Mars' thermal evolution constrained by the crustal magnetization and volcanic resurfacing: Present-day melting and the disappearance of the global magnetic field explained

by

A. C. Glerum

3118622

A thesis submitted to the
Faculty of Geosciences of
Utrecht University in partial fulfillment
of the requirements for the degree of
Master of Science

Supervisor dr. A. P. van den Berg
Department of Theoretical Geophysics
2012

This thesis entitled:
Mars' thermal evolution constrained by the crustal magnetization and volcanic resurfacing: Present-day melting and the disappearance of the global magnetic field explained
written by A. C. Glerum
has been approved for the
Department of Theoretical Geophysics

A. P. van den Berg

J. A. M. Paulssen

Date

The final copy of this thesis has been examined by the signatories, and we find that both the content and the form meet acceptable presentation standards of scholarly work in the above mentioned discipline.

MARS' THERMAL EVOLUTION CONSTRAINED BY THE CRUSTAL MAGNETIZATION AND VOLCANIC RESURFACING: PRESENT-DAY MELTING AND THE DISAPPEARANCE OF THE GLOBAL MAGNETIC FIELD EXPLAINED

Convection modeling so far failed to explain the thermal state of Mars in view of the observed long-lived volcanism, absence of plate tectonics and the early generation and subsequent cessation of a core magnetic dynamo. Therefore I have applied both parameterized and full convection models of mantle convection coupled to the evolution of the core in a search for a suitable combination of model parameters that might explain the available observations.

The 2D radially symmetric parameterized models allow for a fast exploration of the parameter space spanned by the thermal conductivity structure, radioactive element concentration and partitioning between mantle and crust as well as the initial temperature profile and superheating of the core. A combination of the above parameters that is both physically plausible and meets the constraints derived from the cessation of the Martian global magnetic field, growth rate of the crust, surface heat flow and the formation temperature and depth of partial melt forms the basis for the full convection models. Also, it is found that the different radioactive element concentrations used in the literature on Mars' thermal state produce such a wide range of results that these studies should be compared with care.

With axisymmetric statistical equilibrium full convection models the effect of the viscosity structure –another major control on the thermal state– on the present-day Mars is investigated. However, comparison with equivalent transient full convection models shows that the equilibrium models do not accurately represent the current state of the Martian mantle. The parameterized thermal histories do agree reasonably well with equivalent time-dependent full convection models.

Subsequently, using transient axisymmetric full convection models I studied the effect of radioactive element partitioning between mantle and crust, initial superheating of the core, viscosity type and structure, thermal conductivity structure, internal heating rate and compositional buoyancy on the temperature and melt productivity distribution and the convective planform of the mantle. It becomes clear that the generation of mantle plumes is highly dependable on the ratio of internal to bottom internal heating. The observational constraints on core heat flow, CMB temperature, volcanic productivity, surface heat flow and the distribution of partial melting are met by a model with Arrhenius viscosity that includes a 600 km thick top layer representing mantle material depleted through partial melting. The core is initially superheated about 200 K with respect to the mantle and only 35% of the relatively low total amount of radioactive elements is partitioned into the crust. The early generation of the core dynamo through thermal convection is explained by the large temperature difference of the core with respect to the mantle, its demise by the equilibration of mantle and core temperatures due to the isolating effect of the buoyant stagnant lid before the core has cooled enough for core crystallization to set in. Partial melting in the hot mantle shifts to greater depths upon thickening of the lithosphere during secular cooling, but the chaotic nature of thermal convection still enables periods of shallower melting that sustain an episodic volcanism through time.

Acknowledgements

I would like to thank Arie for his critical notes, new perspectives and advice. His enthusiasm and ideas are inspiring. I am also grateful to Jellie for providing me with some of the post processing programs. Janneke, Tennia and Klara, thanks for the great times in the office. And to Thomas and all my friends and family, thank you for your support.

Contents

Chapter

Tables

Table

Figures

Figure

Chapter 1

Introduction

For several decades, missions to Mars have enabled us to study our neighbouring planet extensively. What was once considered a 'dead' planet proves to have been continuously altered by volcanic, fluvial and periglacial activity (Hartmann and Neukum, 2001), resulting in some of Mars' most striking global features. Especially the crustal dichotomy (Zuber, 2001); the magnetic anomalies found in the upper part of the crust that derive from a past global magnetic field (Stevenson, 2001); and the continuous, although decreasing, volcanism up to the last 10 My (Hartmann and Neukum, 2001) together with the vast volcanic provinces Tharsis and Elysium require a renewed vision on the past and present thermal state of Mars. While these observations pose many new questions that yet remain unanswered, they also present us with an opportunity: by constraining both parameterized and full convection numerical models with recent observations, this thesis provides the necessary comprehensive model of Mars' thermal evolution and shows that the present state is the inevitable result of the cooling of the stagnant lid convective planet.

1.1 Why Mars is interesting: Earth versus Mars

At first inspection, Mars is not unlike the Earth. For example, both terrestrial planets are characterized by an atmosphere, magmatic activity, a crustal dichotomy and a past or present global magnetic field. Despite this resemblance, Mars is fundamentally different in several ways.

For one, Mars is a relatively small planet, resulting in a surface to volume ratio $3R^2/R^3$ that is almost twice as large as that of the Earth. A large surface area allows for a faster loss of heat to space, suggesting rapid planetary cooling.

However, as opposed to Earth, Mars is presently a one-plate planet, and probably has been for most of its history (Zuber, 2001). Hence it does not experience plate tectonics, but is in a stagnant lid regime: no descending slabs cool the mantle, nor is heat lost through crust formation at Mid-Ocean Ridges (the main heat loss mechanisms of the present Earth). Because the lithosphere does not take part in convection (through subduction), possible convection is confined to the underlying mantle, and conduction is the principal mechanism of heat transport in the stagnant lid. Most likely, the less efficient conductive heat transport caused Mars to remain relatively warm, enabling present-day melting of the mantle (as evident from the recent volcanism found by Hartmann and Neukum (2001)). Some authors (e.g. Nimmo and Stevenson, 2000; Connerney et al., 2005, cited in Breuer et al., 2010) do however suggest an early period of plate tectonics to enable the generation of a core dynamo (which requires significant heat flow from the core).

The absence of plate tectonics prevents large-scale reworking of crustal material (except, perhaps, through crustal delamination (Schumacher and Breuer, 2006)). Hence, the primarily basaltic Martian crust formed through partial melting of primitive mantle (McSween et al., 2009) and is analogue to oceanic crust on Earth. Whereas the Earth's crust is divided into oceanic and continental crust, Mars' crustal dichotomy divides the surface into the heavily cratered southern highlands and the smoother, less cratered northern lowlands (Zuber, 2001). The crater density of the southern hemisphere suggests a Noachian age ($\geq$ 3.7 Gy old), while, although the basement is at least as old as the southern crust (Frey et al., 2002), the northern hemisphere has been resurfaced during the later Hesperian (3.1-3.6 Ga) (Hartmann and Neukum, 2001; Zuber, 2001). This younger crust measures only weak magnetizations, while the southern hemisphere shows both weak and strong magnetic field intensities (Langlais et al., 2004, cited in Breuer et al., 2010).

Also, because Mars is relatively small, pressure ranges in the mantle and core are much lower than on Earth. The core radius, although still uncertain, must lie between 1520 and 1840 km (Yoder et al., 2003), placing the Core-Mantle Boundary (CMB) at a pressure of only 20-24 GPa. The endothermic spinel-perovskite phase transition is only possible for a core at the higher end of this range and could disappear all together with ongoing cooling due to its negative Clapeyron slope (Bertka and Fei, 1997; Michel and Forni, 2010). The presence of a lower mantle as on Earth thus remains uncertain.

It is exactly the differences between the terrestrial planets otherwise so alike that make Mars such an interesting subject to study: understanding Mars will also increase our knowledge of the Earth. Also, in the light of the search for extraterrestrial life and the promising conditions for (previous) life on Mars, it is key to gain insight into the different evolution of this planet in relation to the Earth.

1.2 Evolution of the Martian core and melt production yet unresolved

Due to Mars' unfamiliar size and convective regime and the many uncertainties in composition and structure, the evolution of its thermal state is not completely understood. Especially the present and past state of the core together with the disappearance of the dynamo and the continuous volcanism in the absence of plate tectonics are, thus far, not properly explained.

The Mars Global Surveyor detected strong magnetic fields that derive from the upper tens of kilometers of crust, but did not record a current global magnetic field (Acuña et al., 1999). Most likely, the magnetic anomalies of about 10-30 Am^{-1} represent remanent thermal magnetization of large volumes of crust, most of which was acquired during a time when Mars did experience a strong global field (Stevenson, 2001). Evidence from the distribution of the magnetization, impact craters and a limited number of Martian meteorites suggests the observed magnetization was acquired prior to 4.02-4.20 Ga (Stevenson, 2001; Lillis et al., 2007). Hence, a core dynamo was probably only active during the first 300-500 My of Martian thermal history (although Schubert et al. (2001) consider a later event of dynamo activity).

Several causes for the termination of the magnetic dynamo have been suggested in the literature. Stevenson (2001) summarizes three possible scenarios: 1) an initially hot Mars cools fast, while the convecting core remains liquid, until, with decreasing cooling rates, the heat flow out of the core can be accommodated by conduction alone, convection stops and the field is no longer generated; 2) a core with little sulfur crystallizes to form a solid inner core, enriching the liquid outer core in sulfur until the outer core is either completely gone or too thin for convection to occur; 3) a change from mobile to stagnant lid convection decreases the possibility for the core to transfer heat to the mantle and thus to cool, indifferent of the presence of an inner core. Yoder et al. (2003) rule out the possibility of a completely solid core inhibiting a magnetic field from analyses of the gravity effect of deformation by the solar tide extracted from the Mars Global Surveyor data. Stewart et al. (2007) argue that the core is not at all or hardly crystallized, because the estimated areotherms of the core are higher than the liquidi of the eutectic Fe-FeS system at pressures comparable to those of the Martian core (25-40 GPa). Also, Breuer and Spohn (2006) conclude from parameterized modeling that in a core close to the eutectic composition of 14 wt% S (sulfur estimates range from 10.6 to 16.2 wt% (Stewart et al., 2007)) no solid inner core would form and thus favor a strictly thermal dynamo. Moreover, many studies recognize the fact that the relatively abrupt cessation of plate tectonics as implied by the third scenario is difficult to explain (Stevenson, 2001). In addition, since the crustal dichotomy is thought to have been in place around 4.5 Ga, a subsequent period of plate tectonics is unexpected (Solomon, 2005).

Other, more novel theories include impact heating reducing the CMB heat flux to a level insufficient to sustain a core dynamo (Roberts et al., 2009) and shock waves from giant impacts heating and stratifying the core preventing thermal convection (Arkani-Hamed and Olsen, 2010). Reese and Solomatov (2010), on the contrary, find that a layer at the top of the core of impactor iron droplets produced in mantle melting through these early giant impacts can power a dynamo. Obviously, which scenario the Martian core followed is still under debate.

Volcanism is mostly concentrated in the Tharsis and Elysium provinces. Tharsis is a large topographic rise built up of magmatic and volcanic material extruded through major shield volcanoes (~3 x 10^8 km^3); the Elysium province is a similar structure, but of a smaller scale (Zuber, 2001). Using crater-counting techniques, Hartmann and Neukum (2001) date the youngest lava flows on Mars to be at most 10 My old. This implies partial melting continues up to the

geological present, requiring super-solidus temperatures in the upper mantle even after 4.5 Gy of cooling. Kiefer (2003; Li and Kiefer, 2007) hypothesizes such longstanding melt production is possible due to decompression melting in the heads of stagnant mantle plumes underneath the volcanic provinces that bring up heat from the core. Schumacher and Breuer (2006) find that a lower thermal conductivity in the crust and mantle delays the cooling of the mantle such that a global layer of melting is sustained for several billion years. When this continuous layer disappears, variations in crustal thickness can locally raise the mantle temperature enough for melting to occur. Although Mars experienced volcanism throughout its history, distinct peaks in the intensity of volcanic activity are found (Neukum et al., 2010). Neukum et al. (2010) suggest this pulsating type of volcanism derives from intervals of higher crustal mobility alternating with periods of stagnant lid convection. It could also be that the fluctuations in volcanism are the result of a natural variability in the melt production due to the chaotic nature of mantle convection.

Whichever mechanism enables melting up to the present, it is closely related to the convective patterns in the mantle and the distribution of melt regions. A focused plume requires stable convection cells (Kiefer, 2003); such a plume can be achieved by the high temperature, low pressure- and temperature-dependent thermal conductivity feedback mechanism described by Schott et al. (2001). A global melt layer or the episodic nature of melting can be identified from the melt productivity distribution and magnitude. The convective planform and distribution of melt zones in the mantle are thus of great interest. Hence they are the primary focus of the numerical experiments in this thesis together with the evolution of the core and the global magnetic field.

1.3 Comprehensive numerical model of Mars' thermal evolution

In this thesis I take into account that the evolution of the core, melting in the mantle and crustal growth all affect the convective planform and thermal state of the Martian mantle. It does not suffice to study any one of these contributions individually; hence all are incorporated into the numerical models used to resolve the planetary thermal evolution. Moreover, in coupling the evolution of the mantle to that of the core and crust, the inflow of heat at the CMB and the outflow of heat from the mantle to the crust or space (and, possibly, to the core) as well as the magma and related crust generation can be constrained by observations on the magnetic field and the volcanic resurfacing rate (the observational constraints are discussed in Chapter 4). Often, the focus lies on processes at either one of the mantle's boundaries (e.g. Kiefer, 2003; Schumacher and Breuer, 2006).

Wherever models are constrained by observations on processes at both the CMB and the surface, these models are based on one-dimensional parameterizations of convection that cannot resolve the mantle structure (for example, Breuer and Spohn, 2003; Williams and Nimmo, 2004). Here, three different modeling methods are applied –parameterized convection models, statistical equilibrium full convection models and transient full convection models– and their applicability to Martian thermal evolution studies is assessed. The numerical models are described in Chapter 2. Especially the first two methods are often applied in the literature (for instance, Williams and Nimmo, 2004; Schumacher and Breuer, 2006 and Kiefer, 2003; Li and Kiefer, 2007, respectively); comparison with the latter method shows both should be used with care.

The parameters investigated with the numerical models are those thought to affect cooling of the mantle most:

The *thermal conductivity* determines the efficiency of conduction through the lithosphere and thermal boundary layers –the limiting factor in the cooling of Mars– and a low conductivity may preserve high temperatures in the shallow mantle for several hundreds of millions of years, focusing hot upwellings and enhancing the lifespan of volcanism (e.g. Schott et al., 2001; van den Berg et al., 2005; Schumacher and Breuer, 2006).

The *viscosity structure* is of interest because within the convecting mantle, convection is the dominant heat transfer mechanism. Convective vigor increases with the Rayleigh number and is therefore most effective for a low viscosity. Also, temperature-dependent viscosity is thought to focus upwelling plumes (Schott et al., 2002).

The heat transported by convection and conduction is provided by secular cooling (including bottom heating of the mantle by a cooling core) as well as by the decay of radioactive elements (internal heating). The incompatible radioactive elements are transferred into the crust through partial melting; the closer they are to the

surface, the faster their produced heat is lost to space. Kiefer (2003) therefore stresses the importance of incorporating *radioactive element partitioning* between the crust and mantle into model calculations. Obviously, the *initial concentration of radioactive elements* in the primitive mantle is important as well.

The *initial superheating of the core* with respect to the mantle determines the amount of bottom heating of the mantle, thus affecting the CMB heat flux, the convective regime in the core and generation of mantle plumes through thermal boundary layer instabilities.

Based on the parameter study (Chapter 3), the thermal state of the Martian mantle is resolved, i.e. the evolution of convection patterns and melt productivity regions, in the context of planetary thermal evolution. A realistic and relatively simple model constrained by among others the presence/absence of the magnetic field and the volcanic resurfacing rate is found to explain all observations in a self-consistent manner (Chapter 4). It illustrates how the Martian mantle can remain warm up to the present and how the core dynamo could have ceased without the need for a 'deus ex machina' (e.g. giant impacts (Robert et al., 2009; Arkani-Hamed and Olson, 2010; Reese and Solomatov, 2010)) or complex changes in convection regimes (e.g. from plate tectonics to stagnant lid convection (Breuer et al., 2010; Neukum et al., 2010)).

Chapter 2

Description of the numerical models

Both parameterized and full convection models are applied in this thesis. The former model type allows for fast calculations of planetary thermal histories, but is restricted to one-dimensional solutions. The more complex latter type enables resolving a planet's three-dimensional mantle structure in terms of temperature and composition, but requires substantially larger amounts of computational resources. I use two types of full convection models: statistical equilibrium models consider a constant internal heating, while in the transient models radioactive decay is time-dependent. The numerical models are described in the sections below in order of complexity.

It is assumed that at the start of all model runs, at time zero, model-Mars has differentiated into a liquid core, a mantle and, in most cases, a primordial crust. An early differentiation is supported by numerous observations: Lee and Halliday (1997) show that core formation occurred within about 30 My after accretion from tungsten (W) measurements of Martian meteorites. Improved chondritic tungsten compositions suggest the core formed even within the first 13 ± 2 My of the solar system (Kleine et al., 2002). Harper et al. (1995) and Borg et al. (1997) distinguish a major silicate differentiation event within the first 0 to 33 My, of which Kleine et al. (2002) state it is decoupled from core formation. From this and the Nd mass balance study of Norman (1999), Wieczorek and Zuber (2004) conclude a primordial crust of 20 to 30 km (or, at least one-third of the present-day crustal thickness) formed within about 30 My, and subsequent crustal formation is of only minor importance. Also, Solomon et al. (2005) infer that the mantle and primordial crust formed through differentiation of a global silicate magma ocean during the first ~50 My after core formation.

With the exception of the statistical equilibrium models, core-mantle coupling is included in all models. Cooling of the core provides bottom heating of the mantle and is indicative of the heat transport regime in the core (conduction or convection, see Nimmo and Stevenson (2000) and Subsection 4.1.1). With ongoing cooling of the mantle and core, the heat flow is expected to change, hence it does not suffice to apply a constant heat flow or temperature condition on the core-mantle boundary.

Also, every model includes decay of the radioactive elements U, Th and K in the mantle and crust (internal heating), but not in the core (as indicated by the element distribution of Wänke and Dreibus (1994)). Some more recent studies do however include K in the core. One can argue that the effect of including K can be approximated by increasing the initial core superheating, a parameter that *is* varied here.

2.1 Parameterized models

2.1.1 Model domain

With a stagnant lid regime parameterization (based on that of Grasset and Parmentier (1988)), the global properties upper mantle temperature T_m, Core-Mantle Boundary (CMB) temperature T_c, stagnant lid thickness D_l and crustal thickness D_c are solved for on a one-dimensional depth section of a radially symmetric spherical domain. The domain (Figure 2.1) thus consists of a core with a surface temperature T_c and radius R_c; a lower thermal boundary layer with a temperature $\epsilon_m T_m$ at its top; a convecting mantle with an adiabatic temperature increase with depth; an upper thermal boundary layer with bottom temperature T_m; and finally, a non-convecting stagnant lid (of which the

Table 2.1: Parameterized models: Fixed parameter definitions and values

Parameter	**Notation**	**Value**	**Unit**
Planetary radius	R_p	3390 x 10^3	m
Constant mantle gravity acceleration	g	3.7	ms^{-2}
Surface temperature	T_s	220	K
Crustal radiogenic enrichment factor (basaltic melts)	Λ	5	-
Initial lithospheric thickness	D_{l0}	50 x 10^3	m
Mantle reference temperature	T_{ref}	1600	K
Reference viscosity for T_{ref} (dry mantle)	η_0	10^{21}	Pas
Core radius	R_c	1680 x 10^3	m
Core thermal expansivity	α_c	2-3 x 10^{-5}	K^{-1}
Critical Rayleigh number	Ra_{crit}	450	-
Lower thermal boundary layer critical Rayleigh number	Ra_{critb}	2000	-
Mean decay constant ($\tau_{1/2}$ = 2.5 Gy)	λ	2.773 x 10^{-1}	Gy^{-1}
-	δT	2	K

Parameter values are taken from Schumacher and Breuer (2006), with the exception of the lower thermal boundary layer critical Rayleigh number, which is taken from Stevenson et al. (1983), the core thermal expansivity (Böhler et al., 1990) and the decay constant (Turcotte and Schubert, 2002). For all other fixed parameter definitions and values, see table 1 of Schumacher and Breuer (2006, p. 4).

upper tens of kilometers are made up of crustal material) with a bottom temperature T_l and radius R_l and a surface temperature T_s and radius R_p. Constant parameter symbols and values are summarized in Table 2.1.

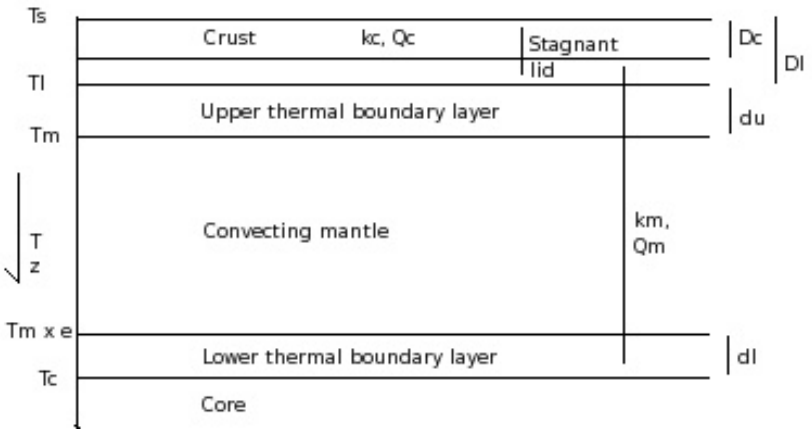

Figure 2.1: Parameterized models: Model domain and parameter definitions. D_c, D_l, δ_u and δ_l denote the thicknesses of the crust, lithosphere, upper thermal boundary layer and lower thermal boundary layer, respectively. k_c and k_m are the thermal conductivities of the crust and mantle, and Q_c and Q_m the heat production densities within the crust and mantle. For further explanations, see main text (Subsection 2.1.1). Note that for illustrational purposes the spherical domain is presented here as rectangular.

2.1.2 Governing equations

Stagnant lid convection is modeled using a one-dimensional parameterization of temperature-dependent viscosity convection in a mantle that is heated both from below by core cooling as well as internally by radioactive decay. The mantle is covered by a stagnant lid consisting of a mantle and a crustal part. The crustal part thickens through ongoing partial melting in a global melt zone underneath the lid, depriving the mantle of radioactive elements.

Based on the convective heat transport in a stagnant lid regime parameterization by Grasset and Parmentier (1998), two coupled energy balance equations are solved, one for the mantle (T_m) and one for the core (T_c),

$$\rho_m C_m V_m \epsilon_m (St+1)\frac{dT_m}{dt} = -q_m A_m + q_c A_c + Q_m V_m \tag{2.1}$$

$$\rho_c C_c V_c \epsilon_c \frac{dT_c}{dt} = -q_c A_c \tag{2.2}$$

with V the volume, q the heat flow, A the surface area and Q the internal heating rate of the mantle (subscript m) and the core (subscript c). St is the Stefan number that accounts for the latent heat effects of partial melting and crystallization. The coupling between core and mantle is parameterized by the dependence of the mantle energy balance equation on the core heat flux.

Two additional differential equations describe the evolution of the stagnant lid (D_l) and crustal thickness (D_{cr}):

$$\rho_m C_m (T_m - T_l)\frac{dD_l}{dt} = -(q_m - (\rho_{cr} L_m + \rho_{cr} C_{cr}(T_l - T_0))\frac{dD_{cr}}{dt}) + k_m(T,P)\frac{\partial T}{\partial r}|_{r=R_l} \tag{2.3}$$

$$\frac{dD_{cr}}{dt} = \frac{D_{pot} - D_{cr}}{D_m} u m_a \frac{V_a}{V_m} \ . \tag{2.4}$$

k_m(T,P) is the temperature- and pressure-dependent mantle thermal conductivity according to the Hofmeister (1999) model (although in most models the mantle conductivity is taken constant, see Subsection 2.2.1). $\frac{\partial T}{\partial r}|_{r=R_l}$ represents the conductive temperature gradient at the base of the lithosphere. m_a is the average melt concentration ($kgkg^{-1}$) in the global melt zone where temperatures exceed the solidus, with V_a the volume of that zone. u is the mean mantle velocity and D stands for thickness, with D_{pot} the potential thickness of the crust in case all melt of a basaltic composition is extracted from the mantle. Subscripts cr and m denote the crust and mantle, respectively. For all other symbols, see Figure 2.1 and Table 2.1.

The equations used to calculate the variable parameter values in Equations 2.1-2.4 are described in Schumacher and Breuer (2006); please refer to Schumacher and Breuer (2006) for the exact formulation, any additions and adaptations are given below. The main difference lies in the calculation of the thermal gradient at the base of the stagnant lid (see right-hand-side of Equation 2.3 and Subsection 2.1.3.2).

2.1.3 Additions and adaptations of the parameterization by Schumacher and Breuer (2006)

2.1.3.1 Heat flow out of the thermal boundary layers

With boundary layer theory for stagnant lid convection (Grasset and Parmentier, 1998), the heat flow out of the mantle into the stagnant lid, q_m, (and the heat flow out of the core into the mantle, q_c) can be calculated,

$$q_m = \frac{k_m(T_m - T_l)}{\delta_u} \tag{2.5}$$

$$q_c = \frac{k_m \Delta T_{cm}}{\delta_l} = \frac{k_m(T_c - \epsilon T_m)}{\delta_l} \tag{2.6}$$

where it is assumed that the average Hofmeister (1999) thermal conductivity of the boundary layer, $(k_{m\delta_{top}} + k_{m\delta_{bottom}})/2$, is representative of the conductivity in the thermal boundary layer in case mantle thermal conductivity k_m is taken pressure- and temperature-dependent. The Hofmeister (1999) model is described in Subsection 2.2.1.

The upper thermal boundary layer thickness δ_u is calculated from the Rayleigh number according to

$$\delta_u = (R_l - R_c)\left(\frac{Ra}{Ra_{crit}}\right)^{-\beta} .^{1} \tag{2.7}$$

By allowing the temperature at the bottom of the stagnant lid, T_l, to evolve with the mantle temperature according to Equation 2.8, instead of determining the mechanical lithosphere by a fixed isotherm, stagnant lid convection with strongly temperature-dependent viscosity can be modeled using the constant viscosity laws given above (Equations 2.5-2.7, see Schubert et al., 1980; Grasset and Parmentier, 1998). (q_m must then be determined by T_l, not T_s, see Equation 2.5).

$$T_l = T_m + 2.21\frac{\eta(T_m)}{d\eta/dT} \tag{2.8}$$

The strongly temperature-dependent effective viscosity of the mantle is

$$\eta = \eta_0 \exp\left(\frac{A(T_{ref} - T_m)}{RT_{ref}T_m}\right) .^{2} \tag{2.9}$$

The scaling factor in Equation 2.8 was set at 2.23 with numerical experiments of convection in a two-dimensional box geometry (Grasset and Parmentier, 1998), but Choblet and Sotin (2000) found a value of 2.21 from 3D experiments.

To calculate the lower thermal boundary layer thickness δ_l (needed in Equation 2.6), the local stability criterion of Stevenson et al. (1983) is applied, considering a local critical Rayleigh number Ra_{critb} of 2 x 10^3 (Equation 2.10). The local criterion implies that the lower thermal boundary layer can be thinner than the upper boundary layer due to the temperature-dependence of the viscosity and the possible thinning of the layer by ascending plumes. Thus, the thickness of the lower thermal boundary layer is equal to the upper layer's thickness, unless calculation of the thickness via the local critical Rayleigh number for breakdown of the thermal boundary layer results in a smaller thickness:

$$\delta_l = \left(\frac{\kappa\eta_c Ra_{critb}}{\alpha\rho_m g_{CMB}\Delta T_{cm}}\right)^{\beta} \tag{2.10}$$

with $\Delta T_{cm} = T_c - \epsilon_m T_m$ the temperature difference across the lower thermal boundary layer, $g_{CMB} = \frac{4\pi}{3}GR_c\rho_c = 3.18\ ms^{-2}$, where G is the gravitational constant of 6.67384 x 10^{-11} $m^3kg^{-1}s^{-2}$, and η_c the geometrically averaged viscosity in the lower thermal boundary layer,

$$\eta_c = \eta_0 \exp\left(\frac{A(T_{ref} - (T_c - \Delta T_{cm}/2))}{RT_{ref}(T_c - \Delta T_{cm}/2)}\right) . \tag{2.11}$$

T_m in Equation 2.9 is replaced by the average temperature in the thermal boundary layer $T_c - (\Delta T_{cm}/2) = (T_c + \epsilon_m T_m)/2$ in Equation 2.11.[3]

With ongoing heating of the mantle and cooling of the core, ΔT_{cm} could become negative, so the fraction in Equation 2.10 is made to be always positive. Still, for a negative temperature difference q_c (Equation 2.6) is accordingly negative, i.e. directed inwards.

2.1.3.2 Heat flow through the stagnant lid

Instead of numerically solving the time-dependent partial differential equation for conductive heat transfer (Schumacher and Breuer, 2006), the temperature gradient $\frac{\partial T}{\partial r}|_{r=R_l}$ in Equation 2.3 is approximated by analytically solving

[1] Although Schumacher and Breuer (2006) state that the fraction of the Rayleigh number and the critical Rayleigh number should be to the power β (in Equation 2.7), this must be -β, for only then does the thermal boundary layer thickness decrease for higher Rayleigh numbers, or, in other words, for more vigorous convection.

[2] When one differentiates the viscosity, it is clear that $T_l = T_m - 2.21\frac{RT_m^2}{A}$ instead of $T_l = T_m - 2.21\frac{R}{AT_m^2}$ given by Schumacher and Breuer (2006).

[3] Schumacher and Breuer (2006) however give $(T_c - \Delta T_{cm})/2 = \epsilon_m T_m/2$ to replace T_m, which does not result in the average temperature needed.

the one-dimensional stationary heat conduction equation (Equation 2.12) with constant mantle and crustal conductivity and heat production density for a two layer domain, resulting in Equation 2.13.

$$k\left(\frac{1}{r^2}\frac{\partial}{\partial r}\left(r^2\frac{\partial T}{\partial r}\right)\right) = -Q \tag{2.12}$$

with Q the heat production density in Wm^{-3}.

$$k_m \frac{dT}{dr}_{r=R_l} = \frac{-Q_m R_l}{3} + \frac{R_{cr}^3(Qm - Qcr)}{3R_l^2} + \frac{\frac{Q_{cr}(R_p^2 - R_{cr}^2)}{6} + \frac{k_m Q_m (R_{cr}^2 - R_l^2)}{6k_m} + \frac{k_{cr} R_{cr}^3 (Q_{cr} - Q_m)}{3k_m R_l} + \frac{k_{cr} R_{cr}^2 (Q_m - Q_{cr})}{3k_m} + k_{cr}(T_s - T_l)}{\frac{R_l^2}{R_{cr}} - \frac{R_l^2}{R_p} + \frac{k_{cr} R_l}{k_m} - \frac{k_{cr} R_l^2}{k_m R_{cr}}} \tag{2.13}$$

Because the derivative of temperature to radius r is used in Equation 2.13, the gradient has to be multiplied with -1. (Otherwise, $\mathrm{q_m}$ and $\mathrm{k_m(T,P)}\frac{\partial \mathrm{T}}{\partial \mathrm{r}}|_{\mathrm{r=R_l}}$ will not have the same sign.) For every integration time step of solving Equations 2.1 to 2.4, the values for $\mathrm{T_l}$, $\mathrm{D_{cr}}$, $\mathrm{Q_m}$, $\mathrm{D_l}$ and $\mathrm{Q_c}$ are updated. Also, it is assumed that the average of $\mathrm{k_m}(\rho \mathrm{g}(\mathrm{R_p} - \mathrm{R_l}), \mathrm{T_l})$ and the conductivity at the bottom of the crust for a linearly interpolated temperature $\mathrm{k_m}(\rho \mathrm{g D_{cr}}, \frac{(\mathrm{T_l} - \mathrm{T_s})\mathrm{D_{cr}}}{\mathrm{D_l}})$ is representative of the variable thermal conductivity in the mantle part of the lithosphere. With a formulation similar to Equation 2.13, the surface heat flow is calculated.

2.1.4 Melting laws and the calculation of partial melting

Secondary crust is produced by partial melting in the mantle and crust. The dependence of the degree of depletion F on the super-solidus temperature (i.e. the difference between the mantle and solidus temperature) can be approximated linearly without significant error (Figure 2.2, Jaques and Green, 1980), where F is defined as the mass fraction of melt produced. The ratio of the difference between mantle and solidus temperature and the temperature difference between solidus and liquidus thus equals the degree of depletion at a particular depth (Equation 2.14). The temperature is known at every depth because it is assumed to increase linearly between the surface and $\mathrm{T_m}$ and from $\mathrm{T_m}$ to $\epsilon_\mathrm{m}\mathrm{T_m}$. The solidus and liquidus temperature at a certain depth are calculated from the overlying pressure deriving from crust and mantle material via the third order polynomial melting laws of Takahashi (1990, see Figure 3.10 for an example).

$$F(z) = \frac{T(z) - T_{sol}(z)}{T_{liq}(z) - T_{sol}(z)} \tag{2.14}$$

The *mean* melt concentration $\mathrm{m_a}$ in the melt zone $\mathrm{V_a}$ –the global mantle layer where temperatures exceed the solidus– is thus given by

$$m_a = \frac{1}{V_a}\int \frac{T(z) - T_{sol}(z)}{T_{liq}(z) - T_{sol}(z)} dV_a \tag{2.15}$$

The derivative of the melt concentration $\mathrm{m_a}$ to $\mathrm{T_m}$ is needed for the calculation of the Stefan number (see Equation 2.1 and Appendix A). This number determines the amount of heat lost through partial melting as well as the amount of heat gained through the latent heat of crystallization; both processes affect $\mathrm{T_m}$. As melt is not instantaneously removed and placed on the surface, in this model, rock can melt, crystallize and melt again at the same mantle temperature. All formed melt is however included in crustal production calculations.

2.1.5 Numerical methods

Time integration of the differential equations 2.1 to 2.4 is done with a second order Runge-Kutta time stepping scheme:

$$y_n = y_{n-1} + \Delta t f(t_{n-1} + \frac{\Delta t}{2}, y_{n-1} + \frac{\Delta t}{2} f(t_{n-1}, y_{n-1})) \ . \tag{2.16}$$

Per integration time step, all variable parameters are updated; quantities $\mathrm{m_a}$, $\mathrm{V_a}$ and $\frac{\mathrm{dm_a}}{\mathrm{dT_m}}$ are calculated through a separate numerical integration over the model domain (see Equation 2.15); the procedure is described in detail in Appendix A.

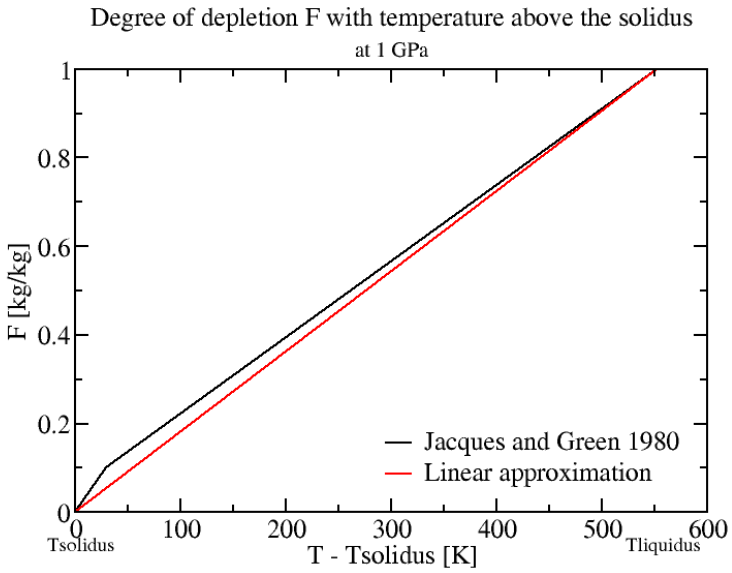

Figure 2.2: Linear approximation of the degree of depletion F with temperature above the solidus (Jacques and Green, 1980).

2.2 Full convection models

2.2.1 Governing equations

In the full convection calculations (including both statistical equilibrium and transient models), the extended Boussinesq approximation is applied, assuming an incompressible fluid (material derivative $\frac{D\rho}{Dt} = 0$) and infinite Prandtl number. The equations solved for are conservation of mass (Equation 2.17), conservation of momentum (Equation 2.18) and conservation of energy (Equation 2.19, Schubert et al., 2001).

The energy equation has contributions from adiabatic (de)compression, viscous dissipation, conduction and advection and heat production through radioactive decay. The temperature and buoyancy effects of partial melting are not considered. The endothermic spinel-perovskite phase transition does not exist for the assumed core radius (Table 2.3, Fei et al., 1995), other phase transitions are neglected.

The variables in the governing equations are scaled as follows: Lengths are non-dimensionalized by dividing by the depth of the model domain, so $x_i' = \frac{x_i}{h}$, while non-dimensional and dimensional temperatures are related via $T' = \frac{T-T_s}{T_{CMB_0}-T_s}$. Time is scaled as $t' = t\frac{\kappa_0}{h^2}$. Velocity scaling is also based on the thermal diffusivity, $u_i' = u_i\frac{h}{\kappa_0}$, as is the scaling of the stress $\tau_{ij}' = \tau_{ij}\frac{\kappa_0\eta_0}{h^2}$. Density, viscosity and internal heating density are scaled by dividing by their reference value, e.g. $\rho' = \frac{\rho}{\rho_0}$.

The scaled conservation equations are given with respect to the reference state (with the reference density, specific heat, gravity and thermal expansivity constant) and primes are dropped from non-dimensional variables (see Tables 2.2 and 2.3 for the definition of the parameters):

$$\frac{\partial u_i}{\partial x_i} = 0 \tag{2.17}$$

$$-\frac{\partial P}{\partial x_i} - TRa + \frac{\partial \tau_{ij}}{\partial x_j} = 0 \tag{2.18}$$

Table 2.2: Full convection models: Abbreviated parameter definitions

Parameter	**Notation**	**Definition**
Thermal Rayleigh number	Ra	$\frac{\rho_0 \alpha_0 g_0 \Delta T_0 h^3}{\kappa_0 \eta_0}$
Internal heating Rayleigh number	Ra_H	$\frac{\rho_0 \alpha_0 g_0 H h^5}{k \kappa_0 \eta_0}$
Heating number	R	$\frac{h^2 H_0 \rho_0}{\kappa_0 \Delta T_0}$
Dissipation number	Di	$\frac{\alpha_0 g_0 h}{c_{p0}}$
Thermal diffusivity	κ	$\frac{k}{\rho_0 c_{p0}}$
Dissipation function	Φ	$\tau_{ij} \partial_j u_i$

Table 2.3: Full convection models: Fixed parameter definitions and values

Parameter	**Notation**	**Value**	**Unit**
Planetary radius	R_p	3396 x $10^{3(a)}$; 3390 x $10^{3(b)}$	m
Constant mantle gravity acceleration	g	$3.72^{(a)}$	ms^{-2}
Surface temperature	T_s	$205^{(a)}$; $220^{(b)}$	K
Crustal thickness	D_{cr}	53 x $10^{3(a)}$; 70 x $10^{3(b)}$	m
Mantle density	ρ_m	$3400^{(a)}$; $3500^{(b)}$	kgm^{-3}
Mantle specific heat	c_m	$1142^{(a)}$; $1200^{(b)}$	$Jkg^{-1}K^{-1}$
Mantle thermal expansivity	α_m	2 x $10^{-5(a)}$; 3 x $10^{-5(b)}$	K^{-1}
Core radius	R_c	1698 x $10^{3(a)}$; 1680 x $10^{3(b)}$	m
Core density	ρ_c	$6750^{(b)}$	kgm^{-3}
Core specific heat	c_c	$840^{(b)}$	$Jkg^{-1}K^{-1}$
Core thermal expansivity	α_c	3 x $10^{-5(c)}$	K^{-1}
Decay constant ($\tau_{1/2}$ = 2.4 Gy)	λ	2.888 x $10^{-1(e)}$	Gy^{-1}
Activation energy	A	2.92 x $10^{5(a)}$; 3 x $10^{5(b)}$	$Jmol^{-1}$
Activation volume	V	0 x 10^{-6}; 6 x $10^{-6(d)}$	m^3mol^{-1}
Grüneisen parameter	γ	$1.2^{(b)}$	-
Bulk modulus	K_T	261 x $10^{9(b)}$	Pa
Pressure derivative of the bulk modulus	K'_T	$5^{(b)}$	-
Lattice contribution fitting parameter for silicates	a	$0.3^{(b)}$	-
Surface conductivity	k_{298}	$4.7^{(b)}$	$Wm^{-1}K^{-1}$

Parameter values are taken from (a) Kiefer (2003), (b) Schumacher and Breuer (2006), (c) Böhler et al. (1990), (d) Karato and Wu (1993) or (e) Turcotte and Schubert (2002).

$$\frac{DT}{Dt} = Diu_z T + \frac{\partial}{\partial x_i}\left(k(P,T)\frac{\partial}{\partial x_i}(T)\right) + \frac{\Phi Di}{Ra} + H(t)R \tag{2.19}$$

Some models incorporate active particle tracers to implement the buoyancy effect of compositional differences. To this end, the transport equation for composition must be solved as well:

$$\frac{\partial \Gamma_c}{\partial t} + \frac{\partial \Gamma_c}{\partial x_j} u_j = 0 \tag{2.20}$$

with Γ_c the composition function describing the local volume fraction of buoyant material.

Newtonian diffusion creep is assumed throughout the domain, together with a purely ductile rheology. Viscosity is stepwise constant, or takes the form of either the temperature-dependent part of the Arrhenius viscosity (activation

volume per mole V = 0 $\frac{\mathrm{m}^3}{\mathrm{mole}}$) or the temperature- and pressure-dependent Arrhenius viscosity:

$$\eta = \eta_0 exp\left(-\frac{(E+PV)}{RT}\right) \tag{2.21}$$

with E the activation energy per mole.

Thermal conductivity k is either (stepwise) constant, or temperature- and pressure-dependent according to the Hofmeister (1999) conductivity model. The temperature- and pressure-dependence derives from the two mechanisms that contribute to conduction in solid materials: vibrations of the lattice (called phonons) and radiation traveling as electromagnetic waves (radiative heat transfer, Hofmeister (1999)).

$$k_m(T,P) = k_{lat}(T,P) + k_{rad}(T) \tag{2.22}$$

with

$$k_{lat}(T,P) = k_{298}\left(\frac{298}{T}\right)^a \exp[-(4\gamma+\frac{1}{3})\alpha_m(T-298)]\left(1+\frac{K_T' P}{K_T}\right) \tag{2.23}$$

$$k_{rad}(T) = 0.01753 - 0.00010365T + \frac{2.2451T^2}{10^7} - \frac{3.407T^3}{10^{11}}\ . \tag{2.24}$$

The internal heating H is taken constant in the statistical equilibrium models. It depends exponentially on time in the transient models, with the half-life of a representative fuel-mix of 2.4 Gy (Turcotte and Schubert, 2002):

$$H(t) = H_0\ \exp(-0.2888\, t) \tag{2.25}$$

with H in Wkg^{-1} and t in Gy.

The initial total amount of heat produced by radioactive decay in the primitive mantle ($\mathrm{H_{pm}V_{pm}}\rho$) is partitioned between the mantle and crust according to crust fraction C, the fraction of heat producing elements transferred into the crust. Therefore, the initial internal heating in the mantle and crust (assuming a uniform density ρ) is

$$H_{m0} = \frac{(1-C)H_{pm}V_{pm}}{V_m} \tag{2.26}$$

$$H_{c0} = \frac{CH_{pm}V_{pm}}{V_c}\ . \tag{2.27}$$

Subscripts pm, m and c denote the primitive mantle (mantle + crust), mantle and crust, respectively.

In the statistical equilibrium models, $\mathrm{H_{pm}}$ is either the present-day internal heating rate to model the current thermal state of Mars or representative of the Martian mantle 4.5 Ga to provide the initial temperature profile for the transient models.

2.2.2 Numerical methods and model domain

Time integration of the conservation equations 2.17-2.20 is done via a Predictor/Corrector time stepping scheme combining the implicit Euler predictor and the Crank-Nicolson corrector methods (e.g. van den Berg et al., 1993).

Computations are based on an axisymmetric domain geometry. The two-dimensional domain is either a half or a quarter circle, with a finite element mesh of 400 or 200 horizontal (at a constant radius) triangular elements, respectively, and 100 radial elements. The software package SEPRAN (Ingenieursbureau Sepra; Segal and Praagman, 2005) is used to construct the mesh. In using axisymmetric geometry, the whole upper hemisphere ($0 < \theta < 1/2\pi$) or the whole of Mars ($0\pi < \theta < \pi$) is modeled and can be envisaged by sweeping the images presented in this study around the axis of symmetry, the Cartesian z-axis. Thus, the solution may vary with radius r and angle θ, but not with angle ϕ, as the solution is symmetric around the vertical axis (Kellogg and King, 1997).

All boundaries are impermeable and free slip, with zero heat flux on the vertical boundaries. The temperature at the outer surface of the domain is fixed, the bottom temperature varies only in the thermal evolution models. For such transient models, the CMB temperature is given by the volume-averaged temperature of the core, which is modeled as an isothermal heat reservoir. The core reservoir cools due to an average heat flow through its surface, see Appendix B.

2.2.3 Initial conditions

The initial radial temperature profile for the transient models is obtained from corresponding statistical equilibrium models (with the exception of the models investigating the thermal conductivity structure, these start from a profile obtained with the parameterization of Section 2.1). The latter start from a linear or adiabatic temperature profile. The core temperature in transient models can be in equilibrium with or superheated with respect to the mantle. In all models, a mid-mantle temperature perturbation is applied at the start of the model run to trigger the onset of convection.

2.2.4 Melting laws and the calculation of partial melting

Several model runs contain passive particle tracers to monitor temperature and velocity throughout the model domain at every integration time step. The particle tracer monitoring data allow for melt productivity calculations. Such calculations are done in separate post processing steps, using either a linear and parallel solidus and liquidus with a 600-K difference (McKenzie, 1984), or a third order polynomial solidus and liquidus (e.g. Takahashi, 1990; Vlaar, van den Berg and Keken, 1994). See Figure 3.10 for an example of the different solidus-liquidus sets.

For each passive particle tracer, partial melting is possible when the temperature of the tracer for a given time step exceeds the solidus at that location. Between the solidus and liquidus, the degree of depletion F is assumed to increase linearly (Jacques and Green, 1980), see Subsection 2.1.4 and Figure 2.2. Because here melting is seen as an irreversible process, only when $F(t_n)$ is greater than $F(t_{n-1})$ melt is produced, and $F(t_n) \geq F(t_{n-1})$. The volume of melt produced then equals the volume represented by the tracer times the increase in degree of depletion. See Appendix C for the details of the calculations.

Melt is not instantly removed and placed at the surface. Also, since compositional buoyancy (other than that imposed by the active particle tracers) is neglected, partially molten material is not retained in a buoyant layer at the top of the domain, but is allowed to sink into the mantle and reheat again, possibly melting more (when the highest previous F is exceeded).

Chapter 3

Results of the numerical modeling experiments

The numerical modeling results are presented in order of complexity: first the parameterized model results, then the results of the statistical equilibrium models and finally those of the transient full convection runs.

3.1 Parameterized models

The parameterized models serve multiple purposes. First of all, parameters expected to be of major influence, such as the thermal conductivity structure and the initial mantle temperature, are varied individually to become acquainted with the sensitivity of the thermal evolution of Mars to these parameters in preparation of the full convection modeling. Second, this parameter study investigates whether uncertainties in our knowledge of Martian conditions (and thus of Martian parameters) affect the compatibility of different studies available in the literature. For example, the heat production density of the primitive mantle is uncertain because the radioactive element concentration is not well-constrained. Hence, different studies consider different internal heating rates, which will affect the thermal evolution. Last, an optimal combination of parameters is found that is both physically plausible and fits the observational constraints (Subsection 3.1.5). This parameter set provides the proper initial conditions for the full convection models.

In the numerical experiments, (1) the crustal thermal conductivity k_c, (2) mantle thermal conductivity k_m, (3) initial crustal thickness D_{cr0}, (4) initial heat production density Q_0, (5) initial mantle temperature T_{m0} and (6) the initial superheating of the core ΔT_{cm0} are varied independently from the reference parameter configuration (taken from Schumacher and Breuer (2006)). The reference model as well as the parameter ranges tested are given in Table 3.1; please refer to Subsection 2.1.1 for a detailed description of the model parameters.

3.1.1 Reference model P0

Figure 3.1(a) gives the evolution of the global parameters T_m, D_l, T_c and D_{cr} and the mantle and core heat flow for the reference model P0 (see Table 3.1). The temperature at the bottom of the upper thermal boundary layer (T_m, Figure 3.1(a)(1)) decreases continuously from 1900 K down to almost 1775 K during the 4.5 Gy of Martian history. The mantle heat flow, dependent on this temperature, follows a similar pattern. The stagnant lid thickness (D_l, (3)) increases fast initially to about 280 km, then continues to increase more gradually up to 560 km. The CMB temperature (T_c, (4)) decreases steadily for 4.5 Gy. The heat flux coming from the core decreases from 7.5 mWm^{-2} to 3.25 mWm^{-2} (q_c, (5)), but the decrease slows down between 1 and 2 Gy. Within the first 250 My, the crust grows fast, up to 24 km, then the crustal thickness (D_{cr}, (6)) remains constant.

Figure 3.1(b) shows the present-day geotherm resulting from the reference model together with the solidus. The lithosphere and upper and lower thermal boundary layer are characterized by a faster increase in temperature with depth than the convective part of the mantle. At every depth, temperatures are well below the solidus, so melting in the current Martian mantle is unlikely for the reference model.

To assess possible pitfalls of the parameterization used, modeling results are compared to those of Schumacher and Breuer (2006). A straightforward comparison of the equivalent reference models learns that T_m in the Schumacher and Breuer (2006) study increases from 1900 K to 2000 K in the first 0.75 Gy, and only then starts decreasing. Also, the stagnant lid is about 150 km thinner after 4.5 Gy and the crust about 40 km thicker than in the current study.

Table 3.1: Parameterized models: Model specifications

Model	$\mathbf{k_c}$ $[\mathbf{Wm^{-1}K^{-1}}]$	$\mathbf{k_m}$ $[\mathbf{Wm^{-1}K^{-1}}]$	$\mathbf{D_{cr0}}$ **[km]**	$\mathbf{Q_0}$ $[\mathbf{Wm^{-3}}]$	$\mathbf{T_{m0}}$ **[K]**	$\mathbf{\Delta T_{cm0}}$ **[K]**	**Figures**
P0	4	4	0	1.6 x 10^{-8}	1900	100	3.1
P1							
P1-1	1	4	0	1.6 x 10^{-8}	1900	100	3.3
P1-2	2	4	0	1.6 x 10^{-8}	1900	100	3.2; 3.3
P1-3	3	4	0	1.6 x 10^{-8}	1900	100	3.3
P1-4	4	4	0	1.6 x 10^{-8}	1900	100	3.1; 3.2; 3.3
P2							
P2-1	4	4	0	1.6 x 10^{-8}	1900	100	3.1; 3.2; 3.3
P2-2	4	$k_m(T,P)$	0	1.6 x 10^{-8}	1900	100	3.2; 3.3
P3							
P3-1	4	4	0	1.6 x 10^{-8}	1900	100	3.1; 3.4
P3-2	4	4	20	1.6 x 10^{-8}	1900	100	3.4
P3-3	4	4	40	1.6 x 10^{-8}	1900	100	3.4
P4							
P4-1	4	4	0	1.6 x 10^{-8}	1900	100	3.1; 3.5
P4-2	4	4	0	5.3 x 10^{-8}	1900	100	3.5
P4-3	4	4	0	8.1 x 10^{-8}	1900	100	3.5
P5							
P5-1	4	4	0	1.6 x 10^{-8}	1800	100	3.6(a)
P5-2	4	4	0	1.6 x 10^{-8}	1900	100	3.1; 3.6(a)
P5-3	4	4	0	1.6 x 10^{-8}	2000	100	3.6(a)
P5-4	4	4	0	1.6 x 10^{-8}	2100	100	3.6(a)
P6							
P6-1	4	4	0	1.6 x 10^{-8}	1900	100	3.1; 3.6(b)
P6-2	4	4	0	1.6 x 10^{-8}	1900	200	3.6(b)
P6-3	4	4	0	1.6 x 10^{-8}	1900	300	3.6(b)
P7	2	$k_m(T,P)$	20	1.6 x 10^{-8}	1900	200	3.7; 3.8
P8	2	$k_m(T,P)$	0	1.6 x 10^{-8}	2000	200	3.7

In all models the initial thickness of the lithosphere, D_{l0}, is 50 km (Schumacher and Breuer, 2006). Model P7 meets the observational constraints discussed in Chapter 4, see Subsection 3.1.5.

The only difference between this parameterization and that of Schumacher and Breuer (for $k_c = k_m = 4$ $Wm^{-1}K^{-1}$) lies in the calculation of the conductive heat flow through the bottom of the stagnant lid (steady-state versus time-dependent heat conduction equation, see Subsection 2.1.3.2). The heat flow thus calculated here is too large (with respect to Schumacher and Breuer (2006)), so the stagnant lid grows faster and more heat is extracted from the mantle. Consequently, the mantle is not able to heat up through radioactive decay and the heat coming from the core, and the temperatures in the mantle fall below the solidus early on, frustrating crustal formation. Simplifying the heat conduction equation thus has a significant effect on the model results.

3.1.2 Thermal conductivity structure: crustal and mantle thermal conductivity

A great uncertainty exists about the materials making up the Martian crust and mantle and hence, for example, the thermal conductivity is not well constrained. For simplicity, a uniform and constant thermal conductivity of 4 $Wm^{-1}K^{-1}$ is incorporated in most models studying Martian thermal histories (e.g. Breuer and Spohn, 2003; 2006). However, Schumacher and Breuer (2006) argue that due to (1) the reversed temperature-dependence of the conductivity of the Martian volcanic crust; (2) the crust's fractured and porous nature; and (3) the extremely low thermal conductivity of the upper few centimeters of soil, the column-averaged crustal thermal conductivity should be

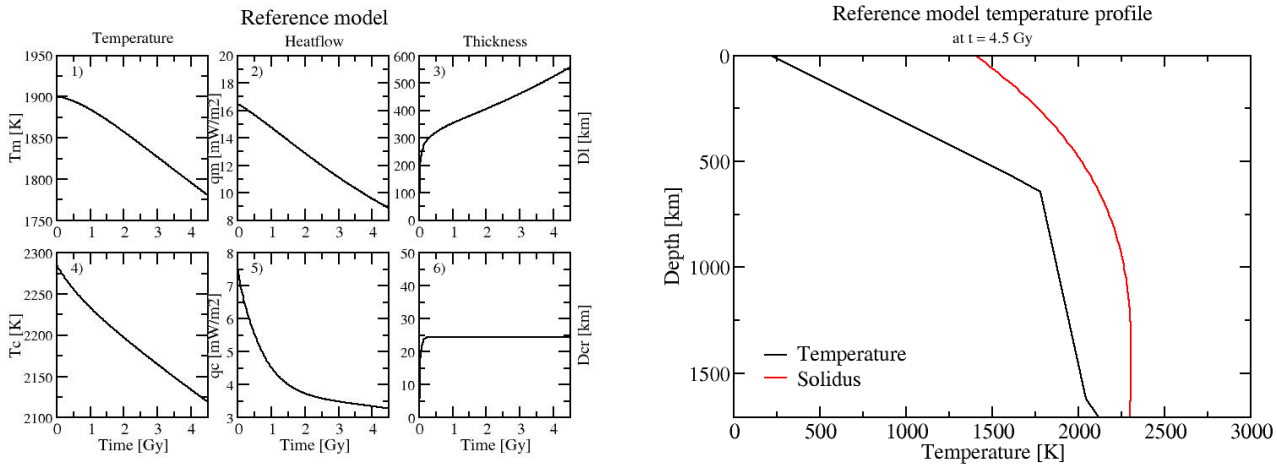

(a) Evolution of the 1) temperature at the bottom of the upper thermal boundary layer T_m; 2) mantle heat flow q_m; 3) lithospheric thickness D_l; 4) CMB temperature T_c; 5) core heat flow q_c; and the 6) crustal thickness D_{cr}.

(b)

Figure 3.1: a) Global parameter and heat flow evolution and b) present-day radial temperature profile for the reference model P0.

on the order of $k_c = 2 \pm 1$ $Wm^{-1}K^{-1}$. Therefore, model P1 varies k_c between 1 and 4 $Wm^{-1}K^{-1}$ (see Table 3.1).

In the mantle, thermal conductivity does not only depend on composition and texture, temperature and pressure play an important role as well. This dependence is described by the Hofmeister (1999) model (Equation 2.22), which results in a mantle conductivity that is at any depth lower than 4 $Wm^{-1}K^{-1}$ for Martian conditions (Schumacher and Breuer, 2006, and Figure 3.19(b)). Thus, constant and temperature- and pressure-dependent mantle conductivity are implemented here in model P2-1 and P2-2, respectively.

By varying the crustal and mantle thermal conductivity with respect to the reference model ($k_c = k_m = 4$ $Wm^{-1}K^{-1}$), their individual effects can be established: Increasing the crustal conductivity from $k_c = 1$ $Wm^{-1}K^{-1}$ to $k_c = 4$ $Wm^{-1}K^{-1}$ has no significant effect on T_m, nor on T_c (as an example, consider the black and blue curves in Figure 3.3(a)(1) and (4)). However, the thickness of the lithosphere increases with crustal conductivity, while the thickness of the crust is inversely related to k_c (Figure 3.3(a)(3) and (6)). Because the depth of T_m is determined by the thickness of the lithosphere and that of the upper thermal boundary layer (see Figure 2.1), it becomes shallower for lower k_c, thus increasing the temperature in the stagnant part of the mantle (see, for instance, the black and blue curves in Figure 3.3(b)).

A variable mantle thermal conductivity $k_m(T, P)$ results in an initial small rise in T_m with respect to the reference model (see, for instance, green and blue curves of Figure 3.3(a)(1)). The delay in secular cooling of about 1.5 Gy leaves a slightly higher present-day temperature ($\delta T_m \approx 50$ K). This effect of variable conductivity was also found by van den Berg et al. (2005) for full convection models. A warmer mantle frustrates heat flow from the core; hence, the core remains hotter (Figure 3.3(a)(4) and (5)). Lithospheric growth is reduced by about 100 km, while the final crustal thickness increases ~3 km. Contrary to lowering the crustal thermal conductivity, for $k_m(T, P)$ the present-day temperature is raised at *every* depth in the model domain (Figure 3.3(b), green and blue curves).

Figure 3.2 summarizes the above effects of conductivity on the mantle temperature: it plots the temperature difference between the solidus temperature at the depth of T_m and T_m, so $T_s(z = D_l + \delta_u) - T_m$, after 4.5 Gy against the crustal conductivity. This solidus temperature deficit acts as an indication of the possibility of present-day melting (Schumacher and Breuer, 2006). It can be seen that a lower crustal conductivity lowers the difference between the

solidus and the mantle temperature by maximally 25 K, while the use of variable mantle thermal conductivity results in a present-day temperature that is about 120 K closer to the solidus. This effect of variable mantle conductivity is larger for low k_c.

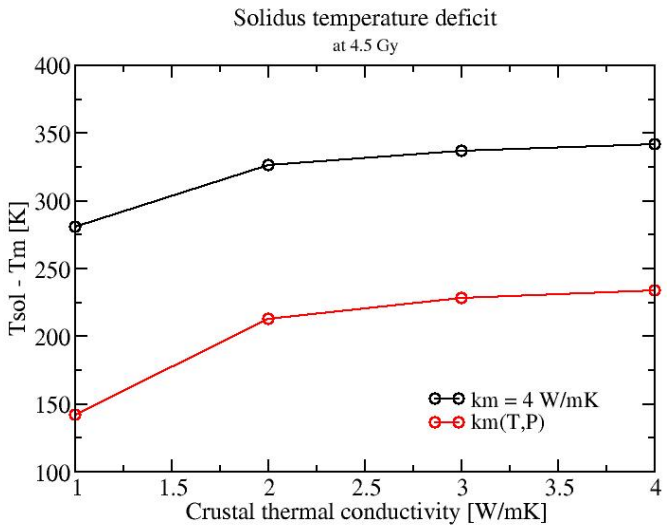

Figure 3.2: Present-day solidus temperature deficit for the contrasting thermal conductivity structures of models P1 and P2 combined. The solidus temperature deficit is defined as the difference between the solidus temperature and the temperature of the sub-solidus mantle.

From the above results, it is expected that the combined effects of a low crustal conductivity and a variable mantle conductivity result in a warmer upper mantle, a thinner lid, a thicker crust and prolonged crust production. Figure 3.3 (green curves) confirms these expectations: For instance, the crust is thickest (about 29 km) and takes the longest time to form (about 550 My) in the $k_c = 2$ $Wm^{-1}K^{-1}$, k_m(T,P) case (Figure 3.3(a)). Also, present-day temperatures in the upper thermal boundary layer and stagnant lid are up to 250 K higher for this conductivity structure, in the convective mantle about 75 K (Figure 3.3(b)).

The effects of changing the thermal conductivity structure (Figures 3.2 and 3.3) are different for the parameterization of Schumacher and Breuer (2006, pp. 7-9, figures 3, 4b and 5b). For example, qualitatively the effects on the crustal thickness are the same, but quantitatively the final thickness increases much more over a longer timespan with their calculations. In part, this is caused by the different application of variable mantle conductivity. Here, the steady-state heat equation (Equation 2.12) is solved analytically for constant conductivity in both the mantle and crust. When implementing variable mantle conductivity in the model, it is chosen to use the average of the variable mantle conductivity value at the base of the lithosphere for T_l and that at the bottom of the crust for a linearly interpolated temperature between T_l and T_s. In the parameterization of Schumacher and Breuer (2006), however, the heat flow at the base of the lithosphere depends on the variation in conductivity throughout the lid, which, as Figure 3.19 shows, is significant. Right within the lid lies the minimum in mantle thermal conductivity, which greatly inhibits upward heat conduction. The thermal gradient calculated for variable mantle thermal conductivity here is therefore probably too high, resulting in a thicker stagnant lid, enhanced cooling and less crust production (with respect to Schumacher and Breuer (2006)).

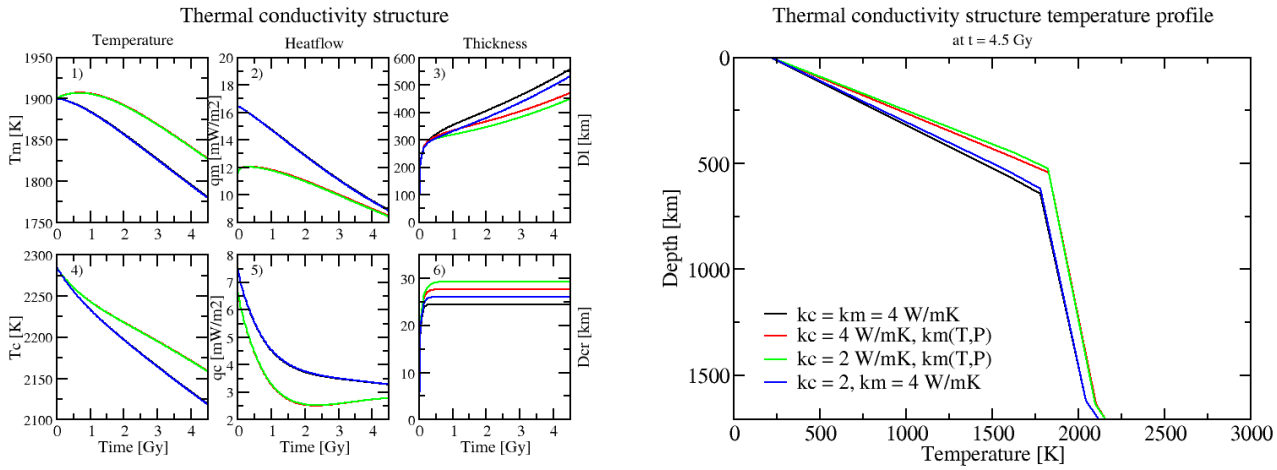

(a) See Figure 3.1(a) for a detailed description of the individual plots. (b)

Figure 3.3: a) Global parameter and heat flow evolution and b) present-day radial temperature profile for the contrasting thermal conductivity structures of models P1 and P2 combined. The colour schemes of a) and b) are identical.

3.1.3 Internal heating: primordial crustal thickness and initial heat production density

The existence of an enriched primordial crust is suggested by several cosmochemical models (e.g. Norman, 1999; 2002; Wieczorek and Zuber, 2004). A primordial crust, formed during the early differentiation of Mars, removes a significant amount of heat producing radioactive elements from the primitive mantle, lessening the heating of the planet's interior. From a thorough analysis of published and new crustal thicknesses, Wieczorek and Zuber (2004) conclude that at least one-third of the present-day Martian crust is primordial, so at least 13 to 21 km of their estimate of 38 to 62 km. Because previous studies have considered a much thicker present-day crust (up to ~125 km, e.g. Kavner, 2001, cited in Hauck and Philips, 2002), primordial thicknesses of 0, 20 and 40 km are tested here with model P3.

Because a primordial crust removes radioactive elements from the mantle, the thicker the initial crust, the more T_m decreases (Figure 3.4(1)). Moreover, temperatures are lower at every depth within the model domain up to the present with respect to reference model P0. Subsequently, the temperature difference between mantle and core increases and the heat flow out of the core is slightly larger, cooling the core faster (Figure 3.4(4) and (5)). Temperature difference are however not big enough for the formation of additional crust to differ between the model runs (Figure 3.4(6)): the final crustal thickness increases with exactly the primary crustal thickness. (Note that the final crustal thickness is less than three times the initial thickness.) The lithospheric thickness does differ, but only after crust formation ceases (Figure 3.4(3)). Then, the lid grows more for thicker crusts, about 25 km per 20 km of extra primordial crust.

There is great variation in the heat production density of the primitive Martian mantle (mantle + crust) in the literature. Most commonly, it is derived from the radioactive element distribution of Treiman et al. (1986), Wänke and Dreibus (1994) or Lodders and Fegley (1997). Table 3.2 shows that especially the concentration of potassium (K) is debated. Model P4 tests the three different heat production densities to estimate their effect on the thermal state of Mars.

The higher initial internal heating rates after Wänke and Dreibus (1994, WD94, P4-2) and Lodders and Fegley (1997, LF97, P4-3) result in an initial mantle temperature rise of 100 and 150 K, respectively (Figure 3.5(1)). Also, the higher the initial heating rate, the faster the warming and subsequent cooling of the mantle. Hence the present-day temperature is about 75 K lower for LF97 than for the WD94 case. The core temperature increases after a small initial fall, most for the LF97 case (Figure 3.5(4)). This heating is due to a negative core heat flow: the hot mantle provides heat to the core. The last two and a half billion years, the core cools, and core heat flows are above zero. The

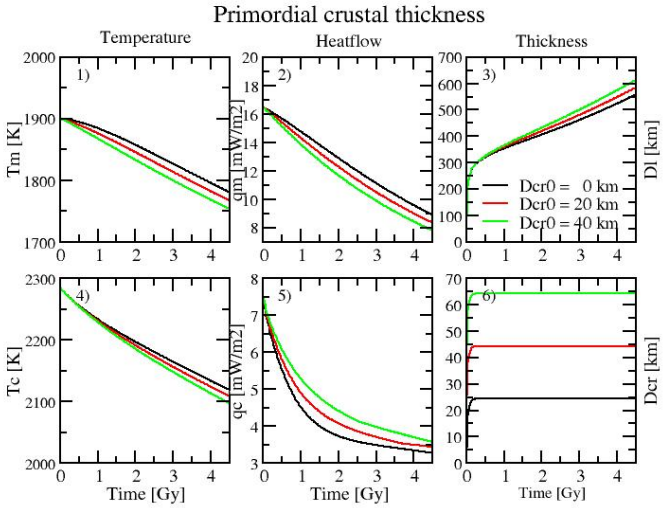

Figure 3.4: Global parameter and heat flow evolution for the contrasting primordial crustal thicknesses of model P3. See Figure 3.1(a) for a detailed description of the individual plots.

Table 3.2: Radioactive element concentrations for the Martian primitive mantle

Element	**SB06-T86**$^{(a)}$	**WD94**$^{(b)}$	**LF97**$^{(c)}$
K	160 ppm	305 ppm	920 ppm
U	16 ppb	16 ppb	16 ppb
Th	48 ppb	56 ppb	56 ppb

Radioactive element concentrations from (a) Schumacher and Breuer (2006) based on data from Treiman et al. (1986), (b) Wänke and Dreibus (1994) or (c) Lodders and Fegley (1997).

higher radioactive heating greatly prolongs crust production as crustal growth continues for 3.25 Gy (Figure 3.5(6)). For the LF97 heating rate, the crust even becomes as thick as the lithosphere, which results in some strange effects in lithospheric and crustal growth (because the crustal thickness is not allowed to exceed the lithospheric thickness as this would most likely result in crustal delamination (Schumacher and Breuer, 2006)).

Figure 3.5 demonstrates that the diversity in heat production densities in the literature used for Martian thermal evolution models (Table 3.2) is so substantial that temperatures can vary up to 100 K, and, more importantly, the stagnant lid and crustal thickness as much as 200 km. This signifies that results of different studies can only be compared with caution, and perhaps need to be adjusted for internal heating prior to comparison. The unrealistically thick crusts that exceed the lithospheric thickness and the negative core heat flows will be of even larger magnitude when using the parameterization of Schumacher and Breuer (2006), because this model cools slower (see Subsection 3.1.1 and 3.1.2); perhaps something inherent to the model does not allow for high heating rates.

3.1.4 Initial radial temperature profile: initial mantle temperature and core superheating

Estimating the initial temperature distribution of Mars is difficult. It can be assumed that in the initial stages of evolution (after core-mantle differentiation), Mars is hot and partially molten. When considering the mantle solidus, temperatures thus have to be higher than about 1600 K (Nimmo and Stevenson, 2000). On the other hand, it is unlikely that the mantle remained above the liquidus for a substantial amount of time (Breuer and Spohn, 2006). The

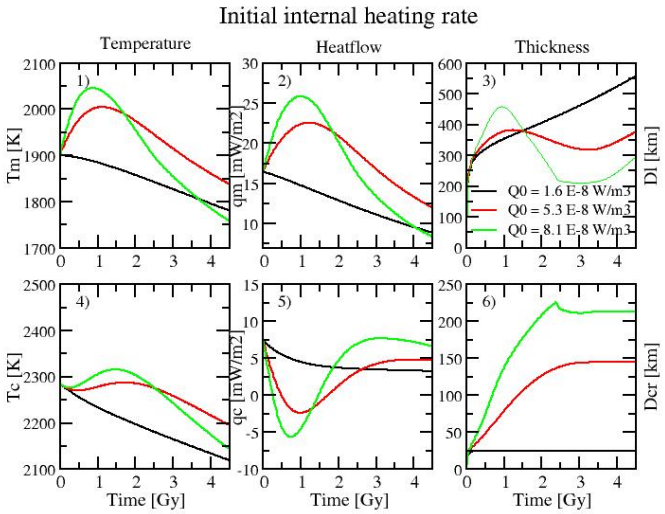

Figure 3.5: Global parameter and heat flow evolution for the contrasting initial internal heating rates of model P4. See Figure 3.1(a) for a detailed description of the individual plots and Table 3.2 for the specific radioactive element concentrations of each internal heating rate.

liquidus temperature at the CMB is about 2300 K (Breuer and Spohn, 2006), providing rough boundaries on the initial mantle temperature of 1600 K to 2300 K. Here, results are shown for initial temperatures T_{m0} varied between 1800 K and 2100 K (model P5). Additional test runs show that lower initial temperatures do not produce any significant amounts of crust and that for higher temperatures unrealistically thick crusts form.

Although throughout the first 3 Gy temperature differences are large, Figures 3.6(a)(1) and (4) show that after 4.5 Gy mantle and core temperatures do not differ much between the model runs. For $T_{m0} = 1800$ K, hardly any crust is produced (about 3 km), while for $T_{m0} = 2100$ K, approximately 165 km of crust forms in 1.5 Gy (Figure 3.6(a)(6)). Melting and crust formation are thus significantly prolonged by higher T_{m0}. The rapid crust production in the highest T_{m0} case is accompanied by a fast increase in lithosphere thickness. The lid thickness declines later on, so after 4.5 Gy the thickness in all cases is similar (Figure 3.6(a)(3)).

After differentiation of Mars into a crust, mantle and core, the core is most likely superheated with respect to the mantle (Flaser and Birch, 1973, cited in Stevenson, 2001): the core and mantle are not in thermal equilibrium. Because they are not, a thermal boundary layer is expected to form above the CMB with a high temperature contrast. The initial amount of superheating is defined here as the initial temperature increase over this boundary, so $\Delta T_{cm0} = T_{c0} - \epsilon T_{m0}$. At the start of the above model runs, the core is superheated 100 K with respect to the mantle. Model P6 also considers superheatings of 200 K and 300 K.

The final values of T_m, q_m, D_l, T_c and q_c are not affected, but the initial evolutions of T_c, q_c and D_{cr} do differ for the higher superheatings of P6-2 and P6-3 (Figure 3.6(b)). For example, the core heat flow is higher than 20 mWm^{-2} for the first 500 My in case $\Delta T_{cm0} = 300$ K, rapidly reducing the temperature of the core. The crustal thickness increases 4 km per 100 K of extra superheating. These results agree with those of Breuer and Spohn (2006), who find that an initial superheating of over 100 K is required by the presence of an early magnetic field on Mars (see Subsection 4.1.1), but that the exact value has no significant effect on crustal formation (only several kilometers of extra crust per 100 K additional superheating).

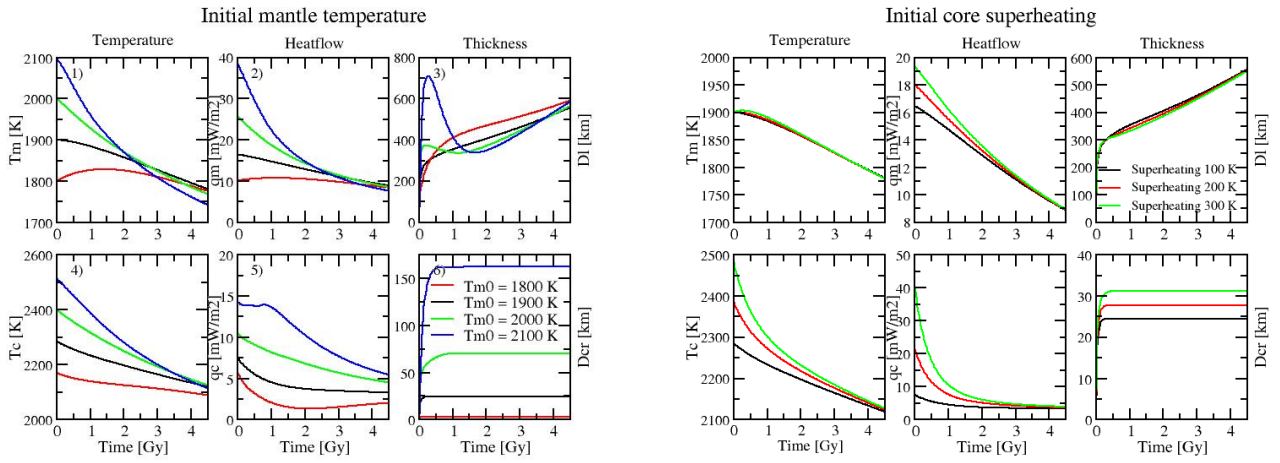

(a) (b)

Figure 3.6: Global parameter and heat flow evolution for the contrasting initial a) mantle temperatures of model P5 and b) core superheatings of model P6. See Figure 3.1(a) for a detailed description of the individual plots.

3.1.5 Initial model conditions properly constrained by observations

The low crustal thermal conductivity and variable mantle conductivity model of Schumacher and Breuer (2006) is considered to resemble the actual conductivity profile of Mars more than the canonical uniform value of 4 $Wm^{-1}K^{-1}$. Due to the reduced efficiency of heat transport through the crust and thermal boundary layers, it slows down the cooling of the Martian mantle, prolongs the existence of a global melt zone underneath the lithosphere, produces more crust and results in a smaller temperature difference between the solidus and the mantle temperature at the present (Figures 3.2 and 3.3). However, the insulating effect of this conductivity structure is not large enough to meet the constraints on the CMB temperature, surface and core heat flow and crustal thickness that will be discussed further in Section 4.1 (compare the green curves in Figure 3.3 with the constraints shown in Figure 3.7).

Models P1-P6 help to find a combination of parameters (P7) that does meet the observational constraints on which the full convection models will be based. As a basaltic primordial crust is suggested by several cosmochemical models (e.g. Kleine et al., 2002), a primary crust of 20 km is added, which is within the boundaries estimated by Wiezcorek and Zuber (2004). Although this removes radioactive elements from the mantle, it does increase the final crustal thickness (Figure 3.4). Together with an initial superheating of the core of 200 K, the crustal thickness (evolution) (Wieczorek and Zuber, 2004), Noachian potential temperatures and melting depths (Filiberto and Dasgupta, 2011) and the newly defined core heat flow constraints of 4-13 mWm^{-2} (Subsection 4.1.1) are satisfied (Figure 3.7, red curve P7, and Figure 3.8). The average surface heat flow falls just below the lower limit within the first 100 My, but it does follow the later Hesperian and Amazonian heat flow (< 3.6 Ga) as reported by McGovern et al. (2004). The CMB temperature during the first 500 My is > 2300 K (Figure 3.8). Extrapolating this temperature along the core adiabat shows that core temperatures are well above the liquidus (Breuer and Spohn, 2006; Stewart et al., 2007), so core convection driven by compositional differences is not supported. Within 1 Gy the core cools about 100 K, so the cooling rate required for thermal convection of 80 KGy^{-1} (Stevenson, 2001) is satisfied.

Schumacher and Breuer (2006) find that $k_c = 2$ $Wm^{-1}K^{-1}$, $k_m(T,P)$ and $D_{cr0} = 40$ km suffices to meet the crustal evolution constraints. They do however not consider the core heat flow and state it is below 5 mWm^{-2} within 'a few hundred million years' (p. 16). It is likely that the additional core heat flow constraint used in the current study would change their findings, because the differences in parameterization result in a slower cooling of their model mantle (and thus lower heat flows).

Another plausible combination of parameters (P8) is obtained by raising the initial mantle temperature by 100 K combined with a core superheating of 200 K (Figure 3.7, green curve P8). The core heat flow then exceeds the upper constraint calculated in this study and that of Nimmo and Stevenson (2000) during the first 400 My and the lithosphere remains thinner than 400 km. Nevertheless, the final crustal thickness is about 120 km, with crustal production continuing well into the Early Amazonian (~2 Ga). Although crustal thicknesses of that order have been suggested (e.g. Kavner, 2001, cited in Hauck and Philips, 2002), a mean value of 50 km is more accepted (Wieczorek and Zuber, 2004). Hence, the first model is considered to fit best with the observational constraints available to this date.

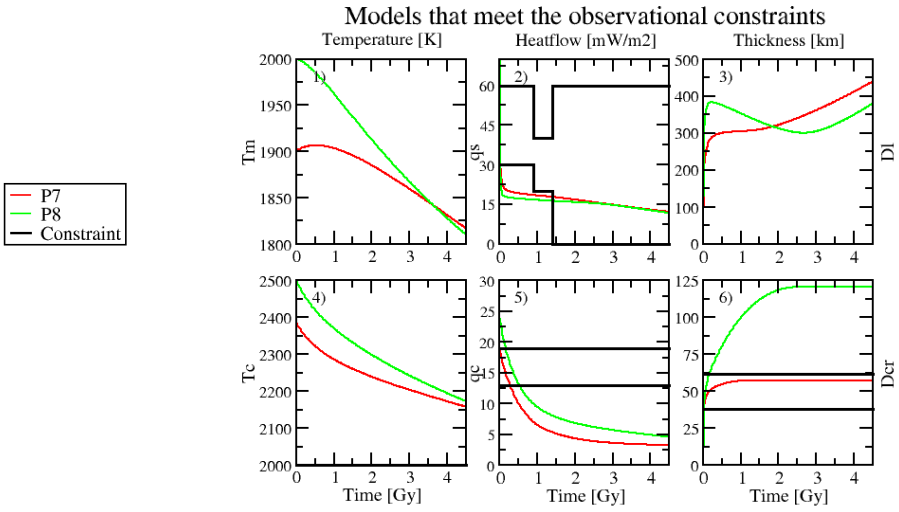

Figure 3.7: Global parameter and heat flow evolution for the two parameterized models P7 and P8 meeting the observational constraints. See Table 3.1 for the model specifications. Thick black lines indicate the observational constraints that will be discussed further in Section 4.1: in plot (2) and (6) the lines represent a minimum and maximum, in (5) two differently derived lower boundaries. See Figure 3.1(a) for a detailed description of the individual plots; note that in plot (2) the surface heat flow is plotted instead of the mantle heat flow.

It can be argued that the crust production is overestimated by the parameterization, however: The parameterized numerical model assumes *all* melt is transferred to the surface to form crust, even if the melt forms at depth. For example, after 500 My, melt forms at a depth of ~330 km and above the CMB for the best fit model (Figure 3.8). It is not likely for the CMB melt to reach the surface, for reasons discussed in Subsection 4.1.2. Breuer and Spohn (2006) do take into account the lesser probability of melt rising to the surface from greater depths by incorporating an extra term depending on the thickness of the lithosphere:

$$\frac{dD_c}{dt} = \frac{D_{pot} - D_c}{D_m} um_a \frac{V_a}{V_m} \left(1 - \frac{D_l}{D_{lcrit}}\right)^n \quad . \tag{3.1}$$

For n = 0, all melt can pass the lithosphere, for n = 1 and n = 3, 50% of the melt reaches the surface for a lithospheric thickness of 300 and 125 km, respectively (Breuer and Spohn, 2006). Including this term in the current parameterization would greatly reduce the crust production in Figure 3.7 (see the evolution of D_l), and, to a lesser extent, the duration of crustal growth. The fact that although molten mantle material is allowed to crystallize and possibly melt again (through the Stefan number), at each integration time step, all melt is included in the crustal growth calculations is also bound to add to the overestimation of the crustal thickness. When corrected for the overestimation of the crust thickness, model P8 would probably fit all the observational constraints well.

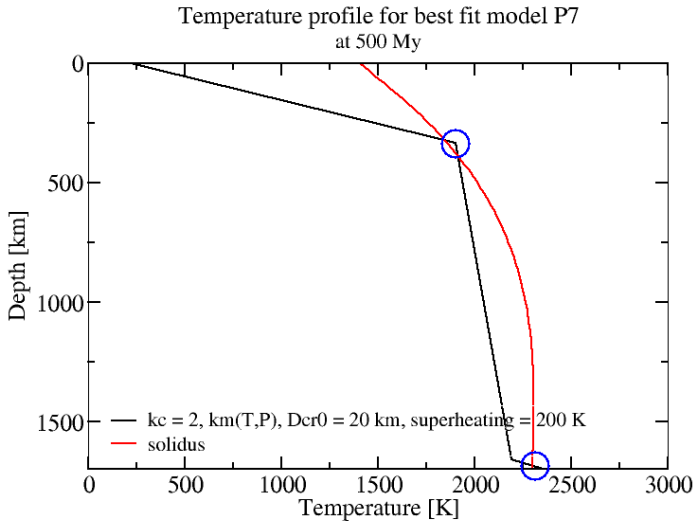

Figure 3.8: Radial temperature profile after 500 My for the best fit model P7. The blue circles indicate the depth ranges where partial melting occurs.

Even with best fit model P7 (and P8), the present-day solidus temperature deficit is still 218 K (165 K), which suggests present-day volcanism is hard to explain. However, parameterized models cannot include lateral variations in temperature, and the obtained temperature profile should be seen as a horizontal average: the geotherm should lie below the solidus for a solid mantle. Locally, temperatures can be raised by, for example, a mantle plume bringing up heat from the core (a plume's excess heat is usually on the order of 100 K (Schumacher and Breuer, 2006)). Also, Schumacher and Breuer (2006) propose that the excess thickness of 20 to 30 km of the Tharsis and Elysium provinces made up of low conductivity crust could result in a local temperature increase of 100-150 K. This in combination with a mantle plume underneath the province could easily produce present-day volumes of melt, especially since Schott et al. (2001) find that variable conductivity can have a focusing effect on mantle plumes. Other studies (de Smet et al., 2000; Drury et al., 2001; Schott et al., 2001) have shown that partial melting rather takes place in the adiabatic upward flow of shallower convection cells than in the warm heads of mantle plumes. With the hot upwellings compensated by cold downwellings (temperatures can vary up to 100-200 K with respect to the horizontal average), melt can be produced even when the horizontally averaged temperature lies below the solidus. The full convection models used in the following sections *can* resolve the mantle's temperature distribution and thus provide insight into the mechanism enabling partial melting. In accordance with best fit model P7, these models will incorporate a primordial crust and in most cases an initial superheating of the core of ~200 K.

3.2 Full convection - Statistical equilibrium models

Unlike parameterized models, full convection modeling *can* resolve the three-dimensional structure of the model domain. This characteristic of full convection models is used here firstly to understand the effect of radioactive element concentration and partitioning between mantle and crust, core superheating, viscosity type and thermal conductivity on the convective planform and melt production of Mars. The parameterized model results have clearly illustrated the importance of these parameters. Also, a comparison of statistical equilibrium (SE) and transient (T) models helps determine whether calculating models to equilibrium gives results representative of the current thermal state of Mars. The final objective is however to find a transient model that is physically plausible and fits all the observational constraints, i.e. that is representative of Mars' entire thermal evolution. Such a model is discussed in Section 4.2.

Table 3.3: Statistical equilibrium models: Model specifications

Model	**C**	$\eta_{\mathbf{m}}$ **[Pas]**	$\eta_{\mathbf{CMB}}(\mathbf{P},\mathbf{T})$ **[Pas]**	$\mathbf{H_{pm}}$ **[Wkg^{-1}]**	**Domain size**	**Figures**
SE1	0.50	9.0066 x 10^{20}	-	4.1 x 10^{-12}	π	3.9(a); 3.10(a); 3.11; 3.12
SE2	0.50	-	9.0066 x 10^{20}	4.1 x 10^{-12}	$1/2\pi$	3.9(b); 3.10(b)
SE3	0.35	5.8278 x 10^{20}	-	4.1 x 10^{-12}	π	-
SE4	0.35	-	5.8278 x 10^{20}	4.1 x 10^{-12}	$1/2\pi$	-
SE5	0.55	11.889 x 10^{20}	-	4.1 x 10^{-12}	π	-
SE6	0.55	-	11.889 x 10^{20}	4.1 x 10^{-12}	$1/2\pi$	-
SE7	0.50	9.0066 x 10^{20}	-	1.5 x 10^{-11}	π	-
SE8	0.50	-	9.0066 x 10^{20}	1.5 x 10^{-11}	$1/2\pi$	-
SE9	0.35	5.8278 x 10^{20}	-	1.5 x 10^{-11}	π	-
SE10	0.35	-	5.8278 x 10^{20}	1.5 x 10^{-11}	$1/2\pi$	-
SE11	0.55	11.889 x 10^{20}	-	1.5 x 10^{-11}	π	-
SE12	0.55	-	11.889 x 10^{20}	1.5 x 10^{-11}	$1/2\pi$	-

The constant mantle viscosity η_{m} and the CMB reference value of the variable viscosity $\eta_{\mathrm{CMB}}(\mathrm{P},\mathrm{T})$ vary simultaneously with the crust fraction of radiogenic heating C, see main text. The CMB lies at a depth of 1698 km, corresponding to ~21.5 GPa. A constant temperature contrast between the surface and the CMB of 1906 K is applied. The constant viscosity models consider a constant surface temperature of 205 K, so $\mathrm{T_{CMB}}$ = 2111 K. For the variable viscosity models, the surface temperature is 220 K, so $\mathrm{T_{CMB}}$ = 2126 K. The heat production density of the primitive mantle, $\mathrm{H_{pm}}$, corresponds to the composition of Wänke and Dreibus (1994) at 0 or 4.5 Gy; models SE7-SE12 are only used to obtain the initial temperature profiles for the transient models.

Calculating models to statistical equilibrium gives an impression of what the thermal state of a planet could be in case the inflow and production of heat are in equilibrium with the outflow of heat. This implies that the thermal state is no longer changing. Kiefer (2003) estimates calculating to statistical equilibrium is allowed for the present-day Mars because previous parameterized studies (Nimmo and Stevenson, 2000 and Weizman et al., 2001, cited in Kiefer, 2003) do not indicate that Mars has a 'thermal memory': the present mantle temperature is insensitive to the precise initial temperature (see also Figure 3.6(a)). Also, Kiefer (2003) argues that because current mantle heat flows are low (as calculated in the studies cited), Mars is close to thermal equilibrium. However, it remains questionable whether such assumptions can be made for an active planet like Mars. Comparing statistical equilibrium results (this section) to the present-day thermal state obtained from transient models (next section) will resolve this question.

Although several statistical equilibrium models have been run to investigate the effect of radioactive element partitioning (models SE1-SE6 of Table 3.3), it is chosen to discuss only the results of two models with an identical crust fraction of 0.50, but different viscosity structures (models SE1 and SE2). For a discussion of the effect of the crust fraction C (defined in Subsection 2.2.1) on the equilibrium models of the current thermal state of Mars, the reader is referred to Kiefer (2003; Li and Kiefer, 2007). Results of models SE1-SE6 are in accordance with the findings of Kiefer (2003).

Model SE1 considers a constant viscosity in the convecting part of the mantle and in the lithosphere, with viscosity in the 212-km thick lithosphere 10^5 times higher than in the mantle. In model SE2, temperature- and pressure-dependent Arrhenius viscosity is implemented (reference value $\eta_{\mathrm{CMB}}(\mathrm{P},\mathrm{T})$ is given in Table 3.3). The same two types of viscosity are used for the transient models. Solid-state creep in mantle minerals is activated by higher temperatures and deactivated by higher pressures (Schubert et al., 2001); the viscosity type of model SE2 is therefore assumed to be most representative of the Martian mantle, especially in the cooling transient models.

A crust fraction of 0.50 is chosen based on findings of Kiefer (2003): models with 43-50% of the Wänke and Dreibus (1994) radioactivity remaining in the mantle satisfy the observed volcanic resurfacing rate on Mars as well as the typical melt fraction of shergottites (meteorites originating from Mars). Kiefer (2003) does not give explicit values of the viscosity model used. Therefore I have derived the value of the constant mantle viscosity (and the reference CMB value for the variable viscosity) from the internal heating Rayleigh number $\mathrm{Ra_H}$ and C, which *are* given by Kiefer (2003), via $\mathrm{Ra_H} = \frac{\rho \mathrm{g} \alpha \mathrm{H_m} \mathrm{d}^5}{\mathrm{k} \kappa \eta_{\mathrm{m}}}$. From the formulation of the internal heating Rayleigh number, it is clear that higher

mantle temperatures originating from higher heating rates reduce the viscosity in the mantle.

3.2.1 Constant viscosity model SE1

The constant viscosity model run reaches statistical equilibrium after about 10 Gy: the average mantle and core heat flux and mantle temperature then no longer vary significantly (only small fluctuations around the equilibrium values). The equilibrium core heat flow is about 34 mWm^{-2} on average, the surface heat flow is 22 mWm^{-2}. A simple calculation can be done to illustrate that the surface heat flow is indeed in equilibrium with the heat flowing into the mantle plus the heat produced through decay.[1]

Equilibrium is maintained for 10 Gy (until end of run). The average temperature of the equilibrated model domain is 1402 K. In this relatively cool mantle, convection patterns show a combination of hot upwelling plumes and thinner cold downflows. Plumes appear to maintain a fixed position on the CMB for several Gy (during equilibrium). Figure 3.9(a) gives the final temperature distribution of the run as this distribution is considered to be the most equilibrated. Note the thick blue outer shell that represents the cold lithosphere.

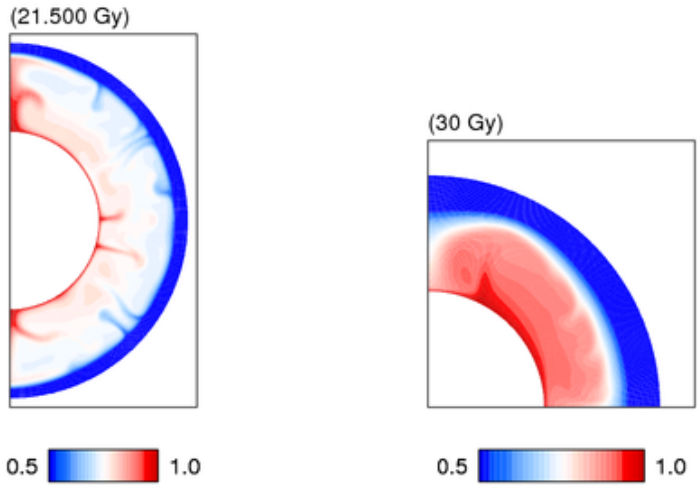

(a) (b)

Figure 3.9: Statistical equilibrium temperature distribution of a) model SE1 of constant viscosity and b) model SE2 of temperature- and pressure-dependent viscosity. Temperatures are non-dimensional, see Subsection 2.2.1 for the applied scaling.

The equilibrated geotherm lies entirely below the polynomial and linear solidus (Figure 3.10(a)). However, because the geotherm represents the horizontally averaged temperature, locally, temperatures *could* exceed the solidus. Indeed, when calculating the instantaneous degree of depletion (Equation 2.14) from the temperature distribution within the model domain, a small degree of depletion (≤ 0.1) is seen in the shallow heads of mantle plumes for a linear solidus and liquidus (compare the temperature distribution (b) and degree of depletion (c) after 10 Gy in Figure 3.11). In case the third order polynomial solidus and liquidus are used, no instantaneous melting is seen.

[1] With a primitive mantle heating rate of 4.1 x 10^{-12} Wkg^{-1}, the total heat production in the statistical equilibrium model domain is (independent of crust fraction C): $H_{pm}\rho_{pm}V_{pm} = 4.1 \text{ x } 10^{-12} \cdot 3400 \cdot \frac{4\pi}{3} \cdot (3396000^3 - 1698000^3) \approx 2.00 \text{ x } 10^{12}$ W . For model SE1, $q_c \cdot A_c = 0.034 \cdot 4\pi \cdot 1698000^2 \approx 1.23 \text{ x } 10^{12}$ W is transferred from the core into the mantle. About $q_m \cdot A_p = 0.022 \cdot 4\pi \cdot 3396000^2 \approx 3.19 \text{ x } 10^{12}$ W is released through the Martian surface. This corresponds well with the combined core heat and radioactive heat production of 1.23 x 10^{12} + 2.00 x 10^{12} = 3.23 x 10^{12} W; it shows that the heat flowing out of the mantle is indeed in equilibrium with the heat flowing into the mantle plus the heat produced through decay. Similar calculations can be done for the pressure- and temperature-dependent viscosity model SE2.

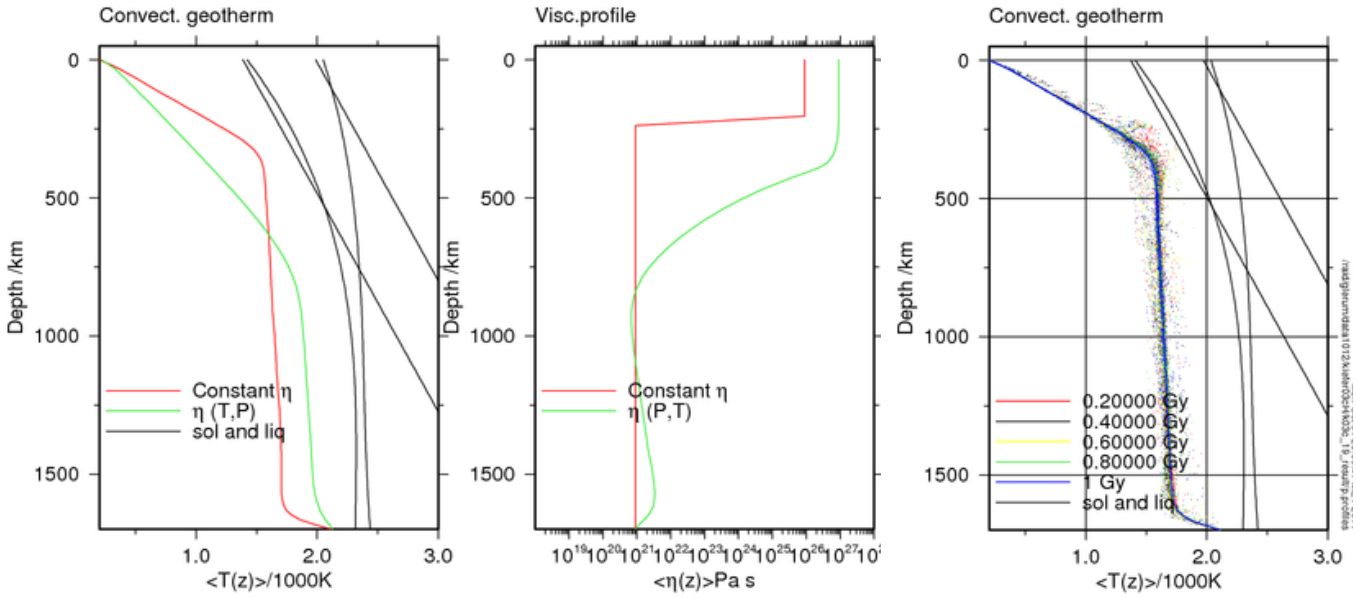

(a) (b)

Figure 3.10: a) Statistical equilibrium geotherms and viscosity profiles for model SE1 of constant and model SE2 of pressure- and temperature-dependent viscosity. b) Statistical equilibrium geotherms for model SE1 continued including passive particle tracers. Both a) and b) include linear and polynomial solidus-liquidus pairs (black curves).

3.2.1.1 Melt productivity

In Figure 3.11(c) the instantaneous degree of depletion is calculated from the temperature field at that specific time, Figure 3.11(b). The calculations do not take into account any previous melting that would inhibit further melting of the same or of a lower degree, thus the degree of instantaneous melt is overestimated. In a further experiment, model SE1 is continued (so equilibrium is already reached) with 2000 passive particle tracers that record the temperature at every integration time step for ~1 Gy. Initially, the tracers are placed in the domain according to a uniform random distribution, with time they are advected by the convective flow. Per tracer, the increase in degree of depletion with time can now be calculated (see Appendix C for a detailed formulation).

The tracers' pressure and temperature distribution (Figure 3.10(b)) illustrates the temperature variations in the mantle with respect to the geotherm: locally, temperatures deviate from the geotherm as much as 300 K. Where tracers barely cross the linear solidus, the polynomial solidus is even higher, explaining why no melt is produced for the polynomial melt relations.

The passive particles tracers show that the increase in the degree of depletion per time bin (a measure of melt production, see Appendix C) decreases over time due to ongoing depletion of the mantle. During the first 56 My at a depth of 300 to 400 km (Figure 3.12(a)) the increase in F is especially large (~0.6). This depth coincides with the mantle plume head seen in the final temperature distribution of model SE1 given in Figure 3.9(a) before continuing the run with passive tracers. At the same depth, three subsequent events of melting can be seen, pointing towards a natural variability in the melt production even though statistical equilibrium has been reached.

The total dimensional melt productivity (in km^3yr^{-1}) with time calculated from the total number of tracers (see Appendix C for details) corresponds well to the increase in degree of depletion binned in time and depth (compare Figures 3.12(a) and 3.12(b)). The time-averaged total melt productivity, more appropriate for equilibrium models, is 0.18 km^3yr^{-1}. This includes the exceptionally high initial peak in productivity that is caused by the rapid evolution

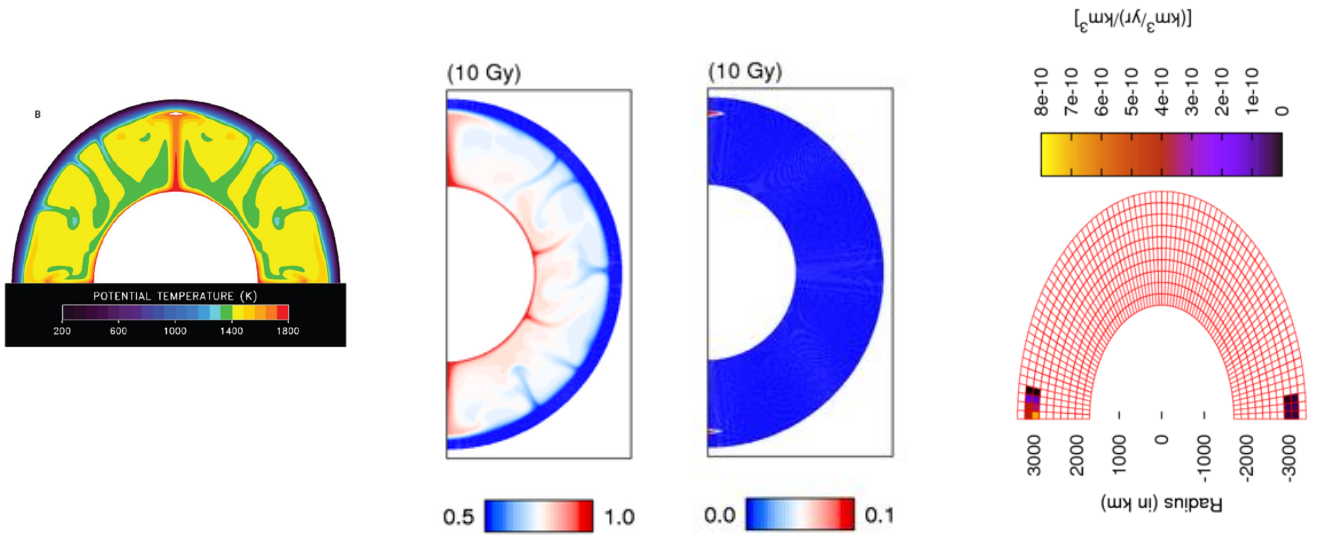

(a) (b) (c) (d)

Figure 3.11: Statistical equilibrium temperature and melt (productivity) distributions for the SE1 model of constant viscosity. a) Temperature distribution at 283 My for a crust fraction of 0.45 from Kiefer (2003, p. 1822, figure 3b). Note that Kiefer gives the potential temperature in the mantle. The actual temperature is obtained by adding the adiabatic contribution of 0.18 Kkm^{-1} (Kiefer, 2003, pp. 1820 and 1826). b) Temperature distribution of model SE1 after 10 Gy. c) Instantaneous degree of depletion of model SE1 after 10 Gy for a linear and parallel solidus and liquidus. d) Distribution of time-averaged melt productivity (for a linear and parallel solidus and liquidus) per unit bin volume for the SE1 model continued including passive particle tracers.

towards an equilibrium in productivity after adding the particle tracers. Without this peak, the time-averaged melt productivity is 0.084 km^3yr^{-1}.

Distributions of the melt productivity per unit bin volume (see Appendix C) at the time of melt productivity peaks show alternating production at the left and the right vertical boundary. When averaging the melt productivity distributions over the entire runtime of 1.13 Gy (Figure 3.11(d)), it is evident that significant amounts of melt are *only* produced in the two plume heads along the vertical boundaries. This average location represents the most likely melt productivity distribution of the present-day Mars. Please note the trade-off between resolution, i.e. bin size, and accuracy, which depends on the number of tracers in a bin.

Comparison of the melt productivity distribution from the particle tracers and an instantaneous melt production distribution at the same time shows that the latter can only be used as an indication of *where* melting is likely to occur (because temperatures are above the solidus), it does not accurately show *when* melt is actually produced at that location. However, because the location indicated by the instantaneous degree of depletion distribution (Figure 3.11(c)) agrees with the average melt productivity locations of the tracers (Figure 3.11(d)), the instantaneous distributions do not render useless.

3.2.1.2 Considerations on the calculation of partial melting

The constant viscosity thermal equilibrium model SE1 is identical in set-up to the larger set of model runs by Kiefer (2003), except for the larger model domain (spherical versus hemispherical) and the uniform viscosity in the lithosphere (instead of an exponential increase towards the surface). The spherical domain allows for more accurate calculations of the melt productivity (distribution).

The results of this and Kiefer's (2003) study in terms of core heat flow, mantle temperatures, convective planform

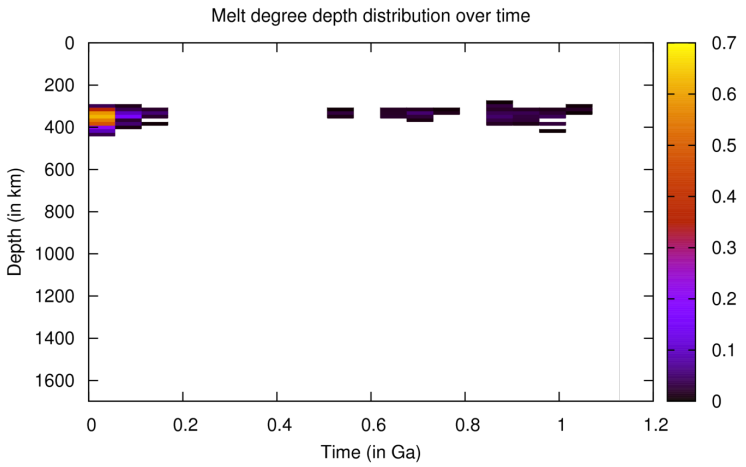

(a)

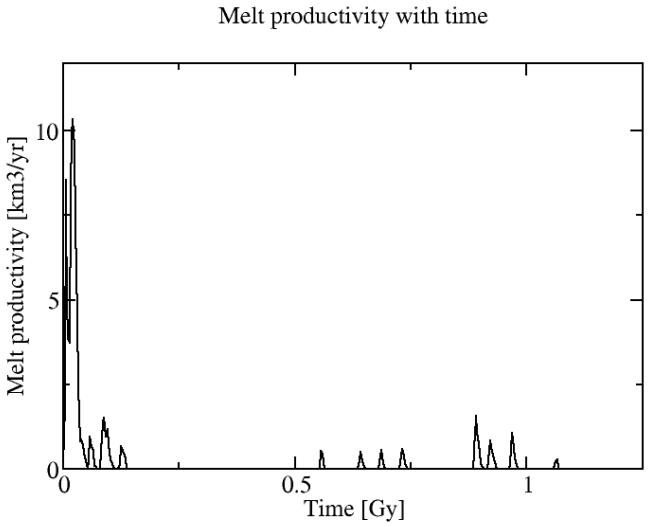

(b)

Figure 3.12: Statistical equilibrium melt productivity (for a linear and parallel solidus and liquidus) for the SE1 model of constant viscosity continued including passive particle tracers. a) Increase in degree of depletion binned in time and depth. b) Total melt productivity with time.

and time variability in melt productivity all agree. For example, Kiefer (2003) finds a core heat flux of 27-33 mWm^{-2} and this thesis one of 31-34 mWm^{-2} (for a subset of Kiefer's models). Also, Kiefer (2003, p. 1822) describes the 'development of a strong upwelling mantle plume' comparable to that of Figure 3.9 (also compare Figures 3.11(a) and 3.11(b)). There *is* a discrepancy in the average melt productivity for a crust fraction of 0.50: that found in this study is roughly two orders of magnitude larger (8.4 x 10^{-2} versus 9.4 x 10^{-4} km^3yr^{-1}). Even though the results of statistical equilibrium model SE1 of this study coincide with the results of the equivalent model of Kiefer (2003), the calculated time-averaged melt productivity during equilibrium differs significantly (8.4 x 10^{-2} versus 9.4 x 10^{-4} km^3yr^{-1}). In part, this difference derives from the different size of the model domains. Here, melt productivity calculations are based on the whole of Mars; because Figure 3.11(d) shows that melting in the lower hemisphere is not as productive as in the upper hemisphere, bluntly halving the obtained time-averaged melt productivity is probably not correct. Thus, the melt productivity of the upper hemisphere is $>$ 4.2 x 10^{-2} km^3yr^{-1}. The remaining difference prompts a review of the method of melt productivity calculation.

In this study, to contribute to melt production, material does not only need to be above the solidus, but the super-solidus temperature $\frac{T(z)-T_{sol}(z)}{T_{liq}(z)-T_{sol}(z)}$ must be higher than during the previous event of melting as well. This incorporates the effect of the melting temperature increasing when material is depleted. The models do however not take into account that depletion increases the buoyancy of the material, possibly preventing the material from sinking into the mantle and being brought up and melting again. Thence, the melt productivity is overestimated. However, if buoyancy of the molten material would be included, the shallow depleted layer would act as an insulating layer keeping the underlying mantle warm and thus enhancing melt production. It can thus be assumed that these effects at least partly cancel out.

Direct comparison with the melting calculations of Kiefer (2003) reveals more room for improvement for the method applied in this study. For one, Kiefer only allows melting if the differential melt production rate increases along the streamline, probably to only allow adiabatic decompression melting. Also, Kiefer adapts the super-solidus temperature field by subtracting the latent heat of melting (although it is not included in the energy balance equation). Neither process is included here, resulting in an overestimation of the melt volume. Hence, melt productivity calculations reported in this study should be considered as upper estimates of Martian melting.

Additional differences in the melt productivity may result from the use of passive particle tracers carrying a degree of melting in this study versus the instantaneous approach of Kiefer (2003) and the 600 K versus 200 K temperature difference between the linear and parallel solidus and liquidus, but it is difficult to quantify their separate contributions.

3.2.2 Temperature- and pressure-dependent viscosity model SE2

For an equal radioactivity partitioning and a CMB reference viscosity equal to the constant mantle viscosity of model SE1, temperature- and pressure-dependent viscosity leads to a volume-averaged mantle temperature of 1250 K during equilibrium. Core and mantle heat fluxes are also much lower than in the constant viscosity case: $q_c = 9$ mWm^{-2} and $q_m = 15$ mWm^{-2}.

From Figure 3.10(a) it is evident that a cold, high-viscosity layer forms at the top of the domain. This stagnant lid is 850 km thick, about three times the value implemented in model SE1. Also, a higher-viscosity layer is seen above the CMB, where viscosity increases almost an order of magnitude. As a consequence, the geotherm is much lower in the stagnant lid and much higher (on average 300 K) in the convective mantle than for constant η_m.

Recalling Figures 3.9(a) and 3.9(b), convection patterns also look strikingly different. Whereas the constant viscosity case is characterized by upwelling mantle plumes, the variable viscosity run knows mostly cold downwellings. Thin downflows extend from the cold top layer, which itself downwells at the vertical boundaries of the domain. Where a single thin mantle plume, originating at the CMB, wells up, the cold layer is slightly thinner.

Horizontally averaged temperatures are well below either solidus (Figure 3.10(a)), so, not surprisingly, no instantaneous degree of depletion is seen after equilibrium is reached. Passive particle tracers would not give different results: model SE2 does not experience melting.

3.3 Full convection - Transient models

Table 3.4: Transient models: Model specifications

Model	**C**	**D_{cr} [km]**	**Viscosity [10^{20} Pas]**	**H_{pm0} [Wkg^{-1}]**	**ΔT_{cm0} [K]**	**T_{c0} [K]**	**k [$Wkg^{-1}K^{-1}$]**	**P.t.?**	**Domain size**	**Figures**
T1										3.13(a); 3.14(a)
T1-1	0.35	50	$\eta_m = 5.8$	1.5 x 10^{-11}	100(215)	2989	k_c=k_m=4	no	π	-
T1-2	0.50	50	$\eta_m = 9.0$	1.5 x 10^{-11}	100(200)	2635	k_c=k_m=4	no	π	-
T1-3	0.50	50	$\eta_m = 9.0$	1.5 x 10^{-11}	0(97)	2531	k_c=k_m=4	no	π	-
T2										3.13(b); 3.14(b); 3.16; 3.17
T2-1	0.35	50	$\eta_{CMB} = 5.8$	1.5 x 10^{-11}	100(192)	2384	k_c=k_m=4	pas	$1/2\pi$	-
T2-2	0.50	50	$\eta_{CMB} = 9.0$	1.5 x 10^{-11}	100(191)	2375	k_c=k_m=4	pas	$1/2\pi$	-
T2-3	0.50	50	$\eta_{CMB} = 9.0$	1.5 x 10^{-11}	0(87)	2271	k_c=k_m=4	pas	$1/2\pi$	-
T3										3.21; 3.20
T3-1	0.35	70	$\eta_{utbl} = 0.28$	4.6 x 10^{-12}	100(193)	2478	k_c=k_m=4	no	$1/2\pi$	-
T3-2	0.35	70	$\eta_{utbl} = 0.28$	4.6 x 10^{-12}	100(193)	2478	k_c=2,k_m=4	no	$1/2\pi$	-
T3-3	0.35	70	$\eta_{utbl} = 0.28$	4.6 x 10^{-12}	100(193)	2478	k_c=2,k_m(T,P)	no	$1/2\pi$	3.19(a)
T3-4	0.35	70	$\eta_{utbl} = 0.28$	4.6 x 10^{-12}	100(193)	2478	k(T,P)	no	$1/2\pi$	3.19(b); 3.21(b); 3.20(b); 3.22(a)
T4	0.35	70	$\eta_{utbl} = 0.28$	4.6 x 10^{-12}	100(193)	2478	k_c=2,k_m(T,P)	act+pas	$1/2\pi$	3.21(b); 3.20(b); 3.22(b); 3.22(c); 3.24

C is the crust fraction of radiogenic heating (see Subsection 2.2.1) and D_{cr} the implemented constant thickness of the crust. The constant mantle viscosity η_m varies simultaneously with the crust fraction, and so does the pressure- and temperature-dependent viscosity CMB reference value $\eta_{CMB}(P,T)$. $\eta_{utbl}(P,T)$ is the reference value of the variable viscosity at the bottom of the upper thermal boundary layer in correspondence to the parameterized models of Section 3.1. It is calculated with Equation 2.9 for T_m = 1900 K. The initial heat production density H_{pm0} corresponds to the composition of Wänke and Dreibus (1994), or Schumacher and Breuer (2006) derived from Treiman (1986), see Table 3.2. ΔT_{cm0} is the initial superheating of the core with respect to the mantle and T_{c0} is the resulting initial uniform temperature of the core. The bracketed value for ΔT_{cm0} derives from the additional superheating of the core resulting from the representation of the core as an isothermal reservoir (for details on core superheating and temperature, see Appendix B). The non-bracketed superheating is used to refer to the models. k is the thermal conductivity. Particle tracers (p.t.) can be passive (pas) and active (act). Compositional buoyancy is implemented through the use of active particle tracers.

The objective of the transient models, which do include time-dependent radioactive decay and a cooling core reservoir, is fourfold. Firstly, the effect of 1) different radioactive element partitionings, 2) core superheatings, 3) viscosity types, 4) thermal conductivities in the crust and mantle and 5) different internal heating densities is investigated. See Table 3.4 for the specific parameter values. Of this parameter study, models T1-2 and T2-2 are equivalent to statistical equilibrium models SE1 and SE2, respectively (except for the internal heating and initial temperature profile), as to test the validity of using thermal equilibrium runs to investigate the present-day state of Mars. Model T3 in turn corresponds to the parameterized models P1 and P2 combined, allowing for a comparison of the parameterized and full convection thermal evolutions. Fourthly, based on the above, I work towards a comprehensive model of the evolution of the thermal state of Mars in Chapter 4.

3.3.1 Radioactive element partitioning between mantle and crust

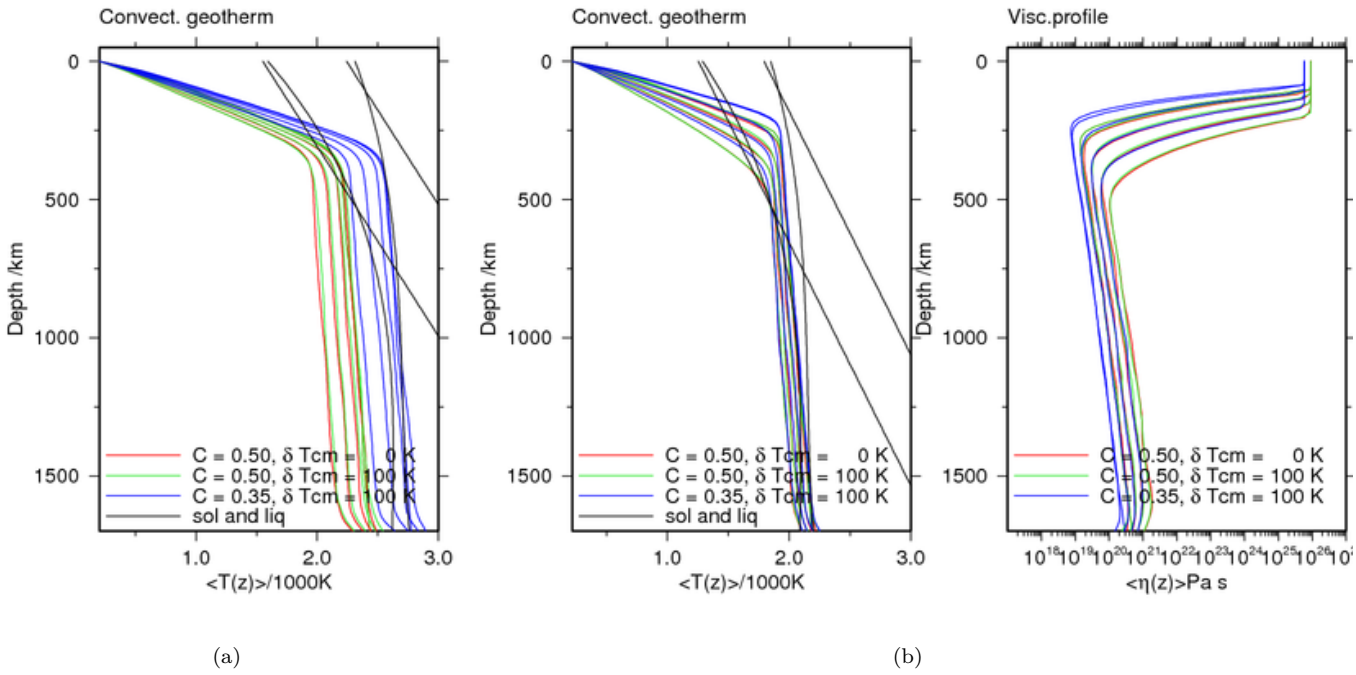

(a) (b)

Figure 3.13: a) Transient geotherm evolution for model T1 of constant viscosity. b) Transient geotherm and viscosity profile evolution for model T2 of temperature- and pressure-dependent viscosity. Geotherms and viscosity profiles are shown at model times 0, 1.125, 2.25, 3.375 and 4.5 Gy.

Internal temperatures of the equilibrium models are higher for models with a lower crust fraction of heat production. For the transient models starting from a geotherm calculated from a statistical equilibrium run with the same crust fraction, a low crust fraction therefore implies a warmer initial temperature profile. Model T2-1 with a low crust fraction of 0.35 starts off and ends with a higher geotherm than model T2-2 with C = 0.50 (compare the blue and green line in Figure 3.13(b)). The amount of cooling in both models is thus similar. Differences in the geotherm are most profound in the upper 400 km of the domain. Despite significant cooling, both the T2-1 and the T2-2 geotherm still exceed the solidus at a depth of about 500 km after 4.5 Gy.

The pressure- and temperature-dependent viscosity follows the geotherm; hence viscosity is slightly higher for C = 0.50, and a thicker lid forms (Figure 3.13(b)).

Figure 3.14(b) shows that the root-mean-square velocity is higher when more radioactive elements remain in the mantle, indicating convection is more vigorous. However, the evolution of the core and mantle temperature is identical

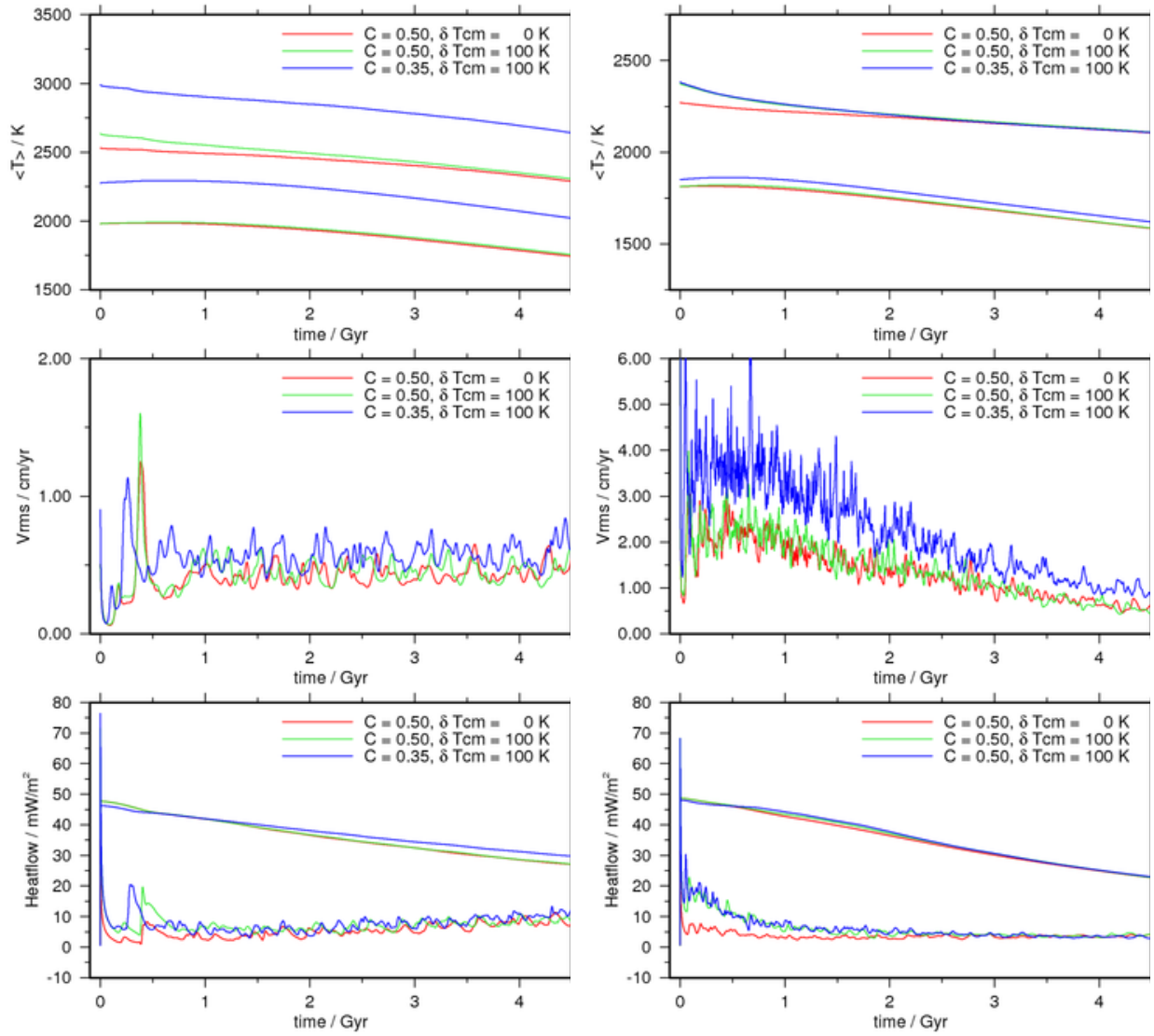

(a) (b)

Figure 3.14: Transient average temperature, velocity and heat flow for a) model T1 of constant viscosity and b) model T2 of temperature- and pressure-dependent viscosity. The upper set of curves in the <T> frame represent the average core temperatures, the lower set the average mantle temperatures. The mantle heat flow is indicated by the upper set of curves in the heat flow frame, the core heat flow by the lower set. Please note the different vertical axes of a) and b).

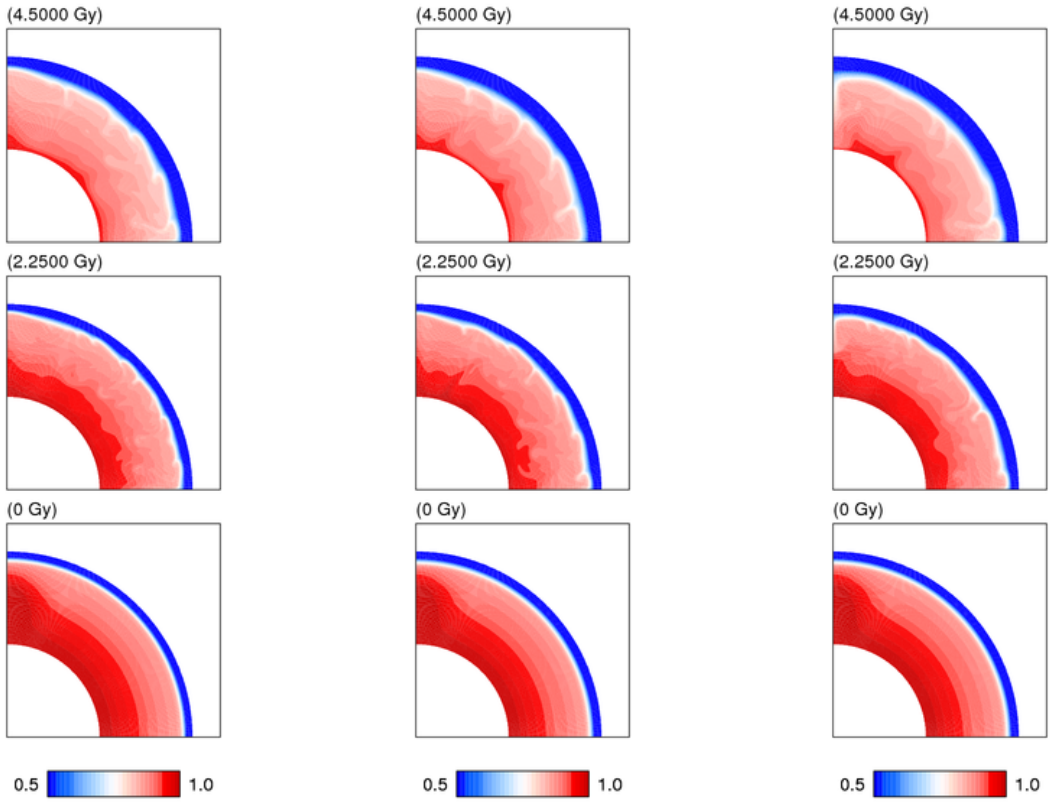

Figure 3.15: Transient temperature distribution for model T2 of pressure- and temperature-dependent viscosity. a) T2-1: C = 0.35, ΔT_{cm0} = 100 K; b) T2-2: C = 0.50, ΔT_{cm0} = 100 K; and c) T2-3: C = 0.50, ΔT_{cm0} = 0 K.

for T2-1 and T2-2, explaining why the core and surface heat flows barely differ.

Differences in convective planform are small as well (Figure 3.15(a) and 3.15(b)). For both crust fractions a gradual cooling of the stably stratified mantle and thickening of the lithosphere is seen. The mantle is devoid of distinct mantle plumes, but shows several thin downflows that reach deeper for model T2-2 (mid-mantle depth).

As the solidus is crossed for both values of the crust fraction, but mantle temperatures differ, different degrees of melting are expected. The passive particle tracer melt productivity calculations do indeed show variation in distribution and magnitude. For example, consider (a) and (b) of Figure 3.16. These represent the melt productivity per unit volume averaged over the first 100 My of thermal evolution. Not only is the maximal productivity 1.6 times higher (1.6 x 10^{-7} versus 1.0 x 10^{-7}) for a crust fraction of 0.35, it is also more widespread. In fact, the total melt productivity with time is much higher and continues longer for more radioactive elements in the mantle, as shown in Figure 3.17. Nevertheless, for both T2-1 and T2-2, melt productivity is concentrated in a layer above the CMB and a shallow layer about 510 km thick during the first 100 My (Figure 3.16). Within the shallow layer, productivity is highest along the left vertical boundary (the symmetry axis) of the model domain. Streamlines are most concentrated along the left boundary as well. With time, the lower boundary of the upper melt zone becomes shallower until melting stops. The

evolution of the total melt productivity also follows a similar pattern: the models are characterized by a very high productivity during the first 100 million years which then decreases rapidly to a productivity on the order of 10^{-2} (see Figure 3.17). Note that apart from this trend the total productivity is highly variable. For T2-2 it takes 2.4 Gy for melt production to end completely, for the warmer model T2-1 melt production ceases after 2.5 Gy.

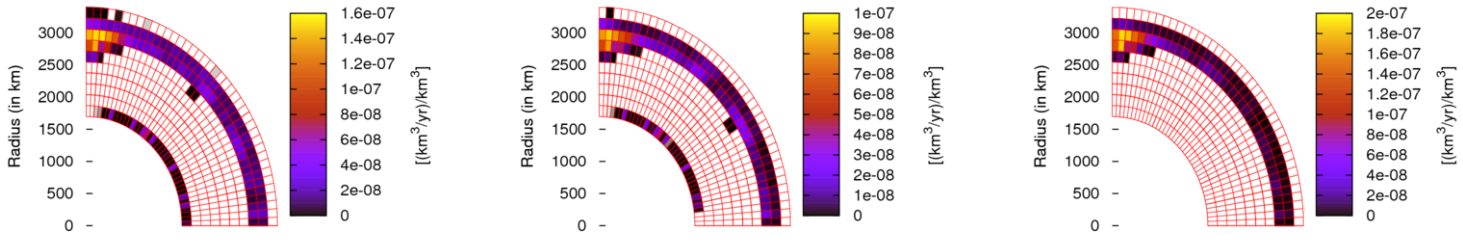

(a) (b) (c)

Figure 3.16: Transient melt productivity distributions averaged over the first 100 My for model T2 of pressure- and temperature-dependent viscosity. Polynomial melting laws are used. a) T2-1: C = 0.35, ΔT_{cm0} = 100 K; b) T2-2: C = 0.50, ΔT_{cm0} = 100 K; and c) T2-3: C = 0.50, ΔT_{cm0} = 0 K. Please note the different colour scales in a), b) and c).

3.3.2 Initial core superheating

Comparison of models T2-2 (ΔT_{cm0} = 100 K) and T2-3 (ΔT_{cm0} = 0 K) demonstrates the effect of initial core superheating (see Appendix B for the definition of ΔT_{cm0} for full convection models). Because of the higher initial temperature of the core for greater ΔT_{cm0}, the initial core heat flux is several tens of mWm^{-2} higher. This way, the core loses more heat and, thus, core temperatures and heat flows of the different models converge within about 2-3 Gy (compare the black and green curves in Figure 3.14(b)). The initial spike in core heat flux is caused by the large temperature difference between the core and mantle at time zero. Thence, it is largest for the highest ΔT_{cm0}.

Volume-average mantle temperatures are hardly affected by the superheating, nor is the surface heat flow (Figure 3.14(b)). Only above the CMB during the first 900 My the geotherms differ (Figure 3.13(b)). Hence, mantle convection patterns do not differ significantly, but a small present-day downflow at the left vertical boundary is seen for the no superheating model that is not found for ΔT_{cm0} = 100 K (Figure 3.15(b) and 3.15(c)).

Interestingly, in comparing figures a), b) and c) of Figure 3.16, it is obvious that superheating of the core enables partial melting above the CMB independent of the crust fraction. Although the maximum melt productivity per unit volume is highest when the core is *not* superheated, the extra layer of melting above the CMB for ΔT_{cm0} = 100 K results in higher and longer lasting total melt productivities (Figure 3.17).

3.3.3 Viscosity type

Comparing corresponding models of constant and temperature- and pressure-dependent viscosity demonstrates the effect of a different viscosity type. Consider, for example, Figure 3.13 for C = 0.50 and ΔT_{cm0} = 100 K, so models T1-2 and T2-2. Already in the initial temperature profile derived from statistical equilibrium runs there is a temperature difference of about 300 K; model T1-2 remains warmer throughout the entire model run. Despite the fact that during the entire Martian history the temperature- and pressure-dependent viscosity in the convective part of the mantle is up to two orders of magnitude lower than the constant viscosity, the development of a thicker stagnant lid prevents efficient global cooling. As a result, the constant viscosity mantle is able to cool much more, but not enough to overcome the initial temperature difference completely within 4.5 Gy.

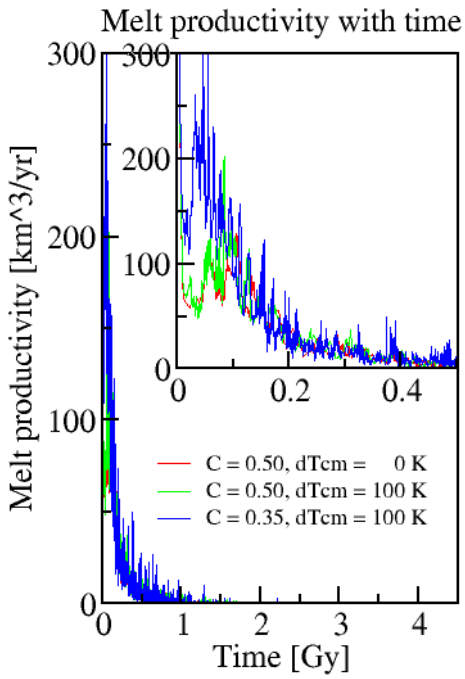

Figure 3.17: Transient total melt productivity with time for model T2 of pressure- and temperature-dependent viscosity. Polynomial melting laws are used. Red: Melt production stops after 2.2 Gy. Green: 2.4 Gy. Blue: 2.5 Gy.

Whereas the variable viscosity run only displays a few thin downflows (Figure 3.15(b)), the constant viscosity mantle is characterized by numerous distinct downflows of cold material sinking deep into the mantle. These downflows could well explain the more efficient cooling, despite the lower mantle velocity of the constant viscosity model (Figure 3.14).

In spite of the fact that the constant viscosity models cool faster, the mantle heat flows do not differ significantly (compare the green curves in the bottom frames of Figure 3.14). It is interesting to note, however, that the core heat flow of model T1-2 experiences a second peak around 400 My and gradually *increases* from about 2 Gy onwards.

The constant viscosity models are very susceptive to the crust fraction and, to a lesser extent, to the initial superheating of the core compared to the variable viscosity models. This is the result of the lack of self-regulation in the constant viscosity models. The temperature-dependence of viscosity ensures that when the mantle is hot, viscosity is low and heat is transported upwards fast. Subsequently, temperature decreases and viscosity increases, shifting towards a viscosity in balance with the internal heating (Schubert et al, 2001). The initial temperature profile then has a smaller effect on the present-day temperature distribution. Because of the sensitivity to crust fraction and superheating, the instantaneous degree of depletion distributions of model T1 show that the extent and degree of the

global layer where melting is possible increase for lower C and higher ΔT_{cm0}.

3.3.4 Applicability of statistical equilibrium models

The applicability of statistical equilibrium runs to the present-day thermal state of Mars is questionable. Most likely calculating models to statistical equilibrium only gives representative results when the mantle is expected to cool and become depleted very slowly (~10 Gy).

Models T1-2 and T2-2 are equivalent to equilibrium models SE1 and SE2 of Section 3.2, respectively. For both viscosity types, the thermal equilibrium and transient numerical models paint a completely different picture in terms of the present-day geotherm and convective planform. Evident from Figure 3.18(a) is the major difference in temperature within the convective mantle for a constant viscosity: transient model T1-2 results in an approximately 500 K higher temperature. Because the temperature difference with the core is much smaller, the core heat flow is as well; the core heat flow of SE1 (34 mWm^{-2}) is so high that it suggests a present-day core dynamo (Nimmo and Stevenson, 2000 and Subsection 4.1.1).Moreover, the equilibrium constant viscosity model (SE1) is characterized by distinct mantle plumes and multiple smaller downflows, while the corresponding transient model (T1-2) knows only downflows. For a variable viscosity, Figure 3.18(b), differences are primarily found in the lithosphere: the stagnant lid is roughly 400 km thinner and much warmer for the time-dependent model (T2-2) (increasing the chance of partial melting). The broad downwelling found during thermal equilibrium (SE2) (Figure 3.9(b)) is not seen in the transient model (Figure 3.15(b)).

The comparison of the statistical equilibrium results with the present-day situation obtained from transient models is clear: the substantially changing thermal state in the transient models does not allow for thermal equilibrium to establish within 4.5 Gy. Although the rate of change in core and mantle heat flow and the exponential heat production density decreases over time, they are not yet constant (for example, consider Figure 3.14). Thus, neither of the statistical equilibrium models SE1 and SE2 represents the present-day thermal state of Mars. It seems necessary,

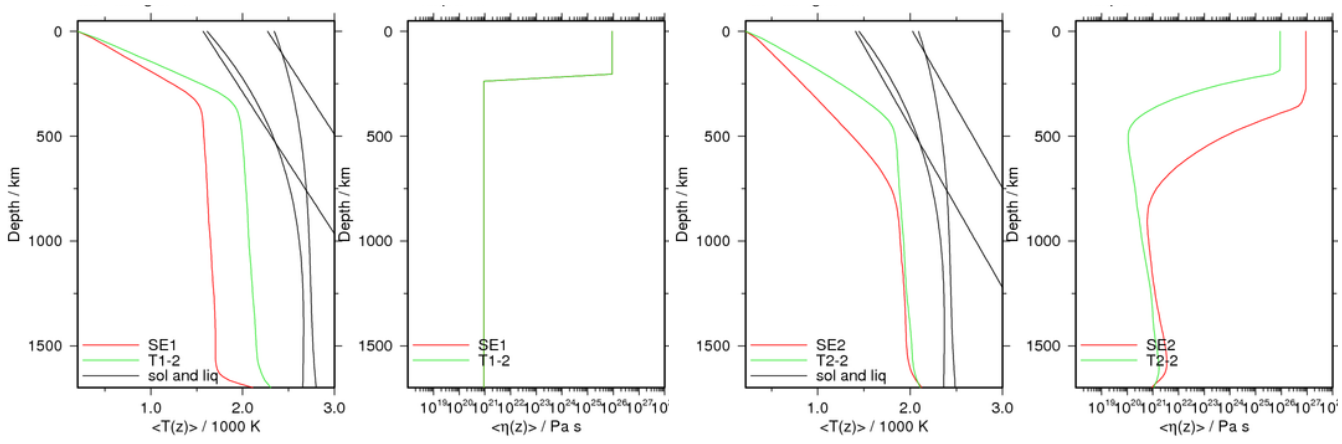

(a) (b)

Figure 3.18: Present-day geotherms and viscosity profiles for corresponding statistical equilibrium and transient models. a) Models SE1 and T1-2 with C = 0.50 and constant viscosity. b) Models SE2 and T2-2 with C = 0.50 and temperature- and pressure-dependent viscosity.

when studying the present-day thermal state of Mars, to consider the entire thermal evolution of Mars instead of approximating the present-day thermal state with statistical equilibrium runs.

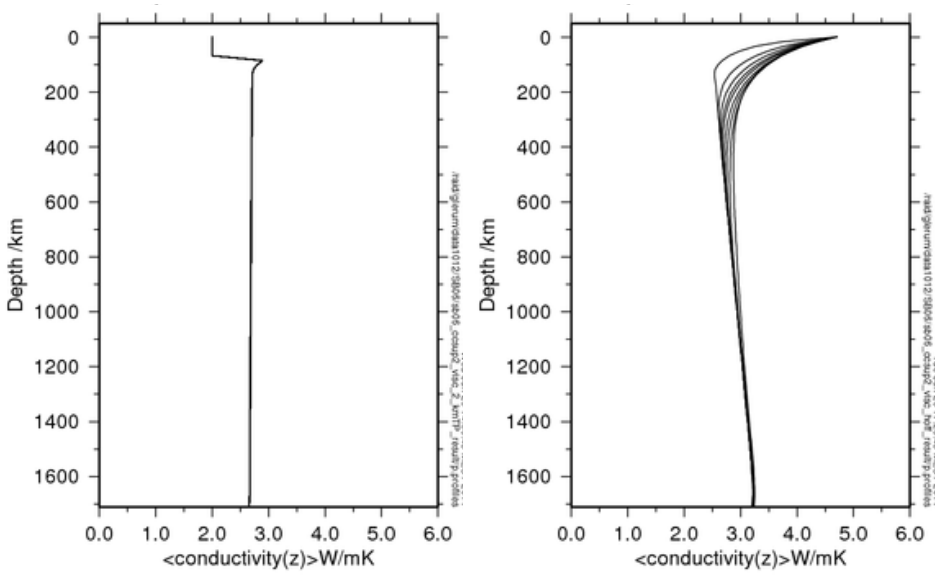

(a) (b)

Figure 3.19: Transient temperature- and pressure-dependent (Hofmeister, 1999) thermal conductivity profiles of a) model T3-3 and b) model T3-4.

3.3.5 Thermal conductivity structure

Four models have been run to assess the effect of the thermal conductivity structure on mantle cooling, convection patterns and melt productivity (equivalent to the parameterized model runs in Figure 3.3, see Table 3.4): Model T3-1 considers a constant, uniform conductivity of 4 $Wm^{-1}K^{-1}$ throughout the model domain. Model T3-2 has a constant conductivity of 2 $Wm^{-1}K^{-1}$ in the crust and of 4 $Wm^{-1}K^{-1}$ in the mantle. T3-3 is characterized by Hofmeister (1999) pressure- and temperature-dependent conductivity throughout the domain. The fourth model, T3-4, has a constant conductivity in the crust of 2 $Wm^{-1}K^{-1}$ and a constant in time, depth-dependent conductivity mantle profile according to the Hofmeister (1999) model at time zero, $k_m(T,P)_{t=0}$. This profile is obtained from the temperature profile calculated at time zero with the parameterization discussed in Section 2.1. Figure 3.19 shows that, compared to the variable conductivity of model T3-3, the assumption of a constant time zero Hofmeister (1999) profile in the mantle underestimates the conductivity.

The initial temperature profile for all four models is taken from the time zero geotherm obtained from the parameterized reference model for a crust of 70 km (the average time-average of the evolutions of the crustal thickness found by Schumacher and Breuer (2006, figure 4b, p. 8) corresponding to C = 0.35[2]). This is in contrast with the starting profile of the other transient models that derives from a statistical equilibrium model, but necessary for an unbiased comparison with parameterized modeling results. When comparing the evolution of the geotherm of T3-1 (Figure 3.20) with the geotherm of an equivalent equilibrium model, it is evident that the parameterized starting profile is quite hot and has a thin lithosphere, but that this difference is overcome within several hundred million years.

Viscosity is temperature- and pressure-dependent and defined by the viscosity at the bottom of the upper thermal boundary layer (Equation 2.9, Section 2.1.2) at time zero. The initial internal heating is lower than in the previous models (see Table 3.4), namely 4.6 x 10^{-12} Wkg^{-1} = 1.6 x 10^{-8} Wm^{-3}, which corresponds to the heating used in the parameterized models.

The conductivity profile has a distinct effect on the temperature in the mantle. Both the temperature profiles

[2] The crustal enrichment factor λ for basaltic melts is 5 (Schumacher and Breuer, 2006), so $Q_c = 5Q_{pm}$. Then, $C = \frac{V_c \cdot Q_c}{V_{pm} \cdot Q_{pm}} = 0.35$.

(Figure 3.20(a)) and the volume-averaged temperature plots (Figure 3.21(a)) are evident of this effect: During 4.5 Gy of thermal evolution, least change from the initial geotherm is seen for model T3-4 with k_c = 2 $Wm^{-1}K^{-1}$, k_m = $k(T,P)_{t=0}$, where especially the lower mantle remains hot (Figure 3.20(a)). For this model the average mantle temperature decreases least as well (from 1898 K to 1633 K). It decreases most for the uniform conductivity of model T3-1 (from 1898 K to 1466 K, Figure 3.21(a)).

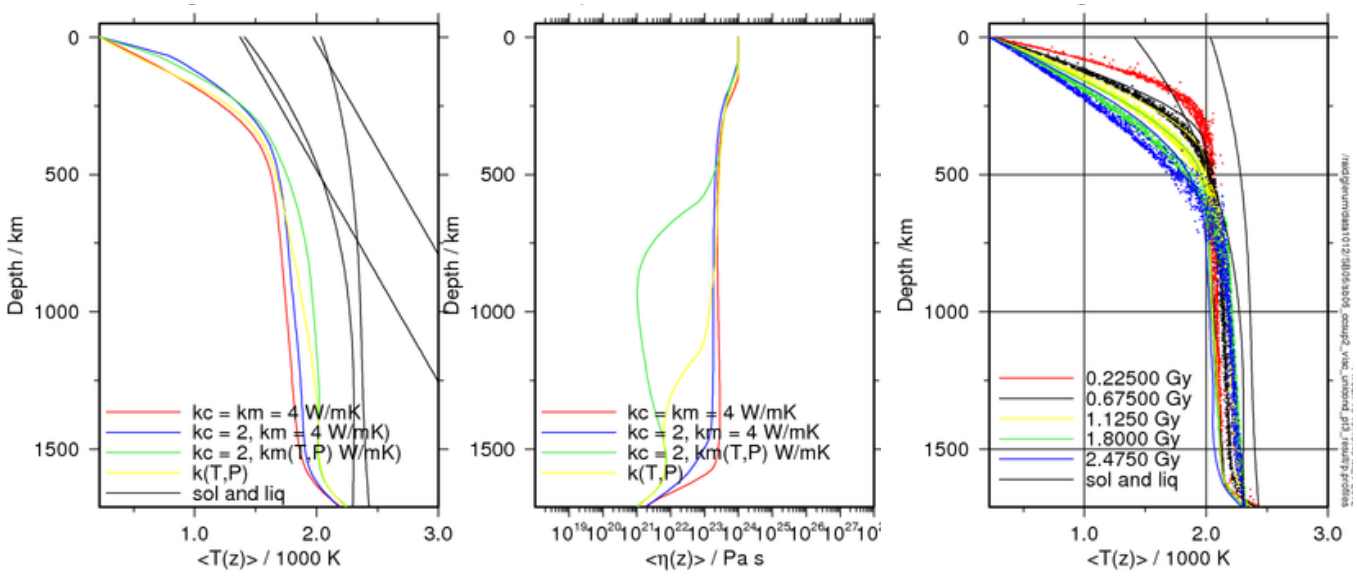

(a) (b)

Figure 3.20: Transient geotherms and viscosity profiles for the contrasting thermal conductivity structures of model T3. a) Present-day geotherms and viscosity profiles for varying conductivity structures without compositional buoyancy. Note the abrupt change in temperature gradient for model T3-2 at the crust-mantle boundary (at a 70-km depth) due to radioactive element partitioning between mantle and crust. b) Passive particle tracer P,T distributions for model T4 with compositional buoyancy and geotherms for the equivalent model T3-4 without compositional buoyancy.

Viscosity is seen to closely follow the mantle temperature profiles (Figure 3.20(a)): The cooler constant conductivity models T3-1 and T3-2 experience a high viscosity ($> 10^{23}$ Pas) up to about 1500 km depth. The warmer k_c = 2 $Wm^{-1}K^{-1}$, $k_m = k(T,P)_{t=0}$ model maintains a low viscosity ($< 10^{22}$ Pas) at depths greater than ~700 km.

The present-day volume-averaged core temperatures are grouped into the lower temperatures of ~2200 K of models T3-1 and T3-2 and the about 50 K higher temperatures of the depth-dependent conductivity models T3-3 and T3-4 (Figure 3.21(a)).

Initially the uniform and Hofmeister (1999) conductivity mantle heat flows in Figure 3.21(a) are almost twice as high as those of the other models. After about 800 My, they converge however. The core heat flows closely resemble each other, but are slightly higher for models T3-1 and T3-2.

Figure 3.22(a) shows the temperature distribution in the model domain for the constant, uniform conductivity of 4 $Wm^{-1}K^{-1}$ (T3-1). Along the vertical boundaries of the model domain, warm material is brought up. Especially along the left vertical boundary (symmetry axis) a persistent mantle plume is seen that is deflected horizontally at the bottom of the lithosphere. This plume is present in all four models. Also characteristic for every model is the development of a large cold downwelling covering most of the domain's surface, with thin downflows extending from it, like in Figure 3.22(a) at 4.5 Gy. Interestingly, the more the thermal conductivity comes to depend on composition, temperature and pressure, the lesser the depth to which the large downwelling extends, probably due to the later start of its formation as a result of the higher temperatures. The high viscosity of the constant conductivity cases inhibits

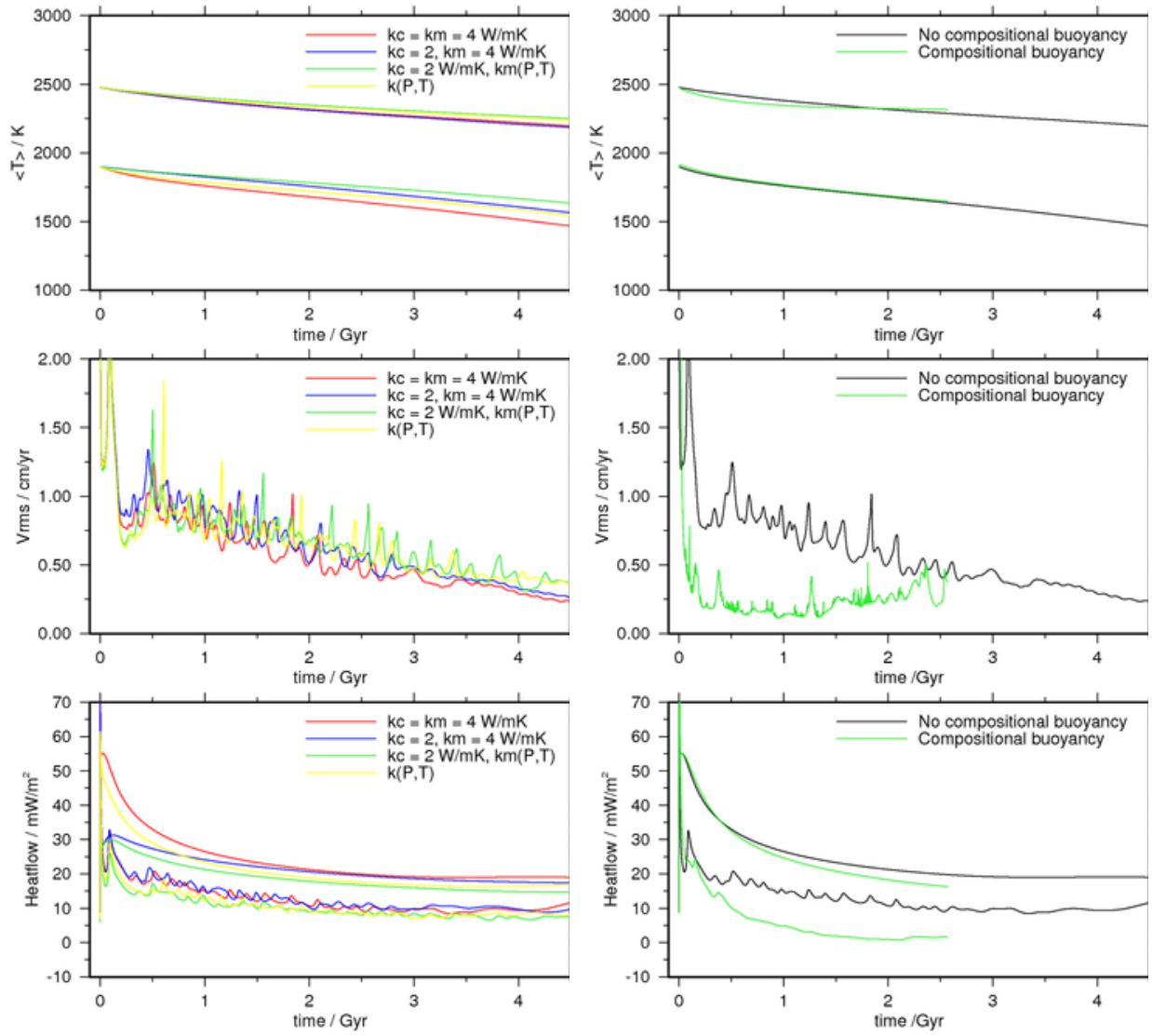

(a) (b)

Figure 3.21: Transient average temperature, velocity and heat flow for contrasting thermal conductivity structures. a) Model T3 without compositional buoyancy. b) Models T3-4 without and T4 with compositional buoyancy.

The extreme variability of the RMS velocity of model T4 in (b) is probably caused by an instability of the model concerning the particle tracer help cells.

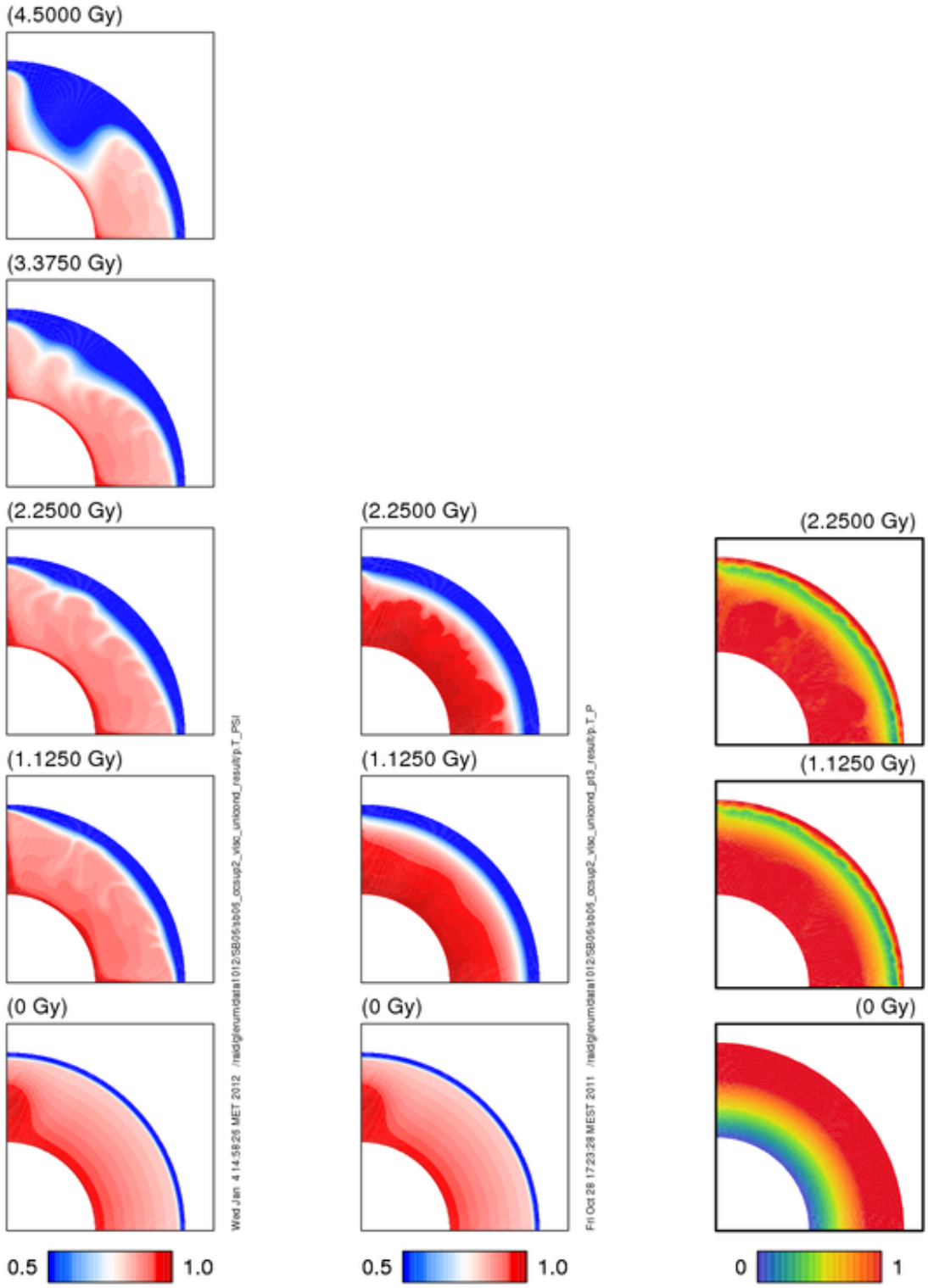

(a) (b) (c)

Figure 3.22: Transient temperature distribution for the uniform thermal conductivity of models a) T3-4 without and b) T4 with compositional buoyancy. c) Composition distribution corresponding to b).

convection within the downwelling, restricting the convective flow.

For all four models, the present-day geotherm lies below the solidus (Figure 3.20(a)). However, early in the thermal history the solidus is exceeded, and a global layer just below the lithosphere is seen where the instantaneous degree of depletion ≤ 0.5. This layer exists longest for the $k_c = 2$ $Wm^{-1}K^{-1}$, $k_m = k(T,P)_{t=0}$ conductivity structure of model T3-4. With the development of the large downwelling, the layer is interrupted, and only along the model's vertical boundaries, where warm material rises up, the possibility of melting persists. As expected, the instantaneous degree of depletion is most profound in the warmer mantles. Hardly any degree of depletion is seen just above the CMB.

3.3.6 Applicability of parameterized convection models

Transient full convection models T3-1 to T3-4 confirm the effect of thermal conductivity structure as shown by the parameterized models in Subsection 3.1.2. The mantle remains warmest for a low crustal conductivity and a Hofmeister mantle conductivity. As a result, partial melting can continue longer and is of a higher degree. Figure 3.23 is a direct comparison of the present-day geotherms of models T3-1 and T3-4 (solid lines) and the equivalent parameterized models with (dash-dotted lines) and without a primordial crust of 40 km (dashed lines). It shows that the parameterization is reliable to a first order; it is however not able to reproduce every detail of the full convection models. Consequently, temperatures in the convecting mantle are up to 200 K higher, while at shallow depths the temperature is too low. Differences in the convective mantle are smaller for the non-uniform conductivity case.

The low temperatures in the top of the model domain could affect the crust production in the parameterized models, as partial melting usually occurs at these depths. However, the overestimation of the crustal growth (Subsection 3.1.5) most likely counterbalances this effect.

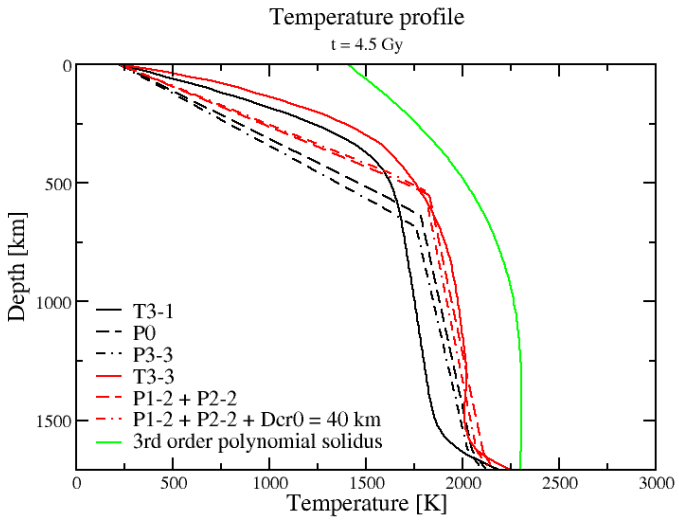

Figure 3.23: Present-day geotherms for equivalent parameterized (P) and transient full convection (T) models and the polynomial solidus.

3.3.7 Compositional buoyancy

The large downwelling mass that develops in the above models (e.g. Figure 3.22(a)) may be related to the absence of compositional buoyancy, which can be an important factor in the longterm planetary evolution (Schott et al., 2001; 2002). The crust is only characterized by a higher heat production density, it does not have a lower density than the mantle, nor are the buoyancy effects of partial melting taken into account. In reality, both the melt and the depleted

layer that form through partial melting have a lower density than the parent material. Ignoring the compositional buoyancy of the depleted top layer and crust probably allows for the sinking of the large cold masses into the mantle (de Smet et al., 2000), cooling the mantle and core at higher rates. As this problem is greatest in the constant, uniform conductivity case (T3-1), a new uniform conductivity run (T4) is started. This time a low, but gradually increasing, density layer is placed just above the CMB at time zero by means of 100,000 active particle tracers. The layer's thickness is chosen such that the layer is 600 km thick at the surface when taking into account geometrical spreading (Schott et al., 2001). Upon the start of the model run, the active tracers are positioned according to a uniformly random distribution and a density perturbation value (between 0 and 3%) is implemented through the tracers. Two thousand passive particle tracers are added as well. So far, this model has ran for 2.56 Gy of model time. The evolution of the distribution of composition within the model domain shows that in less than 225 My the high buoyancy material is transported upwards. From Figure 3.22(c) it is clear that this low density material (blue, green and yellow) then remains at shallow depths organized according to its buoyancy.

The buoyant shallow layer prevents top-down convection, and the temperature distribution (Figure 3.22(b)) shows the development of a thick, cold stagnant lid while the underlying convective mantle heats up. This heating is also illustrated by Figure 3.20(b), the geotherm evolution. Whilst the lithosphere cools and thickens, the convective mantle warms up until after about 1.2 Gy it reaches a steady temperature distribution in equilibrium with the core (the lower thermal boundary layer disappears). The depth at which the solidus is crossed by the geotherm increases until only several individual tracers exceed the solidus (Figure 3.20(b)).

Figure 3.21(b) shows that although the mantle temperature decreases more when no compositional differences are incorporated, the mantle heat flow does not differ between models T3-1 and T4. The core heat flow does: it is above 20 mWm^{-2} during the first 300 My, but becomes practically zero within 1.5 Gy in case a buoyant layer is inserted.

From the passive particle tracer data the evolution of the total melt productivity is calculated for a polynomial solidus and liquidus (Figure 3.24(a), see Appendix C for details): The early melt productivity is very high (up to 4000 km^3yr^{-1}, see inset). However, within 178 My it falls below 1 km^3yr^{-1}, with a minimum of 8 x 10^{-4} km^3yr^{-1}. Around 2.3 Gy, a sudden increase is seen, it is yet unknown whether this increase persists.

During the first 100 My melt productivity is concentrated in a shallow global layer, see Figure 3.24(c). Two centers of activity are seen, one along each vertical boundary. Here, melting reaches much deeper. Moreover, an additional layer of melt productivity is found above the CMB. Also note that the melt productivity per unit bin size is about 4-8 times larger than for models T2-1 to T2-3. However, the extensive distribution of melting diminishes fast. For example, after 1 Gy melt production is only seen above the CMB, and after 2 Gy melting occurs above the CMB and in some isolated regions at mid-mantle depth (see also Figure 3.24(b)). From Figure 3.24(b) it is obvious that the average depth of the upper melt zone increases over time, and melting above the CMB persists. For reasons discussed in Subsection 4.1.2, the melt produced above the CMB is not likely to become crust. When excluding all melt produced at depths greater than 580 km, an upper estimate of crustal productivity is obtained (the red curve in Figure 3.24(a)). The bulk of the crust is produced within the first 700 My, later pulses of crustal growth are seen between 2.32 and 2.56 Gy. These pulses coincide with an increase in the convective vigour, as evident from the increased velocity amplitude at the depth of melting. When distributing the total amount of melt produced at depths smaller than 580 km along the surface of Mars (taking into account geometrical spreading), this would amount to a crust of 292 km thick.

Models T3-4 and T2-1 can help envisage how compositional buoyancy model T4 would react in case the more realistic conductivity structure proposed by Schumacher and Breuer (2006) or a higher initial heat production density (e.g. Wänke and Dreibus, 1994) is incorporated. By switching from uniform conductivity to k_c = 2 $Wm^{-1}K^{-1}$, k_m(T,P), the model without compositional buoyancy increases about 300 K in present-day temperature within the convecting mantle. At t = 2.6 Gy, the runtime of the model with compositional buoyancy, the increase is about 250 K in the upper 750 km. Also, the viscosity is lowered about two orders of magnitude. It can be assumed that incorporating this conductivity structure in the model including compositional buoyancy will have a similar effect: The lower conductivity in the crust and mantle will enhance the insulating effect of the high buoyancy layer. Together with the reduced conductive heat flow in the upper thermal boundary layer this will delay cooling of the mantle due to the lower viscosity. Even though the k_m(T,P) might not act as a way to focus plumes (Schott et al., 2001), it will keep the mantle warm in general (van den Berg et al., 2005). A higher initial heat production density as opposed to

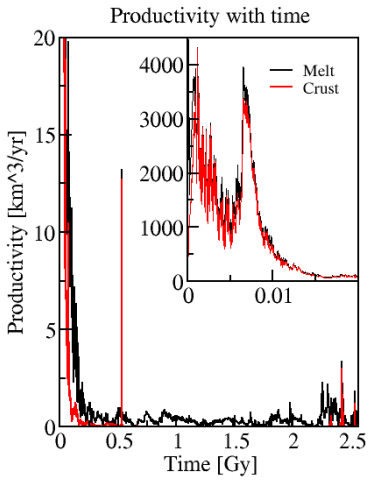

(a)

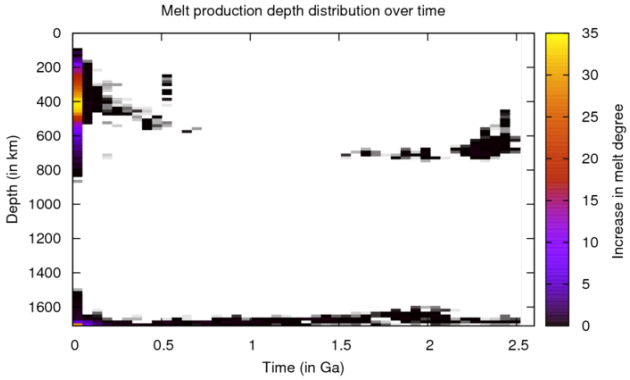

(b)

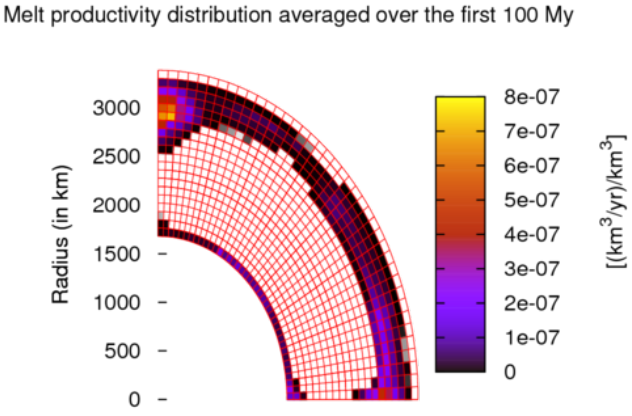

(c)

Figure 3.24: Transient melt productivity for the uniform thermal conductivity of model T4 including compositional buoyancy. a) Total melt and crust productivity with time. After 0.7 Gy, the crust production stops, but it is revived at 2.32-2.33 Gy, 2.41-2.44 Gy and 2.53-2.56 Gy. b) Increase in degree of depletion binned in time and depth. c) Melt productivity per unit bin volume averaged over the first 100 My.

that based on element concentrations from Treiman et al. (1986) leads to more internal heating, leaving the mantle even warmer. In the parameter study it is shown it also slows down thickening of the viscous lithosphere, but here the top ~600 km will less likely take part in convection any way due to the increased compositional buoyancy. As a result of the warmer mantle, equilibrium with the core might be reached sooner however.

3.3.8 Conditions for mantle plume generation

In discussing the results of both statistical equilibrium and transient full convection models, the clear division in models with and without the generation of mantle plumes stands out. Mantle plumes form through instabilities in the lower thermal boundary layer and bring up the heat from the core. The boundary layer is maintained by a temperature contrast between the mantle and the core. This contrast is mostly controlled by the mantle's internal heating and the bottom heating by the core. A large internal heating decreases the temperature difference with the core and, thus, the chance of mantle plumes forming. On the other hand, plumes that do form lose less heat during their ascent through the mantle when that mantle is hot.

To investigate the possible onset criteria for plume generation, Figure 3.25 plots the ratio of the total amount of heat produced through decay in the mantle (the internal heating rate, in Watt) and the total amount of heat coming out of the core (the bottom heating rate, in Watt). For the transient models, this ratio varies with time, the equilibrium model ratios are plotted at 4.5 Gy. See the figure's subscript for the specific models used.

Of Figure 3.25, three models develop mantle plumes, namely models SE1, T3-1 and T3-4. Model T4 shows mantle plumes during the first 450 My. All other model runs are absent of plumes. Clearly, the ratio $\frac{\text{internal heating}}{\text{bottom heating}} = 4$ forms the divide between plume and no plume generation. This divide stands for both transient and equilibrium models. Earlier studies already established a relationship between the percentage of internal heating with respect to the combined bottom and internal heating. For instance, Bercovici et al. (1989c, cited in Schubert et al., 2001) found that more, but substantially weaker plumes form for 80% internal heating than for 50%. In the latter case, plumes can coalesce into fewer, but more vigorous plumes.

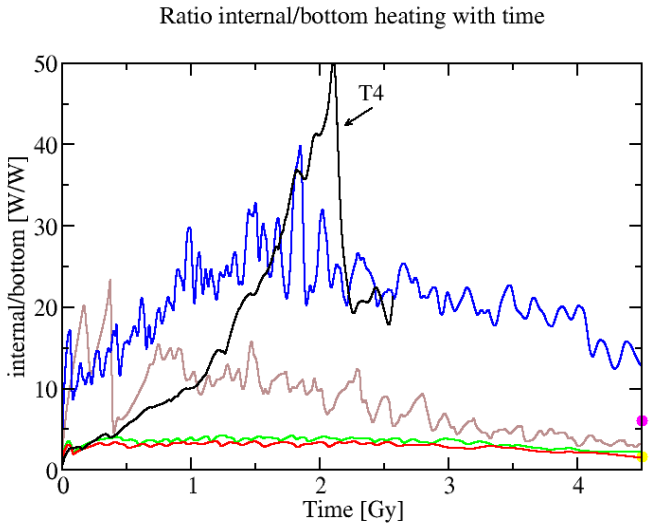

Figure 3.25: Ratio of internal and bottom heating with time for contrasting full convection models. Yellow solid circle: Model SE1. Pink solid circle: Model SE2. Grey: Model T1-2. Blue: Model T2-2. Red: Model T3-1. Green: Model T3-4. Black: Model T4. Models SE1, T3-1 and T3-4 result in mantle plumes throughout their runtime, model T4 only during the first 0.45 Gy.

The internal to bottom heating ratio of model T4 (with compositional buoyancy) is seen to increase up to 2.1

Gy. This increase can be linked to the evolution of the core heat flow in Figure 3.21(b) (green curve), which keeps decreasing at a faster rate than the internal heating. Around 1.1 Gy, core heat flow falls below 4 mWm^{-2}, the lower boundary of the maximum core heat flow that can be sustained by conduction alone, excluding any core dynamo generation (see Subsection 4.1.1). Chapter 4 demonstrates that model T4 also meets a range of other observational constraints, indicating that in this successful model of Martian thermal evolution long-lived mantle plumes originating at the CMB are of no account.

Chapter 4

Discussion of the numerical modeling results

Numerical parameter studies are useful to determine the effect of different model parameters on the planetary evolution. Models prove most helpful however when they can be validated by constraining the model predictions with observational data. Below, the most important observations on Mars are described and converted into applicable model constraints. These constraints are applied to the full convection models with temperature- and pressure-dependent viscosity, resulting in a comprehensive model of Martian thermal evolution.

4.1 From observations to model constraints

4.1.1 Disappearance of the global magnetic field

Observations on the distribution of the remnant magnetization of the Martian crust, the absence or presence of magnetization at old impact basins and the magnetization of an ancient Martian meteorite suggest no geodynamo has been active on Mars for at least the last 4 Gy (Stevenson, 2001; Lillis et al., 2007). However, prior to ~4 Ga a global magnetic field *was* present (Stevenson, 2001).

Dynamo generation requires convective motion in the liquid metal core. Core convection can be caused by thermal buoyancy (through cooling at the CMB) and/or compositional buoyancy (through iron solidification and simultaneous compositional differentiation in the Fe-FeS system, also requiring cooling at the CMB).

Mantle convection cools the mantle, sustaining a temperature deficit with respect to the core, allowing the core to give off heat at the CMB. Subsequently, the colder top material of the core sinks into the core and warmer material rises up. Stevenson (2001) estimates the core must cool about 80 KGy^{-1} for such thermal convection to occur. Using the properties of the core of this study (Table 2.2), this rate equals ~290 GW, which corresponds to about 8 mWm^{-2}.

When the hot core cools below its liquidus, solid material can freeze out. The Martian core is most likely made up of iron with a certain amount of sulphur (Wänke and Dreibus, 1994). The Fe-S system is eutectic, so, depending on whether the amount of sulphur is higher or lower than the eutectic composition, crystallization of iron-rich solids could initiate at the centre of the core or at the CMB (Stewart et al., 2007). In the first case, the lighter sulphur elements would be expelled to the outer core, with the compositional instability of the sulphur enriched liquid at the inner-outer core boundary driving convection (Breuer and Spohn, 2006). The latter case would result in solid particles that, through their higher density, would sink towards the core's centre (Stewart et al., 2007).

Whether the dynamo was sustained by thermal or compositional convection, the absence of a dynamo indicates core convection ceased around 4 Ga and conductive heat transport took over. Nimmo and Stevenson (2000) use Equation 4.1 to estimate the core heat flow that can be sustained by conduction alone; only heat flow in excess of this conductive heat flow contributes to convection.

$$q_{corecond} = \frac{k_{core}\alpha_c g_{CMB} T_{CMBsolidus}}{c_c} \tag{4.1}$$

With k_c = 43-88 $Wm^{-1}K^{-1}$, α_c = 2 x 10^{-5}-3 x 10^{-5} K^{-1} (for solid iron at 25 GPa (Böhler et al., 1990)), g_{CMB} = 3 ± 0.3 ms^{-2} (Longhi et al., 1992), $T_{CMBsolidus}$ = 1800 K (at 25 GPa for a core with 14.5 wt% S (Longhi et al., 1992)) and c_c = 820-860 $Jkg^{-1}K^{-1}$, Nimmo and Stevenson (2000) find that a heat flow of 5-19 mWm^{-2} can be sustained by

core conduction alone. In this thesis, the CMB lies at a pressure of 21.5-22.3 GPa and g_{CMB} = 3.17-3.20 ms^{-2}. The core's specific heat is taken 840 $Jkg^{-1}K^{-1}$. Also, Stewart et al. (2007) experimentally determined the phase changes at 23 GPa for the Fe-S system and obtained a much lower solidus temperature of about 1316 K. Together, these new parameters shift the heat flux boundaries substantially to 4-13 mWm^{-2}. This agrees well with the cooling rate of 80 KGy^{-1} needed for thermal convection (Stevenson, 2001).

The change from convective to conductive core regime could have had several causes. In the simplest case, the hot liquid core cooled fast until the heat flow could be accommodated by conduction alone (see Equation 4.1 and Stevenson, 2001). Another scenario considers the freezing out of an inner core until the outer core becomes too thin for convection to occur or disappears all together (Stevenson, 2001). A change in the convective regime of the mantle provides another mechanism of stopping dynamo generation (Stevenson, 2001). An early period of plate tectonics or smaller scale recycling of hot and weak lithosphere (van Hunen and van den Berg, 2008) would cool the mantle efficiently, as well as the core. The change to stagnant lid convection could reduce heat loss from the core and, with it, core convection. The models in this study do not incorporate such an ad hoc change of convective regime.

Considering the second scenario, formation of such a large inner core could not have taken more than 500 My, because the global magnetic field ceased around 4 Ga. Inner core crystallization starts when temperatures fall below the liquidus. The CMB temperature obtained from the parameterized numerical models can be extrapolated towards the core's centre along the core adiabat (because the core must have convected during the first 500 My) to test whether the liquidus is crossed. From the energy equation an exponential adiabat can be derived:[1]

$$\frac{dT}{dz} = \frac{\alpha_c T g_z}{c_p} \rightarrow T(z) = T_{CMB} \exp\left(\frac{4\pi\alpha_c\rho_c G R_c z}{3c_c} - \frac{4\pi\alpha_c\rho_c G z^2}{6c_c}\right) \tag{4.2}$$

where the gravitational constant G = 6.67428 x 10^{-11} Nm^2kg^{-2} and z the depth from the CMB towards the centre of Mars. α_c, c_c and ρ_c are assumed constant.

The core is made up of a eutectic mixture of liquid iron and sulphur. The exact eutectic composition of the mixture is still debated, for example, Böhler (1996) assumes 20 wt% S, while Fei et al. (1997; 2000) find a composition of 15.4 wt% at the CMB. For both Fe-FeS eutectics, Breuer and Spohn (2006) assessed the liquidus for a core composition of 14 wt% S (Figure 4.1, red curves labelled Böhler 1996 and Fei et al. 1997; 2000, respectively). Stewart et al. (2007) obtained a eutectic composition of 16 wt% at 23 GPa and of 12 wt% at 40 GPa (centre of Mars) through laboratory experiments. Figure 4.1 shows the highest of the core liquidi for sulphur contents of 10.6, 14.2 and 16.2 wt% found in that same study, that for 10.6 wt% S (red dotted curve labelled Stewart et al. 2007).

Besides the liquidi assessed by Breuer and Spohn and the highest liquidus of Stewart et al. (2007), Figure 4.1 shows two adiabatic core areotherms (Equation 4.2). It is evident that for the core temperature to be entirely above the highest liquidus of Breuer and Spohn (2006), the parameterized CMB temperature must be at least 1900 K (green solid curve). When considering the liquidus of Stewart et al. (2007), T_{CMB} must exceed 2000 K (green dashed curve). These temperatures provide the lower boundary for the parameterized CMB temperature to exclude a geodynamo due to chemical convection during the first 500 My.

All in all, the observation of the cessation of the Martian core dynamo ~4 Ga provides three model constraints: Firstly, after 500 My the core heat flow may not exceed 13-19 mWm^{-2}, before ~4 Ga it should. Secondly, during the first 500 My, a CMB temperature below 1900-2000 K indicates core crystallization and thermochemical convection contributing to the generation of the dynamo. Thirdly, if the core temperature remains *above* the liquidus during the first 500 My, the core must cool at a rate of at least 80 KGy^{-1} for thermal convection to occur.

In all full convection models T2-T4, the CMB temperature remains above the 2200 K during the first 500 My (see Figures 3.14(b) and 3.21), suggesting inner core crystallization played no role in the generation of the Martian dynamo. Prior to 4 Ga, only model T2-3 does not exceed the heat flow constraint of 13 mWm^{-2} calculated above. Models T3-1 and T3-2 even remain above 19 mWm^{-2} during this period. T4 is, however, the only model that after about 1 Gy falls below the lower boundary of the core heat flux that can be sustained by conduction alone, completely excluding any convection in the core.

[1] The linear gravity of the homogeneous core $g_z = \frac{M_z G}{(R_c - z)^2} = \frac{4}{3}\pi G(R_p - z)\rho_c$ is inserted in the left equation of (4.2). This differential equation is then solved by separation of variables resulting in the right equation of (4.2). See also Appendix B.

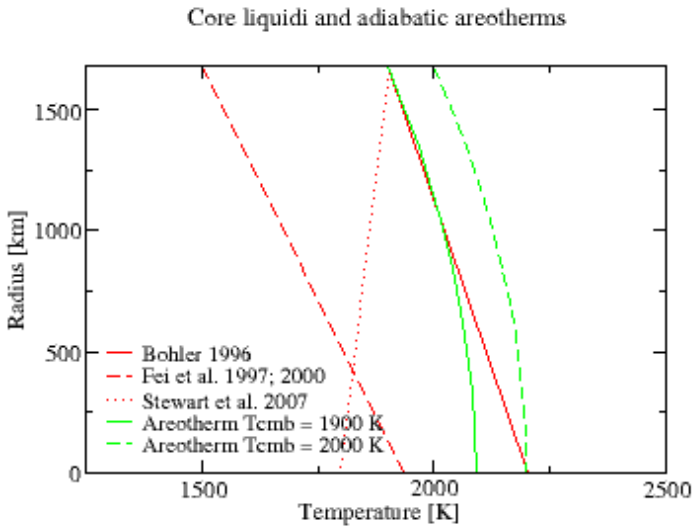

Figure 4.1: Core liquidi based on Fe-FeS eutectics from Böhler (1996) and Fei et al. (1997; 2000) adapted by Breuer and Spohn (2006) and of Stewart et al. (2007) together with two adiabatic areotherms.

4.1.2 Volcanic resurfacing rate and crustal growth

Hartmann and Neukum (2001) find volcanic activity on Mars as recent as 10 Ma. With the help of crater counting techniques they determine the volcanic resurfacing rate throughout the Martian history. The first 500 My, the Early Noachian, the resurfacing rate is relatively low (~3900 km^2My^{-1}), but from the Middle Noachian to the Middle Hesperian, the resurfacing rate peaks ($\leq$ 560,000 km^2My^{-1}). The last 3 billion years, it is more or less constant at 10,000 km^2My^{-1}.

However, the amount of extrusive volcanics does not equal the amount of melting in the mantle and crust. Generally, not all melt reaches the crust because it gets increasingly difficult for melt to migrate through the lithosphere that thickens over time (Schumacher and Breuer, 2006). Also, melt is more compressible than parent rock at pressures above a critical value, decreasing the buoyancy of especially deep magma (Schumacher and Breuer, 2006). Moreover, the majority of melt that reaches the crust remains in the crust as plutonic bodies (intrusive volcanism, e.g. Crisp, 1984). Hence, the melt productivity must be several orders of magnitude higher than the volcanic resurfacing rate.

Kiefer (2003) estimates lava flows are about 3 to 10 m thick on Mars. He also estimates that only 5 to 20% of the melt produced in his models reaches the surface, the rest of the melt becomes intrusive bodies. These assumptions lead to the melt productivities in columns 2 and 3 of Table 4.1. Kiefer (2003) bases the 5 to 20% estimate on the findings of Crisp (1984) who reports intrusive to extrusive volcanics volume ratios of 4:1-16:1 for intraplate volcanism on Earth. In 2006, White et al. state that new investigations show that the ratio is hardly ever higher than 10:1 and there is no correlation with the volcanic setting. Assuming V_i:V_e is 1:1 to 10:1, new magma emplacement and extrusive volcanic rates are obtained, see the fourth and fifth column of Table 4.1.

The rates in column 4 and 5 of Table 4.1 represent a lower estimate of the magma generation within the Martian mantle and crust, because the intrusive and extrusive volcanism as defined by Crisp (1984) and White et al. (2006) only considers magma that rose through the *crust*. Also, crustal underplating and magmatic addition to the lower crust are not included. Nevertheless, most melt is produced between 100 and 800 km depth (see, for example, Figure 3.24(b)), and only part of that melt reaches the crust. Hence, the productivities in Table 4.1 should rather be called 'volcanic productivities' instead of 'melt production rates' as in Kiefer (2003), and melt productivity calculations based on the model results should be corrected for the depth of the melt region. Ohtani et al. (cited in Breuer and Spohn,

Table 4.1: Lower estimate volcanic productivity from volcanic resurfacing rates

Period [Ga]	**Min. C84** [km^3yr^{-1}]	**Max. C84** [km^3yr^{-1}]	**Min. W06** [km^3yr^{-1}]	**Max. W06** [km^3yr^{-1}]
4.5 - 4	5.85 x 10^{-5}	7.80 x 10^{-4}	2.34 x 10^{-5}	4.29 x 10^{-4}
4 - 3	8.40 x 10^{-3}	1.12 x 10^{-1}	3.36 x 10^{-3}	6.16 x 10^{-2}
3 - 0	1.50 x 10^{-4}	2.00 x 10^{-3}	6.00 x 10^{-5}	1.10 x 10^{-3}

Column 2 and 3 have been calculated according to the V_i:V_e ratios of Crisp (1984, C84), column 4 and 5 according to the ratios of White et al. (2006, W06).

2006) find that melt of Mars-analogue composition becomes neutrally buoyant at 7.4 GPa, so at about 580 km depth on Mars. Breuer and Spohn use this depth as critical lithosphere thickness D_{lcrit} (600 km) in the right bracketed term of Equation 3.1 for a parameterization of the percentage of melt to reach the surface. Here, melt that is produced deeper than 580 km is not included in the calculation of the so called volcanic productivity. It is possible for deeper melt to become entrained in an upward convective flow and so to reach the crust passively. Neglecting this possibility is justified in light of the thick (> 400 km) lithospheres that form in the variable viscosity models however.

The northern hemisphere of Mars has been resurfaced during the Hesperian (3.1-3.6 Ga), otherwise, volcanism mostly concentrated in the two volcanic provinces Tharsis and Elysium (Zuber, 2001). Most likely, a primordial crust crystallized from a magma ocean and secondary crust has formed from partial melts. Wieczorek and Zuber (2004) estimate that of the 38 to 62 km of average present-day crust, at least one-third was present as primordial crust. The total volume of volcanics produced according to Table 4.1, when averaged out along the surface of Mars, only adds up to a crust of 25 m for the minimum estimate and of 4.3 km for the maximum estimate. This suggests an even bigger part of the present-day crust is primordial. It is also commonly accepted that the bulk of the Martian crust formed during the Noachian (> 3.6 Ga, Zuber, 2001), possibly followed by extensive Hesperian volcanism and crustal growth (Head et al., 2002, cited in Breuer and Spohn, 2003). This corresponds well with the trend in volcanic productivities seen in Table 4.1. A recent study by Neukum et al. (2010) finds that volcanism continued throughout the lifespan of Mars, but greatly intensified at ~3.8-3.3 Ga, possibly ~2.5-2.2 Ga, 2.0-1.8 Ga, 1.6-1.2 Ga, ~800-300 Ma, ~200 Ma and ~100 Ma.

The crustal thickness as estimated by Wieczorek and Zuber (2004) and the timing of crustal growth act as constraints on the results of the parameterized models (Subsection 3.1.5). Table 4.1 provides a minimum constraint for the volcanic production rates obtained from the full convection models including passive particle tracers. In models T2-1, T2-2 and T2-3, melt production stops within 2.2-2.5 Gy, so these models cannot explain present-day Martian volcanism. The melt productivity of model T4 is well above the volcanic productivity estimates, especially during the first 200 My. Factoring in the improbability of deep melt reaching the surface greatly reduces the melt productivity, but not enough for this volcanic productivity to fall between the observational boundaries (the volcanic productivity would still lead to a crustal thickness of 292 km). This can be expected however, because the rise through the thick lithosphere is troublesome even for melt generated at depths smaller than 580 km. The bulk of the crust is created early in the history of Mars however, and the peaks in volcanic productivity seen in Figure 3.24(a) correspond to the increased intensity of volcanism found by Neukum et al. (2010). However, where Neukum et al. (2010) explain the episodic volcanism through changes in convection from the stagnant lid regime to episodic behaviour, here the vigour of convection is seen to increase locally in the melt zone, indicating increased pressure release melting.

4.1.3 Surface heat flow from volcanic/tectonic structures

Grott et al. (2005) estimate the surface heat flow from topography models at the Martian Coracis Fossae Rift Valley 3.5-3.9 Ga to be 54-66 mWm^{-2} (for a column-averaged thermal conductivity of 2 $Wm^{-1}K^{-1}$). The rift can be seen as representative of magmatically active regions. The heat flow at a 3.7-4.0 Gy old Martian thrust fault, an inactive region, of 24-46 mWm^{-2} is expected to lie closer to the global background heat flow from before 3.5 Ga, because the greater part of the Martian surface can be considered magmatically inactive (Grott et al., 2007). Unfortunately, Grott

et al. (2005; 2007) ignore radioactive heating in the crust, which is why the heat flows must be considered as lower estimates. A similar heat flow of 54-70 mWm^{-2} is found by Schultz and Watters (2001) for the 3.8 Gy old Amenthes Rupes thrust fault (for a thermal conductivity of 3.2 $Wm^{-1}K^{-1}$, so 34-44 mWm^{-2} for 2 $Wm^{-1}K^{-1}$). In conclusion, the surface heat flow is estimated to lie in the range of 24-66 $Wm^{-1}K^{-1}$ or above 3.5-4.0 Ga.

The above surface heat flows are in agreement with the study of McGovern et al. (2004), which incorporates numerous tectonic/volcanic structures with ages spanning the entire lifetime of Mars. The compilation of this data demonstrates how the heat flow is high during the Noachian (> 30-60 mWm^{-2}), then decreases fast to about 20-40 mWm^{-2} during the Hesperian (3.1-3.6 Ga) and becomes highly variable during the Amazonian (0->60 mWm^{-2}).

The surface heat flows can be directly compared to the heat flows outputted by the models: Only for models T3-2 and T3-4 the heat flow during the Noachian is too low. The surface heat flow of all other models falls right within the observational constraints.

4.1.4 Composition of the crust and meteorites

Geochemical data from missions to Mars and the few Martian igneous meteorites found on Earth sample the crust, albeit with a certain bias. They show the composition of the Martian crust is quite uniform: the crust is almost purely basaltic (McSween et al., 2009), except for a few occurrences of siliceous rock (Christensen, 2005, cited in McSween et al., 2009).

McSween et al. (2006) report that the major element concentrations of the Hesperian picritic basalts found in the Gusev Crater suggest the basalts originate from primitive mantle magmas. The younger shergottite meteorites are very similar, indicating a more widespread presence of primitive olivine-rich basalts.

McSween et al. (2009) compiled numerous studies of Martian soils and rocks and meteorites. They conclude that the tholeiitic type of all basalts excludes the need for crustal differentiation or remelting of hydrous, recycled, or alkaline-rich mantle sources, as previously suggested to explain the older rocks determined as calc-alkaline. Thus, there is no need for extensive recycling of crustal material through plate tectonics as seen on Earth. This agrees with the stagnant lid convective regime on which the numerical modeling in this thesis is based. However, a clear compositional difference exists between the 3.7 Gy old Gusev Crater rocks and soils and the younger meteorites, which crystallized only 1.4 Ga, that leads McSween et al. (2009) to believe that the meteorites are not representative of the older crust. Perhaps the differences in composition between old igneous crust and younger igneous meteorites could indicate heterogeneous source regions, for example a change in the depth of the melt region over time.

Noachian (3.6-4.5 Ga) mantle potential temperatures and initial melting depths are derived from the basalts from Gusev Crater and Bounce Rock by Filiberto and Dasgupta (2011). For both locations they find temperatures in the range of 1638-1798 K and melting pressures between 2.7 and 5 GPa (200-400 km); hence, these may represent a Noachian global average.

In short, the basaltic crust of Mars formed from primitive melts (so no remelting or crystal fractionation) that possibly changed in composition over time. Early melting took place at depths of approximately 200-400 km, with mantle potential temperatures of 1638-1798 K, constraining the melt regions found in the numerical models.

Model T3 corresponds well with the depths of partial melting reported by Filiberto and Dasgupta (2011), but melting stops after 2.5 Gy. In model T4, early melting takes place within as well as outside the depth range of 200-400 km, but the melt zone deepens fast. After 750 My, melting only occurs below the critical depth of 580 km. However, 2.5 Ga melting also takes place at shallower depths (Figure 3.24(b)), contributing to renewed crustal growth. It is expected that the average melt zone deepens further, but that additional periods of shallow melting enable crust production up to the present. The increase in depth of the melt regions could result in melts of different compositions (with the deepest melts perhaps being analogue to komatiites on Earth). Melt produced above the CMB will not reach the surface based on a buoyancy contrast, possibly preserving a primitive mantle source that, with increased convective vigour, later becomes entrained in the convective flow and replenishes shallower melt regions.

4.2 Towards a self-consistent model of the evolution of the thermal state of Mars

In Section 3.3, the effect of radioactive element partitioning between mantle and crust, viscosity structure, initial core superheating and thermal conductivity structure on the thermal evolution of a model-Mars has been investigated. Comparison of the results of this investigation with the observational constraints (core heat flow, CMB temperature, volcanic productivity, surface heat flow and the distribution of partial melting) derived in Section 4.1 learns that model T4 incorporating compositional buoyancy meets the requirements; incorporating the more realistic thermal conductivity structure proposed by Schumacher and Breuer (2006) or the higher initial heat production density after Wänke and Dreibus (1994) will ensure longer-lived shallower melting in accordance with the study of Filiberto and Dasgupta (2011).

All in all, a comprehensive model of the thermal history of Mars can now be described. In an initially hot planet, large parts of the mantle are above the solidus, resulting in a voluminous production of melt (and an appreciably less voluminous production of crust). Mantle convection brings up heat from the cooling core and mantle to the lithosphere, where conduction transfers it to the surface. Convective mantle is converted to stagnant lid and, thus, cools, and the less effective conductive lid acts as an insulating blanket on top of the mantle. Subsequently, the underlying mantle warms until within about 1.5 Gy the temperature difference with the core has disappeared (and the lower thermal boundary layer with it). The absence of thermal instabilities at the CMB prevents the formation of mantle plumes, but the mantle is hot altogether, enabling melt production up to at least 2.6 Gy. The distribution of melt productivity changes significantly. Whereas early on melt is produced in a global layer with two centers of higher productivity, within 500 My, the global layer disappears and melting takes place above the CMB and in isolated zones above mid-mantle depth. After the initially high rates of crust production, volcanism now peaks periodically due to the chaotic nature of thermal convection. Within 425 My the core heat flow falls below the maximum heat flow sustainable by conduction alone. With the disappearance of the core-mantle temperature difference, core cooling is further controlled by the slow secular cooling of the mantle. This implies core thermal convection is no longer sustained by heat flow through the CMB. The high temperatures of the core rule out chemical convection through core crystallization as well. Without convection, generation of a global magnetic field becomes impossible.

Chapter 5

Concluding remarks

By constraining an extensive parameter study of the main controls on the thermal state of Mars with observations on the global magnetic field, volcanic resurfacing, crustal growth rates, surface heat flow and the composition of the crust and meteorites, I arrive at a relatively simple, self-consistent model that is physically plausible and explains the thermal state of Mars in view of the observed long-lived volcanism, absence of plate tectonics and the early generation and subsequent cessation of a core magnetic dynamo. This 2D axisymmetric model-Mars labeled T4 in Table 3.4 is characterized by variable Arrhenius type viscosity and includes a buoyant 600 km top layer representing material depleted through partial melting. An initial superheating of ~200 K of the thermally coupled core reservoir is required, but to satisfy melt productivity constraints a relatively low radioactive element concentration in combination with a low partitioning of radiogenic elements into the crust is sufficient. A core dynamo purely driven by thermal convection is active during the first ~400 My, but then disappears due to the equilibration of core and mantle temperatures. The radiogenic internal heating rate of the mantle is significantly higher than the bottom heating from core cooling. This is directly correlated with the absence of long-lived mantle plumes originating from the core-mantle boundary in the model results during most of the model evolution, apart from a relatively brief ~0.5 Gy initial period when the core loses its superheat to the mantle. This finding derived from the self-consistent model contradicts models featuring mantle plumes from the CMB that do not take into account the transient nature of planetary evolution, which is in particular expressed in the time-dependent temperature and heat flux of the core-mantle boundary. An isolating conductive stagnant lid forms that ensures a hot mantle in which episodic partial melting can take place up to the present. Volcanism is episodic and driven by periods of increased convective vigour.

Although this model suggests that the Martian core remains liquid throughout its history, there is no direct evidence that the core is too hot for the crystallization of iron solids. For future research on the thermal state of Mars it would thus be very important to obtain seismic data as this could end the debate on both the phase of the core (solid, partially or completely liquid) and the mean thickness of the crust. Unfortunately, recent plans to set up a seismic network on Mars were hindered by budget cuts and technical difficulties.

In light of this particular research, it is key to study more models including a depleted top layer, as such compositional buoyancy is shown to prevent fast mantle and core cooling and an early stop to magma generation. Models with initial temperature profiles derived from statistical equilibrium models, different radioactive element concentrations and the low crustal, variable mantle thermal conductivity structure would be of interest. It would also be a great step forward to repeat the models that fall within the observational constraints in a three-dimensional spherical geometry, as to properly model the distribution of mantle plumes and melt zones. With the two-dimensional axisymmetric geometry applied here, these are envisaged as ringlike features around the axis of symmetry, while they could well be cylindrical or spherical isolated structures, respectively. Implementing local crustal thickness perturbations (representing volcanic centers) could demonstrate the temperature effect of thickened crust as suggested by Schumacher and Breuer (2006).

Bibliography

[1] M. H. Acuña, J. E. P. Connerney, N. F. Ness, R. P. Lin, D. Mitchell, C. W. Carlson, J. McFadden, K. A. Anderson, H. Rème, C. Mazelle, D. Vignes, P. Wasilewski, and P. Cloutier. Global distribution of crustal magnetization discovered by the Mars Global Surveyor MAG/ER experiment. **Science**, 284(5415):790–793, 1999.

[2] C. B. Agee and D. S. Draper. Experimental constraints on the origin of Martian meteorites and the composition of the Martian mantle. **Earth and Planetary Science Letters**, 224:415–429, 2004.

[3] J. Arkani-Hamed and P. Olson. Giant impacts, core stratification, and failure of the Martian dynamo. **Journal of Geophysical Research**, 115(E07012), 2010.

[4] C. M. Bertka and Y. Fei. Mineralogy of the Martian interior up to core-mantle boundary pressures. **Journal of Geophysical Research**, 102, 1997.

[5] R. Böhler. Fe-FeS eutectic temperatures at 620 kbar. **Physics of the Earth and Planetary Interiors**, 96:181–186, 1996.

[6] R. Böhler, N. Von Bargen, and A. Chopelas. Melting, thermal expansion, and phase transitions of iron at high pressures. **Journal of Geophysical Research**, 95:21,731–21,736, 1990.

[7] L. E. Borg, L. E. Nyquist, L. A. Taylor, H. Wiesmann, and C. Shih. Constraints on Martian differentiation processes from Rb-Sr and Sm-Nd isotopic analyses of the basaltic shergottite QUE 94201. **Geochimica et Cosmochimica Acta**, 61(22):4915–4931, 1997.

[8] D. Breuer, S. Labrosse, and T. Spohn. Thermal evolution and magnetic field generation in terrestrial planets and satellites. **Space Science Reviews**, 152:449–500, 2010.

[9] D. Breuer and T. Spohn. Early plate tectonics versus single-plate tectonics on Mars: Evidence from magnetic field history and crust evolution. **Journal of Geophysical Research**, 108(E7), 2003.

[10] D. Breuer and T. Spohn. Viscosity of the Martian mantle and its initial temperature: Constraints from crust formation history and the evolution of the magnetic field. **Planetary and Space Science**, 54, 2006.

[11] G. Choblet and C. Sotin. 3D thermal convection with variable viscosity: Can transient cooling be described by a quasi-static scaling law? **Physics of the Earth and Planetary Interiors**, 119:321–336, 2000.

[12] Y. A. Crisp. Rates of magma emplacement and volcanic output. **Journal of Volcanology and Geothermal Research**, 20:177–211, 1984.

[13] J. H. de Smet, A. P. van den Berg, and N. J. Vlaar. Early formation and long-term stability of continents resulting from decompression melting in a convecting mantle. **Tectonophysics**, 322:19–33, 2000.

[14] J. de Vries. The origin of lunar basalts. Master's thesis, Utrecht University, 2007.

[15] M. Drury, J. H. de Smet, H. van Roermund, D. A. Carswell, A. P. van den Berg, and N. J. Vlaar. Emplacement of deep mantle peridotites into cratonic lithosphere by convection and diapiric upwelling. **Journal of Petrology**, 42:131–140, 2001.

[16] Y. Fei, J. Li, C. M. Bertka, and C. T. Prewitt. Structure type and bulk modulus of Fe_3S, a new iron-sulfur compound. **American Mineralogist**, 85(11–12):1830–1833, 2000.

[17] Y. Fei, C. T. Prewitt, H. Mao, and C. M. Bertka. Structure and density of FeS at high pressure and high temperature and the internal structure of Mars. **Science**, 268:1892–1894, 1995.

[18] J. Filiberto and R. Dasgupta. Fe^{2+}-Mg partitioning between olivine and basaltic melts: Applications to genesis of olivine-phyric shergottites and conditions of melting in the Martian interior. **Earth and Planetary Science Letters**, 304:527–537, 2011.

[19] H. V. Frey, J. H. Roark, K. M. Shockey, E. L. Frey, and S. E. H. Sakimoto. Ancient lowlands on Mars. **Geophysical Research Letters**, 29:1384, 2002.

[20] O. Grasset and E. M. Parmentier. Thermal convection in a volumetrically heated, infinite Prandtl number fluid with strongly temperature-dependent viscosity: Implications for planetary thermal evolution. **Journal of Geophysical Research**, 103:171–181, 1998.

[21] M. Grott, E. Hauber, S. C. Wemer, P. Kronberg, and G. Neukum. High heat flux on ancient Mars: Evidence from rift flank uplift at Coracis Fossae. **Geophysical Research Letters**, 32, 2005.

[22] M. Grott, E. Hauber, S. C. Wemer, P. Kronberg, and G. Neukum. Mechanical modeling of thrust faults in the Thaumasia region, Mars, and implications for the Noachian heat flux. **Icarus**, 186:517–526, 2007.

[23] C. L. Harper, Jr, L. E. Nyquist, B. Bansal, H. Wiesmann, and C. Y. Shih. Rapid accretion and early differentiation of Mars indicated by 142Nd/144Nd in SNC meteorites. **Science**, 267(5195):213–217, 1995.

[24] W. K. Hartmann and G. Neukum. Cratering chronology and the evolution of Mars. **Space Science Reviews**, 96, 2001.

[25] S. A. Hauck and R. J. Phillips. Thermal and crustal evolution of Mars. **Journal of Geophysical Research**, 107, 2002.

[26] A. M. Hofmeister. Mantle values of thermal conductivity and the geotherm from phonon lifetimes. **Science**, 283:1699–1705, 1999.

[27] A. L. Jaques and D. H. Green. Anhydrous melting of peridotite at 0-15 kb pressure and the genesis of tholeiitic basalts. **Contributions to Mineralogy and Petrology**, 73:287–310, 1980.

[28] S. Karato and P. Wu. Rheology of the upper mantle: A synthesis. **Science**, 260:771–777, 1993.

[29] L. H. Kellogg and S. D. King. The effect of temperature dependent viscosity on the structure of new plumes in the mantle: Results of a finite element model in a spherical axisymmetric shell. **Earth and Planetary Science Letters**, 148:13–26, 1997.

[30] W. S. Kiefer. Melting in the martian mantle: Shergottite formation and implications for present-day mantle convection on Mars. **Meteoritics and Planetary Science**, 39, 2003.

[31] T. Kleine, C. Münker, K. Mezger, and H. Palme. Rapid accretion and early core formation on asteroids and the terrestrial planets from Hf-W chronometry. **Nature**, 418:952–955, 2002.

[32] D. Lee and A. N. Halliday. Core formation on Mars and differentiated asteroids. **Nature**, 388:854–857, 1997.

[33] Q. Li and W. S. Kiefer. Mantle convection and magma production on present-day Mars: Effects of temperature-dependent rheology. **Geophysical Research Letters**, 34, 2007.

[34] R. J. Lillis, H. V. Frey, M. Manga, D. L. Mitchell, R. P. Lin, M. H. Acuña, and S. W. Bougher. An improved crustal magnetic field map of Mars from electron reflectometry: Highland volcano magmatic history and the end of the Martian dynamo. **Icarus**, 194:575–596, 2007.

[35] K. Lodders and B. Fegley, Jr. An oxygen isotope model for the composition of Mars. **Icarus**, 126:373–394, 1997.

[36] J. Longhi, E. Knittle, J. R. Holloway, and H. Wänke. **Mars**, chapter The bulk composition, mineralogy and internal structure of Mars, pages 184–208. University of Arizona Press, 1992.

[37] P.J. McGovern, S.C. Solomon, D. E. Smith, M. T. Zuber, M. Simons, M. A. Wieczorek, R. J. Phillips, G. A. Neumann, O. Aharonson, and J. W. Head. Correction to "Localized gravity/topography admittance and correlation spectra on Mars: Implications for regional and global evolution". **Journal of Geophysical Research**, 109(E07007), 2004.

[38] D. McKenzie. The generation and compaction of partially molten rock. **Petrology**, 25(3):713–765, 1984.

[39] H. Y. McSween et al. Characterization and petrologic interpretation of olivine-rich basalts at Gusev Crater, Mars. **Journal of Geophysical Research**, 111, 2006.

[40] H. Y. McSween, Jr, G. J. Taylor, and Wyatt. M. B. Elemental composition of the Martian crust. **Science**, 324:736–739, 2009.

[41] N. Michel and O. Forni. Mantle convection and phase transitions on Mars. **EPSC Abstracts**, 5, 2010.

[42] D. S. Musselwhite, H. A. Dalton, W. S. Kiefer, and A. H. Treiman. Experimental petrology of the basaltic shergottite Yamato-980458: Implications for the thermal structure of the Martian mantle. **Meteoritics and Planetary Science**, 41(9):1271–1290, 2006.

[43] G. Neukum, A. T. Basilevsky, T. Kneissl, M. G. Chapman, S. van Gasselt, G. Michael, R. Jaumann, H. Hoffmann, and J.K. Lanz. The geologic evolution of Mars: Episodicity of resurfacing events and ages from cratering analysis of image data and correlation with radiometric ages of Martian meteorites. **Earth and Planetary Science Letters**, 294:204–222, 2010.

[44] F. Nimmo and D. J. Stevenson. Influence of early plate tectonics on the thermal evolution and magnetic field of Mars. **Journal of Geophysical Research**, 105, 2000.

[45] M. D. Norman. The composition and thickness of the crust of Mars estimated from rare earth elements and neodymium-isotopic compositions of Martian meteorites. **Meteoritics and Planetary Science**, 34:439–449, 1999.

[46] M. D. Norman. Thickness and composition of the Martian crust revisited: Implications of an ultradepleted mantle with a Nd isotopic composition like that of QUE94201. **Lunar and Planetary Science**, XXXIII, 2002.

[47] C. O'Neill, A. Lenardic, A. M. Jellinek, and W. S. Kiefer. Melt propagation and volcanism in mantle convection simulations, with applications for Martian volcanic and atmospheric evolution. **Journal of Geophysical Research**, 112(E07003), 2007.

[48] C. C. Reese and V. S. Solomatov. Early Martian dynamo generation due to giant impacts. **Icarus**, 207:82–90, 2010.

[49] J. H. Roberts, R. J. Lillis, and M. Manga. Giant impacts on early Mars and the cessation of the Martian dynamo. **Journal of Geophysical Research**, 114(E04009), 2009.

[50] B. Schott, A. P. van den Berg, and D. A. Yuen. Focussed time-dependent Martian volcanism from chemical differentiation coupled with variable thermal conductivity. **Geophysical Research Letters**, 22, 2001.

[51] B. Schott, A. P. van den Berg, and D. A. Yuen. Slow secular cooling and long lived volcanism on Mars, explained. **Lunar and Planetary Science**, XXXIII, 2002.

[52] G. Schubert, D. L. Turcotte, and P. Olson. **Mantle convection in the Earth and planets**. Cambridge U.P., 2001.

[53] R. A. Schultz and T. R. Watters. Forward mechanical modeling of the Amenthes Rupes Thrust Fault on Mars. **Geophysical Research Letters**, 28(24):4659–4662, 2001.

[54] S. Schumacher and D. Breuer. Influence of a variable thermal conductivity on the thermochemical evolution of Mars. **Journal of Geophysical Research**, 111, 2006.

[55] G. Segal and Praagman N. P. **The sepran fem package. Technical report**. Ingenieursburaus Sepra, The Netherlands, 2005. http://ta.twi.tudelft.nl/sepran/sepran.html.

[56] S. C. Solomon, O. Aharonson, J. M. Aurnou, W. B. Banerdt, and M. H. Carr. New perspectives on ancient Mars. **Science**, 307:1214–1220, 2005.

[57] D. J. Stevenson, T. Spohn, and G. Schubert. Magnetism and thermal evolution of the terrestrial planets. **Icarus**, 54:466–489, 1983.

[58] D.J. Stevenson. Mars' core and magnetism. **Nature**, 412:214–219, 2001.

[59] A. J. Stewart, M. W. Schmidt, W. Van Westrenen, and C. Liebske. Mars: A New Core-Crystallization Regime. **Science**, 316, 2007.

[60] E. Takahashi. Speculations on the Archean mantle: Missing link between komatiite and depleted garnet peridotite. **Journal of Geophysical Research**, 95(B10):15941–15954, 1990.

[61] A. H. Treiman, M. J. Drake, M. Janssens, R. Wolf, and M. Ebihara. Core formation in the Earth and Shergottite Parent Body (SPB): Chemical evidence from basalts. **Geochimica et Cosmochimica Acta**, 50:1071–1091, 1986.

[62] D. L. Turcotte and G. Schubert. **Geodynamics**. Cambridge university press, second edition, 2002.

[63] A. P. van den Berg, E. S. G. Rainey, and D. A. Yuen. The combined influences of variable thermal conductivity, temperature- and pressure-dependent viscosity and core-mantle coupling on thermal evolution. **Physics of the Earth and planetary interiors**, 149, 2005.

[64] A. P. van den Berg, P. E. Van Keken, and D. A. Yuen. The effects of a composite non-Newtonian and Newtonian rheology on mantle convection. **Geophysical Journal International**, 115(1):62–78, 1993.

[65] J. van Hunen and A. P. van den Berg. Plate tectonics on the early Earth: Limitations imposed by strength and buoyancy of subducted lithosphere. **Lithos**, 103:217–235, 2008.

[66] N. J. Vlaar, P. E. Van Keken, and A. P. van den Berg. Cooling of the Earth in the Archean: Consequences of pressure-release melting in a hotter mantle. **Earth and Planetary Science Letters**, 121(1–2):1–18, 1994.

[67] H. Wänke and G. Dreibus. Chemical composition and accretion history of terrestrial planets. **Philosophical Transactions of the Royal Society London**, 325(1587):545–557, 1988.

[68] H. Wänke and G. Dreibus. Chemistry and accretion history of Mars. **Philosophical Transactions: Physical Sciences and Engineering**, 1994.

[69] S. Watson and D. McKenzie. Melt generation by plumes: A study of Hawaiian volcanism. **Journal of Petrology**, 32:501–537, 1991.

[70] S. M. White, J. A. Crisp, and F. J. Spera. Long-term volumetric eruption rates and magma budgets. **Geochemistry Geophysics Geosystems**, 7(1), 2006.

[71] M. A. Wieczorek and M. T. Zuber. Thickness of the Martian crust: Improved constraints from geoid-to-topography ratios. **Journal of Geophysical Research**, 109(E01009), 2004.

[72] J. P. Williams and F. Nimmo. Thermal evolution of the Martian core: Implications for an early dynamo. **Geology**, 32(2):97–100, 2004.

[73] C. F. Yoder, A. S. Konopliv, D. N. Yuan, E. M. Standish, and W. M. Folkner. Fluid Core Size of Mars from Detection of the Solar Tide. **Science**, 300, 2003.

[74] M. T. Zuber. The crust and mantle of Mars. **Nature**, 412, July 2001.

Appendix A

Parameterized models: the calculation of partial melting

In the parameterized convection models, quantities m_a, V_a and $\frac{dm_a}{dT_m}$ are calculated per integration time step through a seperate numerical integration over the model domain (see Equation 2.15). The procedure described below applies to both depth ranges (z=0)-($D_l + \delta_u$) and ($D_l + \delta_u$)-($R_c + \delta_l$), with temperatures ranging T_s-T_m and T_m-$\epsilon_m T_m$, respectively (see Figure 2.1). The first depth extent is divided into 501 equidistant nodal points, the second into 1001 points (including the end points).

At each nodal point, the temperature is known due to the assumed constant temperature gradient within each depth range. In a loop over all these points, at each depth the corresponding radius, T_{sol} and T_{liq} are determined. Then, at each point, T(z) is compared to $T_{sol}(z)$. When T(z) is larger than $T_{sol}(z)$, the fraction $\texttt{frac} = \frac{T(z)-T_{sol}(z)}{T_{liq}(z)-T_{sol}(z)}$ (or, degree of depletion F) is calculated and the parameter `volfact` is set to one. In case the temperature at a certain depth is lower than the solidus temperature, both `frac` and `volfact` are assigned the value zero.

The volume integral over the melt region (a spherical shell) is approximated with the summed trapezoidal rule for equidistant nodes over the whole depth range:

$$\int_0^{2\pi}\int_0^{\pi}\int_{r_1}^{r_2} frac(r) r^2 \sin\theta dr d\theta d\psi = 4\pi \int_{r_1}^{r_2} frac(r) r^2 dr = 4\pi\Delta r \left(\frac{frac(r_1) + frac(r_2)}{2} + \sum frac(r_1 + k\Delta r) \right) \tag{A.1}$$

where `frac` can be replaced by `volfact` to compute the volume of the melt region. As `frac` and `volfact` are zero for nodal points outside the melt zone, this corresponds to integrating over just the depth of the melt zone.

The integrated values of both depth ranges are then summed to obtain the total melt volume and the total melt fraction. If the calculated melt volume is equal to or, although unexpected, smaller than zero, the melt concentration is set to zero. In case the volume is larger than zero, the mean melt concentration in the melt region is calculated by $m_a = \frac{\texttt{frac}_{\texttt{total}}}{\texttt{vol}_{\texttt{total}}}$. V_a equals $\texttt{vol}_{\texttt{total}}$.

The above process is executed three times for every time step of the Runge-Kutta integration scheme. Once to calculate the melt concentration for the current value of T_m, once to calculate the concentration for T_m - δT and once for $T_m + \delta$T, all at the same depth. This way, the derivative of m_a to T_m can be computed with a central difference approximation:

$$\frac{dm_a}{dT_m} = \frac{m_a(T_m + \delta T) - m_a(T_m - \delta T)}{2\delta T} \ . \tag{A.2}$$

Appendix B

Full convection models: the isothermal core reservoir

In the transient full convection models, the core is modeled as an isothermal, homogeneous heat reservoir without internal heating. The reservoir cools through an average heat flow q_c through the Core-Mantle Boundary (CMB). The core reservoir temperature T_c thus evolves as follows (van den Berg et al., 2005):

$$\frac{dT_c}{dt} = \frac{-A_c}{\rho_c c_c V_c} q_c(t) \ . \tag{B.1}$$

q_c is computed from the temperature difference between the core and horizontally averaged mantle temperature field according to Fourier's law.

The initial T_c is determined from the initial CMB temperature. Each transient model run starts from a radial temperature profile obtained from an equivalent statistical equilibrium run. The initial amount of superheating of the core is added to the CMB temperature of this profile, giving the CMB temperature of the core. This CMB temperature is extrapolated along the exponential core adiabat derived from the energy equation,

$$\frac{dT}{dz} = \frac{\alpha_c T g_z}{c_p} \rightarrow T(z) = T_{CMB} \exp\left(\frac{4\pi\alpha_c\rho_c G R_c z}{3c_c} - \frac{4\pi\alpha_c\rho_c G z^2}{6c_c}\right) \tag{B.2}$$

where the gravitational constant G = 6.67428 x 10^{-11} Nm^2kg^{-2} and z the depth from the CMB towards the centre of Mars. α_c, c_c and ρ_c are assumed constant. g_z increases linearly towards the centre of the homogeneous core according to $\frac{M_z G}{(R_c - z)^2} = \frac{4}{3}\pi G(R_p - z)\rho_c$.

With the trapezoidal rule for equidistant nodes (see, for example, Equation A.1), the exponential core temperature profile is integrated over the volume of the core. The volume-average is then implemented as the initial temperature of the core reservoir T_c.

In subsequent calculations, T_c, the uniform core temperature, is taken as CMB temperature of the core. This temperature is higher than the CMB temperature obtained through decomposing the volume-averaged core temperature along the exponential adiabat. Numerical integration shows that

$$< T > \ = \frac{1}{V}\int_0^{R_c} 4\pi T(r) r^2 dr \approx 1.04 \ T_{CMB} \ . \tag{B.3}$$

Thus, taking into account geometrical spreading, the volume-averaged temperature is about 4% higher than the CMB temperature for an adiabatic temperature profile. This 4% is included in the bracketed superheating given in the model specifications in Table 3.4.

Appendix C

Full convection models: the calculation of partial melting

Each of the 2000 passive particle tracers is assumed to represent a constant volume of mantle material: $V_{tracer} = \frac{V_{pm}}{nr\,of\,tracers}$. For each tracer m, at each integration time step t, the instantaneous degree of depletion F is calculated from the sampled temperature T and depth z:

$$F^m(t,z) = \frac{T^m(z) - T_{sol}(z)}{T_{liq}(z) - T_{sol}(z)} \ . \tag{C.1}$$

If F = 0, no amount of melt is present, if F = 1, the whole volume represented by the tracer is molten.

Material that is partially molten cannot melt again for the same solidus temperature, hence only when $F^m(t_n)$ is greater than $F^m(t_{n-1})$, melt is produced. Otherwise, $F^m(t_n) = F(t_{n-1})$.

The increase in degree of depletion of the tracers can be displayed binned in time and depth (de Vries, 2007). In this case, the total increase in F during the extent of the time bin of each tracer within the depth range of the bin is summed. For an example, see Figure 3.12(a).

Because each tracer represents a fixed volume of mantle material, melt productivity P per time step can be calculated as well:

$$V^m_{melt\,prod}(t_n) = (F^m(t_n) - F^m(t_{n-1}))V_{tracer} \rightarrow P^m(t_n) = \frac{V^m_{melt\,prod}(t_n)}{t_n - t_{n-1}} \ . \tag{C.2}$$

The melt productivity is displayed in two ways. First, adding the melt productivity of all 2000 tracers at each time step gives the total melt productivity over time (see, for instance, Figure 3.24(a)). Second, the model domain at a certain time step is divided into bins of constant dr and dθ (e.g. Figure 3.24(c), based on the binned degree of depletion displays of de Vries (2007)). The melt productivities of all tracers in a particular bin are summed and then divided by the volume of the bin (which increases with radius), giving the melt productivity per unit bin volume. To ensure the calculations are stable, the calculated melt productivity per unit volume of each bin is time-averaged over 100 My for the transient models and over the entire runtime for the statistical equilibrium models.

The melt productivity incorporates melt produced at all depths. However, for reasons discussed in Subsection 4.1.2, not all melt is expected to reach the surface to form crust. It can be assumed that melt deeper than 580 km will not become part of volcanic in- or extrusions. This melt is excluded from volcanic productivity calculations.